Fundamental Studies on the State of Water with the Generation of Micro and Nano-bubbles

(マイクロ・ナノバブル生成に伴うバブル含有水の状態に関する基礎研究)

Fernanda Yumi Ushikubo

フェルナンダ・ユミ・ウシクボ

Fundamental Studies on the State of Water with the Generation of Micro and Nano-bubbles

(マイクロ・ナノバブル生成に伴うバブル含有水の状態に関する基礎研究)

A dissertation submitted as partial requirement

for the degree of Doctor of Philosophy to

The University of Tokyo

Graduate School of Agriculture and Life Sciences

Department of Biological & Environmental Engineering

by

Fernanda Yumi Ushikubo

フェルナンダ・ユミ・ウシクボ

January 2010

Acknowledgements

I would like to express my appreciation to Professor Seiichi Oshita, for the supervision, fruitful discussions and valuables comments on the research and for his kindness and constant attention.

My gratitude is also addressed to Professor Toyohisa Fujita, Professor Kenji Kurata, Professor Kenji Imou and Professor Yoshio Makino for accepting to compose the examining committee and for their contributive suggestions on the thesis.

I am very grateful to the always pertinent comments of Professor Yoshinori Kawagoe on the research, to his help in different matters in the laboratory.

My sincere thanks to the master students Takuro Furukawa and Ryou Nakagawa and the undergraduate student Masatoshi Enari for the collaboration on the experimental analysis.

It would not be possible to come to Japan without the support of Professor Yasuhisa Seo and Professor Manzo Uchigasaki from Nihon University. I will be always grateful to them.

Special thanks to Mrs. Mihoko Metoki for all her assistance on the bureaucratic procedures and for her immense kindness.

I want to thank Dr. Neelam Ramaiah for her support in the Faculty's affairs and in advising about Japanese daily life.

I appreciate the technical assistance given by Sysmex and by Shimadzu Companies, in the measurements of particle size distribution, and by Microtech Company, in the measurements of zeta potential.

My gratitude for the financial support given by the Food Nanotechnology Project of the Ministry of Agriculture, Forestry and Fisheries of Japan and by Grand-in-Aid for Exploratory Research.

I also thank the Ministry of Education, Science and Culture of Japan for

providing financial assistance to my stay in Japan.

This thesis would not have been completed without the technical support in LaTex given by Roberto Jung Drebes. I also have an immense gratitude for his patience, moral support and companionship during my stay in Japan.

And I am eternally grateful to my parents Emilia and Sergio Ushikubo and my sister Denise for being constantly by my side, though geographically distant.

Finally, I would like to extend my gratitude to everyone who contributed to the completion of my doctoral thesis, by technical advising or personal support.

Fernanda Yumi Ushikubo

January 2010

Table of Contents

List of Figures

List of Tables

Chapter 1

Introduction

1.1 Micro- and nano-bubbles

1.1.1 Definition and Characteristics

As the name suggests, micro-bubbles are bubbles with diameter in the range of micrometers, while nano-bubbles have diameter in the nano-metrical scale. However, there is no consensus about the exact size limit to define micro- and nano-bubbles. According to Tsuge (2007a), the definition of micro-bubble size varies with the application field from the range between 10 and 40 μm, in the study of physiological activity in living organisms, to the range of 500 to 1000 μm, in the application for skin friction reduction in ships.

Serizawa et al. (2003) defined micro-bubbles as bubbles with diameters in the order of less than several tens micrometers. The limit between micro- and macro-bubbles was defined based on the special behavior observed in micro-bubbles regarding physicochemical and fluid dynamic aspects.

Among the physicochemical characteristics of micro- and nano-bubbles (referred to as "MNB" in this study) there is the large specific area and the high pressurization of gas inside the bubble, which confer to these bubbles high gas dissolution capability. Furthermore, micro-bubbles were reported to have an electrically charged surface. It was also observed free-radical generation with the micro-bubble collapse. Regarding the fluid dynamic properties, it was cited the low rising velocity under the liquid phase and the reducing frictional resistance (Tsuge, 2007a). Each characteristic and property is described in details below.

The specific area a_V is calculated by the ratio of the surface area A per volume V. In the case of an spherical bubble with diameter d, the specific area is:

$$a_V = \frac{A}{V} = \frac{\pi\, d^2}{(\pi\, d^3)/6} = \frac{6}{d} \tag{1.1}$$

Thus, the decrease in the bubble diameter result in a larger specific area.

The internal pressure of a bubble can be calculated using the Young-Laplace Equation (Atkins and de Paula, 2006):

$$P_g = P_l + 2\,\frac{\sigma}{r} \tag{1.2}$$

in which P_g and P_l are the gas and the liquid pressure (Pa), respectively; σ is the surface tension (N·m^{-1}) and r is the bubble radius (m).

From the Equation 1.2, it can be observed that the pressure difference between the gas and liquid is inversely proportional to the bubble radius. As an example, a macro-bubble of 1 mm of diameter has a internal pressure of 0.102 MPa and in water, while a 10 μm diameter micro-bubble has 0.130 MPa of internal pressure (using $\sigma = 0.072785$ N·m^{-1}, (Millero, 2001)).

Because of the high gas pressure inside the bubble, the dissolution of gas in the liquid increases, following the Henry's Law (Atkins and de Paula, 2006):

$$c_i = k_H\, P_i \tag{1.3}$$

in which c_i is the molality of the "i" species dissolved in the liquid in the saturation condition (mol·m^{-3}), k_H is the Henry's law constant (mol·m^{-3}·Pa^{-1}) and P_i is the partial pressure of the "i" species in the gas phase (Pa), defined by $P_i = x_i\, P_g$, x_i is the molar fraction of "i".

With the increase in the dissolution of gas into the liquid, the bubble tend to shrink. Therefore, micro-bubbles have a higher shrinking rate than macro-bubbles.

Through the measurement of ζ-potential, the surface of micro-bubbles was found to be negatively charged in a wide range of pH (Takahashi, 2005). In that study, the author stressed the importance of OH^- and H^+ ions in the mechanism of the gas-water interface charge.

Moreover, free-radicals generation was observed with the collapse of micro-bubbles in the absence of dynamic stimulus, without extreme conditions (Takahashi et al., 2007). However, nor-

mally extremely high temperatures induced by adiabatic compression are required for generating free radicals. The shrinking rate of the collapsing bubbles was much slower for micro-bubbles (tens of seconds) than for ultrasound-induced cavitation bubbles (microseconds), indicating a different mechanism for free radicals generation. The generation of radicals during micro-bubbles collapse is thought to be due to the high density of ions during the shrinking of gas, since the ζ-potential increases with shrinking and collapsing processes.

The stagnation of a bubble in water can be estimated through the terminal velocity, given by the Stroke's Law (Clift et al., 2005):

$$V = \frac{1}{18} \frac{(\rho_g - \rho_l)\, g\, d^2}{\mu} \tag{1.4}$$

in which V is the terminal velocity (m·s^{-1}); ρ_g and ρ_l are the densities of the particle and that of the surrounding liquid (kg·m^{-3}), respectively; g is the acceleration of gravity (m·s^{-2}), d is the diameter of the particle (m) and μ is the viscosity of the surrounding liquid (Pa·s).

For example, a nano-bubble of 100 nm diameter has a terminal velocity of 6×10^{-6} mm·s^{-1}, while a 100 μm diameter micro-bubble would rise at 6 mm·s^{-1} and a macro-bubble of 1 mm diameter would go rapidly ascend at approximately 600 mm·s^{-1} (using ρ_g= 1.184 kg·m^{-3} and ρ_l = 997 kg·m^{-3}, corresponding to the air and water densities at 25°C, respectively; g = 9.8 m·s^{-2}; μ = 8.99×10^{-4} Pa·s, corresponding to the water viscosity at 25°C, Lide (2003)).

Finally, the skin friction reduction property of micro-bubbles is thought to be related to the flow laminarization observed with the injection of micro-bubbles in the water flow. By the addition of micro-bubbles, the laminar flow is extended to a higher range of Reynolds number. The reason for this phenomenon is supposed to be the penetration of bubbles into the boundary layer, controlling the turbulent flow by some change in the physical properties of the layer (Serizawa et al., 2003).

1.1.2 Stability

Young-Laplace equation (Equation 1.2) is accepted to describe the internal pressure of macroscopic and microscopic bubbles. The question is if there is a radius limit for the validation of this equation. In nano-scale, for example, a 100 nm radius bubble would present an internal pressure of 1.5 MPa in water (using $\sigma = 0.072785$ N·m^{-1}, (Millero, 2001)), which is too high that they would not probably be stable at atmospheric pressure. Thus, nano-bubbles should have a very short life-

time. In accordance with this hypothesis, Ljunggren and Eriksson (1997) found out that bubbles of 10 and 100 nm radii would have lifetimes of 1 and 100 μs, respectively. The calculations were based on the diffusion of dissolved gas molecules from a spherical gas bubble to determine the shrinkage rate. Young-Laplace Equation (Equation 1.2) and Henry's Law (Equation 1.3) were considered in the calculation.

Furthermore, the validity of Equation 1.2 for nano-bubbles was confirmed through molecular dynamics simulation (Matsumoto and Tanaka, 2008). However, the nano-bubbles can only exist in liquid under highly tensile stress or large negative pressure. That means that nano-bubbles would not be in equilibrium state at atmospheric pressure.

On the other hand, Nagayama et al. (2006) reported that Equation 1.2 is not applicable to nano-bubbles. Using molecular dynamics simulation, the authors concluded that there are too few vapor atoms inside the nano-bubble, which could not promote a high enough pressure to support the force balance with the outer side. In this case, the liquid-vapor interface would play an important role to keep the force balance of a nano-bubble and, therefore, the nano-bubble would be stable at low inner pressure.

According to Hemmingsen (2002), Equation 1.2 may not be applicable to very small bubbles because the surface tension is greatly affected by the interface curvature and the internal gas pressure at that dimension. Tolman (1949) calculated theoretically the surface tension for droplet and concluded that, for small drops, the surface tension should decrease significantly. That is, the surface tension changes with the curvature in the gas-liquid interface. Therefore, the internal pressure of a very small bubble should also have a different magnitude.

Besides the contradictory data show there is no agreement on the nano-bubbles' existence and stability, practical data are still lacking in the literature for the comprehension of these matters. Therefore, the experimental detection of nano-bubbles and an extensive study about their stability are necessary.

1.1.3 Practical Applications

1.1.3.1 General Applications

There are applications of micro- and nano-bubbles in many different fields. Some of them have already practical use, while others are still being investigated as a promising application.

The use of micro-bubbles in separation process by flotation can be applied in wastewater or potable water treatment (Burns et al., 1997; Li and Tsuge, 2006b). The bubbles act removing fine particles from the water by the attachment of particles on the bubble. The smaller the bubble diameter, the more efficient the process, as the collision rate with particles increases (Tsai et al., 2007).

Besides, Gotoh et al. (2006) used micro-bubbles in flotation process to remove oil from polluted soil. Approximately 70 to 80% of oil could be removed because of the excellent physical absorption properties and very low raising velocity of micro-bubbles.

The oil removal from edible algae *nori* using micro-bubbles was reported by Himuro (2007a). The author said that during the shrinking phenomenon, micro-bubbles decreases the hydrogen bonding, which leads to a surface tension decrease in aqueous solution exposed to micro-bubbles. As a result, it was reported an 83% oil reduction in *nori*.

Micro-bubbles were used aiming to enhance the mass transfer of ozone into the water for ozonation process (Li and Tsuge, 2006a). Ozone micro-bubbles can be used for decomposition of organic compounds, being used as oxidant and disinfectant in potable water or for decolorization and odor control in wastewater treatment. Chu et al. (2008) observed higher efficiency of color and chemical oxygen demand (COD) removal using ozone micro-bubble than conventional bubbles in textile wastewater.

Furthermore, the application of micro-bubbles for increasing the dissolved oxygen concentration was performed by Matsuo et al. (2006) with the objective of water purification of a dam lake.

In another application, alcohols, such as ethanol and butanol, can be obtained by anaerobic fermentation of synthesis gas, a mixture of carbon monoxide and hydrogen gases obtained from coal or biomass gasification. However, this gas has low solubility in the fermentation liquid, which makes this technique unfeasible. Bredwell and Worden (1998) obtained mass transfer enhancement of synthesis gas with the use of micro-bubbles produced with surfactants. The authors reported the advantages of this technique: low power consumption, which means low cost technique, and low shear rates in mass transfer comparing to the conventional method, which do not damage the fermentation cells.

The hydrates, which are clathrates formed by gas molecules trapped by water molecules in a hydrogen-bonded network, are normally produced at high pressure and low temperature. With

the objective of generating hydrates at milder conditions, Takahashi et al. (2003) proposed an alternative method to obtain hydrates using micro-bubbles to accelerate the gas dissolution in water. With the addition of 1% of tetra-hydrofuran (THF) as a promoter of hydrate generation in distilled water and the generation of xenon micro-bubbles, the authors could produce hydrates at temperatures lower than 1.6°C.

The use of micro-bubbles to reduce the skin friction in ships was studied by Kodama et al. (2000). Since the depth of ships can reach high values such as 20 m, the pressure on the bottom of the ships may reach up to 0.2 MPa. At this high pressure, the energy required to inject the bubbles is high, which makes it necessary to reduce the volume of the bubbles, making the micro-bubble technology very attractive for this application. By the injection of micro-bubbles into the boundary layer of the wall, it was reported a reduction of 40% of skin friction.

In a different application, Wu et al. (2008) reported the use of nano-bubbles generated by electrochemical treatment as an anti-fouling agent, by preventing the adsorption of proteins by a physical barrier on the surface. Moreover, these bubbles were also effective for cleaning the surface once it was already fouled. The mechanism in this latter case was explained by the detachment of proteins caused by the nano-bubble formation between the protein and the surface. Finally, the protein, adsorbed on the bubble surface, was easily washed away by a low shear water stream.

1.1.3.2 Applications in Living Organisms

Micro- and nano-bubbles have also been applied for the cultivation of shellfishes, yeasts and agricultural products, as described below.

The air micro-bubble supply in the cultivation of oysters (*Heterocapsa circularisquama*) resulted in a better quality product in terms of size and in taste (Onari, 2001). The author cited as effects of micro-bubbles the acceleration of growth by two times compared to the conventional cultivation and the sterilization of the oysters, with total count and *Escherichia coli* count at undetectable level after exposing the oysters in water micro-bubbled for 15 min.

The aerobic cultivation of yeasts (*Rhodoturula mucilaginosa* YR-2) using air micro-bubbles to increase the mass transfer of oxygen to the water was investigated (Ago et al., 2005). As a conclusion, it was found that similar cell mass production is obtained when using micro-bubbles compared to the conventional method, with the advantage of reducing 1/100 to 1/10 of the gas

flow rate. However, irregular surface of yeasts was observed with the cultivation by micro-bubble aeration, while there was no damage for conventional aeration.

Kurata et al. (2007), applying oxygen micro-bubbles in osteoblastic cells culture, reported higher alkaline phosphatase activity, which is related with the higher osteoblastic cell activity. On the other hand, they observed an increase of dead cells and also lower cell viability, comparing to the culture without micro-bubbles. The reasons for this result were probably hyperoxia and cells excessive exposure to fluid shearing force.

In the cultivation of lettuce (*Lactuca sativa*) with hydroponics, Park and Kurata (2009) found a growth enhancement of 2.1 times in wet leaf weight of lettuce subjected to solution containing air micro-bubbles, compared to the lettuce grown in solution with similar dissolved oxygen concentration. The reasons for the growth acceleration were cited as the larger specific surface area of micro-bubbles, which attached to the roots, and the negative charge of micro-bubbles, which might have attracted the nutrients salts. However, the authors stated that these are only possible reasons and further studies are required for the elucidation of the micro-bubbles properties and plant root growth.

In addition, there are indications of acceleration in the cytoplasmic streaming rate of barley coleoptile cells when floated in water after the generation of oxygen micro- and nano-bubbles (Ushikubo et al., 2008).

As described above, although good results were obtained, the mechanism of the acceleration of metabolism is still unclear. One of the reasons for the growth improvement of these living organisms is the better aeration. However, other properties of micro- and nano-bubbles seem to contribute to the physiological activity of the organisms. Besides, as reported in some studies, negative effects of the bubbles were detected. It is important, therefore, to understand which are the properties of micro- and nano-bubbles that can affect the metabolism of the living organisms and to elucidate the mechanism involved.

1.2 Objetives

The general objective of this study was to examine the state of the water with the introduction of micro- and nano-bubbles. This was done by the measurement of dissolved oxygen concentration and pH of water during and after the bubble generation, by the observation of micro-bubbles in microscope to examine their behavior with time.

More specifically, this study aimed to verify the existence of nano-bubbles by the detection of particles at nano-size level using light scattering methods, by the measurement of ζ-potential to verify the presence of electrical charges and by the proton NMR spin-lattice relaxation time, which can indicate changes in molecular interaction with the generation of micro- and nano-bubbles.

1.3 Outline of the Research

This thesis is divided in 6 chapters.

- **Chapter 1**: Introduction

  This chapter presents the state of art of the micro- and nano-bubbles (definition, known characteristics, applications) and the objectives of this study.

- **Chapter 2**: Generation of Micro- and Nano-bubbles

  In this chapter, the method of generation of micro- and nano-bubbles in water is described, as well as the types of water and gases which were used.

- **Chapter 3**: Characteristics of the Water with the Generation of Micro- and Nano-bubbles

  The third chapter includes different measurements: measurements of DO concentration and pH, observation in optical microscope and zeta potential measurements of the water with the generation of micro- and nano-bubbles.

- **Chapter 4**: Particle Size Distribution

  The particle size distribution measured using two different methods, during and after the generation of micro- and nano-bubbles, is described in this chapter. The stability of oxygen and air nano-bubbles along the time is evaluated.

- **Chapter 5**: Proton Nuclear Magnetic Resonance

In this chapter, three different experiments were done in an attempt to find some changes in the proton NMR relaxation times measurements with the introduction of micro- and nano-bubbles in water.

- **Chapter 6**: Conclusion

  The general conclusion of this research and the suggestions for future work are presented.

Chapter 2

Generation of Micro- and Nano-bubbles

2.1 Introduction

The production of MNB without the addition of electrolytes or surfactants is difficult because of the strong surface tension of the water (Takahashi, 2005). Therefore, some methods were developed to generate small bubbles using different principles.

The two general methods to produce colloidal dispersions are comminution and the combination of nucleation and growth (Vicent, 2005). In the former method, mechanical work is applied on the system, that is, there is an increase in free energy of the system. Examples of comminution processes are the use of shear force and the cavitation process. On the other hand, the later method consist in a change in a thermodynamic parameter, such as pressure, temperature or concentration. The nucleation and growth occur spontaneously, which means that there is a decrease in free energy. The colloidal dispersion process is generally easily controlled in nucleation and growth than comminution method. Therefore, a better control in the particle size may be achieved (Vicent, 2005).

Some of the types of generators that applies comminution to produce MNB are swirl flow, ejector, cavitation, pore, mechanical agitation and sonication (use of ultrasound waves) (Tsuge, 2007b). The description of each type is presented below.

The micro-bubble generator of swirl flow type was patented by Ohnari (2007). It is composed by a cylindrical tank, with one entrance on the upper lateral to the water, which enters tangentially to the wall of the tank; and another opening in bottom for the air entrance. The air is sucked by the negative pressure caused by the water rotating flow. The micro-bubbles are generated by the high

rotating velocity in the mixture of air and water and they come out of the tank from an opening on the top. Li and Tsuge (2006b) has suggested an improvement in this method, by introducing the air in the pump that leads the water to the tank, in order to mix the air with water before entering the generator. With this, smaller bubbles (mininum 52 μm) and 30 to 60% higher gas holdup were obtained.

A micro-bubble generator of ejector type was projected by Aura-tec Company (Auratec and Yahiro, 2001). The ejector scheme is shown in Figure 2.1. The liquid enters the ejector and pass through a narrow tube. With the consequent increase in velocity, the pressure decrease, according to the Bernoulli Theorem. The air is then suctioned by the negative pressure. In the section in which the cross-sectional area is expanded, the turbulent flow and the cavitation effect produce fine bubbles. The bubble production is intensified when the flow leaves the ejector (Tsuge, 2007b).

A similar generator was suggested by Sadatomi et al. (2005), using a spherical body in a tube to create a high shear force in the water flow, as the same time the air was automatically suctioned from small holes on the pipe wall. The authors pointed the low energy consumption and the low manufacturing costs as the merits of this generator. However, the average bubble diameter of the bubbles was quite big, from 120 μm to 490 μm.

In the cavitation process, the vapor bubbles are formed in a region where the hydrostatic pressure in liquid becomes lower than the vapor pressure. Micro-bubbles are formed after the cavitation process, when the pressure is recovered in a short time and the vapor bubbles shrink (Tsuge, 2007b). Serizawa et al. (2003) compared different types of micro-bubble generators (swirl flow, ejector, static mixer) and found out that the cavitation type could produce smaller bubble diameter, lower dispersion of bubble size and higher bubble number density.

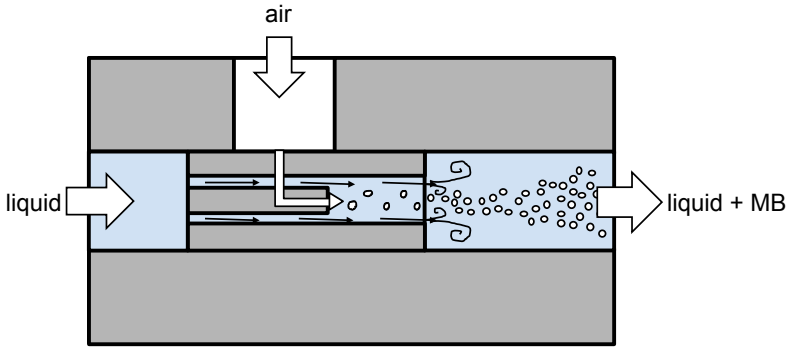

Figure 2.1: Micro-bubble generator ejector type (Aura Tec Co. Ltd.)

Methods using pores such as microchannels (Yasuno et al., 2004) or porous glass membranes (Kukizaki and Goto, 2006) to produce monodispersed bubbles were reported. In the former study, micro-bubbles of 33.6 μm to 51.1 μm mean diameter were obtained, while in the latter, 360 to 720 nm mean diameter nano-bubbles were described. However, in this studies, surfactants were used. The possibility of using these methods in pure water was not informed.

Xu et al. (2008) compared the use of mechanical agitation and sonication methods to produce micro-bubbles in a system containing surfactants. The sonication method showed to be a more efficient method, evaluated through a higher gas hold-up (about 0.4) and smaller bubble diameters (46 μm) in comparison to the mechanical agitation (0.1 and 72 μm, respectively).

The nucleation and growth processes to produce MNB can be done by reducing pressure or by increasing temperature to create a gas-supersaturation condition.

Fujikawa et al. (2003) proposed a micro-bubble generator using a combination of high shear force followed by gas supersaturation condition to nucleate micro-bubbles. In this method, when the air passed through the pores of a porous plate, the rotation of this plate promoted a shear force that teared the gas in the form of 400 μm to 800 μm diameter bubbles. The water with bubbles passed through a five stages channel for promoting turbulent flow and gas dissolution. At last, a gas supersaturation condition was created by a pressure drop, when the water went through a pressure reduction valve. Under this condition, the dissolved air separated from the water in the form of micro-bubbles. According to the authors, the method of consecutive dissolution and nucleation of bubbles in water results in lower bubble diameter and higher number density of bubbles. This generator produced micro-bubbles with average diameter of approximately 20 μm.

A different method for obtaining a gas supersaturated water was suggested by Najafi et al. (2007). Instead of changing the pressure, the authors used a rapid increase in temperature to nucleate the bubbles. The advantage of this method is the non-necessity of high pressure equipments and the easiness in controlling the number of bubbles. In this study, nano-bubbles of 290 nm average diameter were obtained.

In addition, nano-bubbles can be generated through nucleation of hydrogen and oxygen produced by electrolysis in the solid-liquid interface (Kikuchi et al., 2009; Wu et al., 2008). Kikuchi et al. (2009) reported the generation of nano-bubbles in the order of tens and few hundreds nanometers. The advantage of this method is that the size of nano-bubbles can be easily controlled by the applied current.

The different techniques to produce micro- and nano-bubbles may be appropriate for specific purposes. Factors such as bubble size and dispersion, energy consumption, liquid flow and so on are important to select a desired method.

In this study, a method that combines high shear force promoted by a pump with gas nucleation and growth caused by a rapid drop of pressure was selected to produce small bubbles at high efficiency.

2.2 Materials and Methods

2.2.1 Water

Micro- and nano-bubbles were generated in water from three different sources: distilled water, ultrapure water obtained by a water purification system and commercial ultrapure water. The use of each water was dependent on the generator in which bubbles were produced, because of the water volume availability, and on the analysis the water was subjected, based on the water purity.

The distillation process can separate some impurities such as minerals and microorganisms from the water by vaporization, but it can not ensure a complete separation of water and other materials. The distilled water was produced in a distillation unit (Autostill WA-53, Yamato Scientific Co., Ltd., Japan), which is equipped with a water storage tank of 40 L capacity. This high storage capacity allowed to work with high volume with water. This water was used only to produce micro- and nano-bubbles to the preliminary measurements of proton NMR relaxation time (Section 5.3.1).

Ultrapure water was obtained using a water purification system (Direct-Q, Nihon Millipore Ltd., Japan), which is eqquiped with a reverse osmosis cartridge and modules of ion-exchange resins and activated carbon. This system can reject more than 99% of the particles, microorganisms and organic matter (molecular weight above 100 Da). According to the instrument specification, the resistivity of the water treated in this system can reach 182 kΩ-m at 25°C. The water storage capacity of the system is 5 L. The high level of purity of ultrapure water was adequate to use it in measurements of particle size distribution. This water was used to produce bubbles for the particle size distribution and most of the NMR measurements.

Commercial ultrapure water (Kanto Chemical Co. Inc., Japan) has a very strict control of the water purity and was used only to produce bubbles for the zeta potential measurements, when a

very high level of purity was needed. The water was packed in a 1 L bottle.

2.2.2 Gas

The gases used to produce MNB were oxygen (O_2, purity 99.999%, Nissan Tanaka Co., Japan), air, xenon (Xe, purity 99.995%, Iwatani Sangyo Co. Ltd., Japan), nitrogen (N_2, purity 99.9995%, Nissan Tanaka Co., Japan), carbon dioxide (CO_2, purity 99.995%, Nissan Tanaka Co., Japan). In the case of the use of air, in Nikuni Micro-bubble Generator, it was just left opened the gas inlet to the atmosphere; in Aura-tec Micro-bubble Generator, an air filter was set in the gas inlet.

The focus in this study was the micro- and nano-bubbles produced with oxygen (O_2 MNB), so it was used to produce micro- and nano-bubbles in all experiments. The other gases were also used to produce micro- and nano-bubbles for the ζ-potential measurements (air and N_2 MNB), particle size distribution (air MNB) and NMR relaxation time measurements (Xe, N_2 and CO_2 MNB).

2.2.3 Bubble Generation

Two different micro- and nano-bubbles generators were used. Both generate MNB using the same principle: the gas is introduced in the inlet part of the pump and the mixture of water and gas is subjected to a high pressure to increase the dissolution of gas into the water. When the water is released under atmospheric pressure, the depressurization of the gas-supersaturated water leads to the nucleation of the bubbles. The water is circulated in this system for 40 min at 20°C constant temperature. In this study, the water obtained after this procedure is referred as “MNB water”.

The Nikuni micro-bubble generator shown in Figure 2.2 is equipped with a 10 L feed and reservation tank, a centrifugal pump (M20NPD04Z, Nikuni Co., Japan) connected to a pressurized tank (0.4 MPa). The pressure release is controlled by a pressure regulator valve. The gas is introduced at flow rate of 0.3 Nl·min^{-1} (Nl: normal liter at 20°C standard temperature and 0.101 MPa standard pressure). The feed and reservation tank has a double jacket connected to a cooler (C-330, Sibata Scientific Technology Ldt., Japan). In the Nikuni micro-bubble generator, bubbles were mainly produced in distilled water because this system requires a large volume of water. The volume of water used in the experiments was 10 L. However, other 30 L was needed to clean the generator system before the experiment.

On the other hand, Aura-tec micro-bubble generator (OM4-GP-040, Aura Tec Co. Ltd., Japan)

can operate at a lower volume (Figure 2.3). The volume of water was set to 2 L in the case of the ultrapure water produced by the water purification system. When commercial ultrapure water was used, the volume was 1 L (Section 3.5). In addition, in one experiment of NMR relaxation time, bubbles were generated in 1 L of manganese ions solution prepared with ultrapure water produced by Direct-Q system (Chapter 5). This micro-bubble generator is composed by a magnetic gear pump (MDG-R2RVA100, Iwaki Co. Ltd., Japan) and a pressurized tank (0.25 to 0.27 MPa). In addition, a nozzle of ejector type was attached in the outlet (Figure 2.1, but without the air inlet). The mechanism of the nozzle is the Venturi effect: the pressure decreases resulted by the fluid velocity increase when it flows through the constricted section tube. With the pressure drop, bubbles are nucleated from the supersaturated water and micro- and nano-bubbles are dispersed in the water. Two kinds of nozzle were used: one have a single stage Venturi tube (referred to as "single stage nozzle") and the other is composed by a two-stage Venturi tube (referred to as "double stage nozzle"). The latter can reach a lower pressure, which increases the nucleation of bubbles and, therefore, should produce a higher amount of bubbles than the former nozzle. The gas flow rate was set at 0.1 Nl·min^{-1} (20°C, 0.101 MPa) and the water temperature was controlled by a water bath (NTT-1300, Tokyo Rikakikai Co. Ltd., Japan).

Before the experiments, the micro-bubble generator was cleaned by circulating the water for 10 min three times, exchanging water after each circulation. In the case of commercial ultrapure water, the first two cycles were done with ultrapure water produced by the Direct-Q system and only the last cycle was done with commercial ultrapure water.

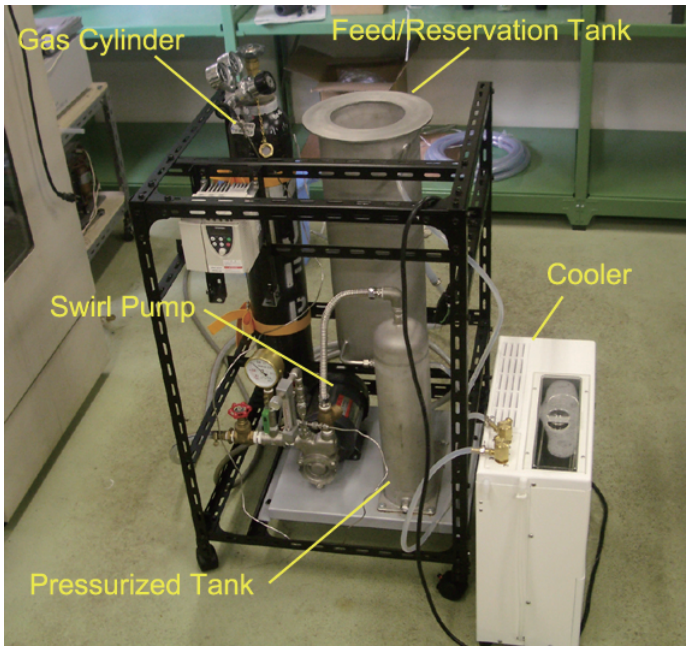

Figure 2.2: Micro-bubble generator system (Nikuni Co.)

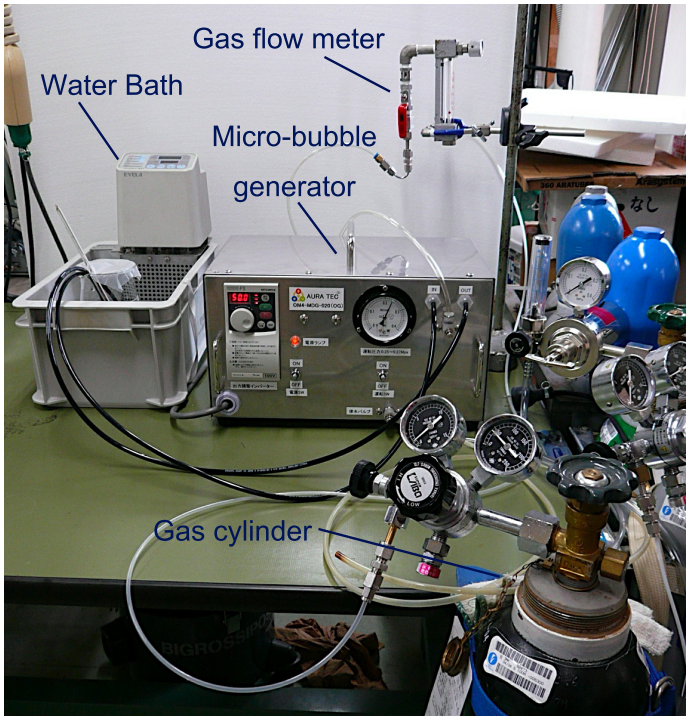

Figure 2.3: Micro-bubble generator system (Aura Tec Co. Ltd.)

Chapter 3

Characteristics of Water with the Generation of Micro- and Nano-bubbles

3.1 Introduction

In this chapter, some basic characteristics of the water with the generation of MNB will be presented. The characteristics include qualitative information about macroscopic and microscopic bubbles, which was obtained through visual appearance and observation in microscope; and quantitative data obtained through measurements of DO concentration, pH and zeta potential.

3.2 Appearance of the water with the Generation of Micro- and Nano-bubbles

The appearance of the water with the generation of MNB in both generators (Nikuni and Auratec) was similar. During the bubble production, the water had a milky appearance, resulted of the light scattering effect of the micro-bubbles (Figure 3.1a). This appearance was observed just a few seconds after starting the micro-bubble generation and was maintained during the whole bubble production period. When the bubbling stopped, the milky appearance gradually vanished. In about 5 min, the water became transparent (Figure 3.1b to Figure 3.1d). The presence of nano-bubbles, however, could not be verified through simple visual observation, as they can not be seen with naked eye.

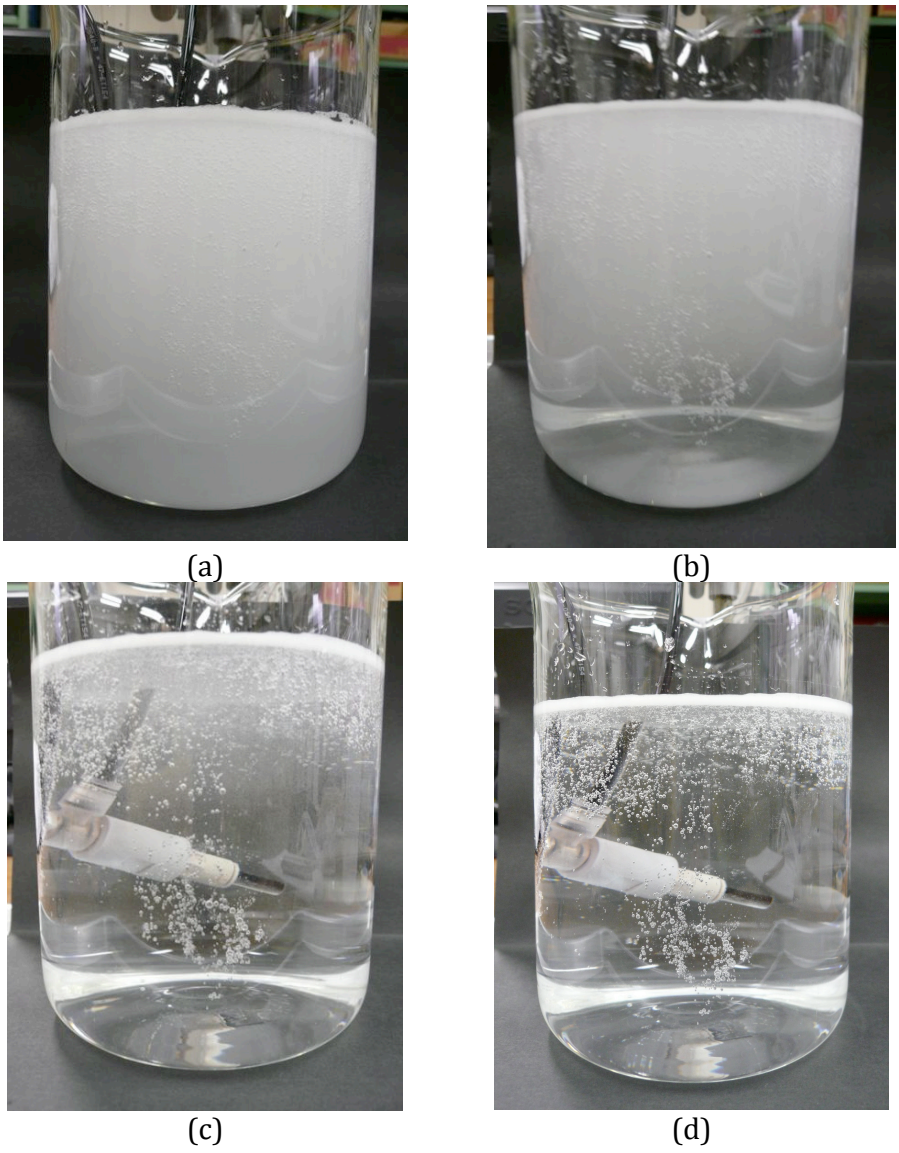

Figure 3.1: Appearance of the O_2 MNB water (a) during the bubble generation and after stopping the bubble generation at different times: (b) t = 3 min; (c) t = 4 min; (d) t = 5 min

3.3 Observation in Microscope

3.3.1 Materials and Methods

Just after the production of the O_2 MNB water, one drop of this water was placed on a glass slide and observed through a optical microscope (BH-2, KS Olympus Co. Ltd., Japan). The image of micro-bubbles was recorded by a Fujix Digital Camera (HC-300Z, Fujifilm, Japan).

3.3.2 Results and Discussion

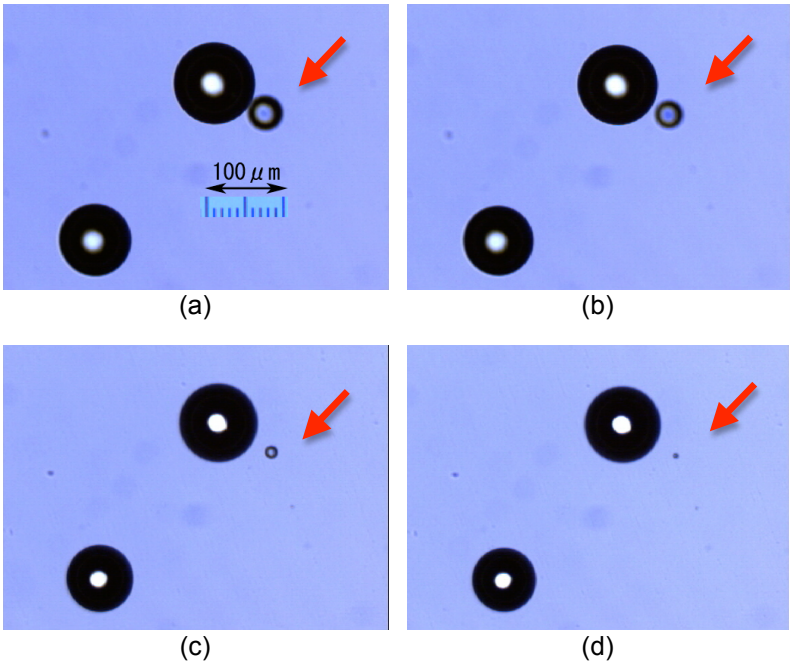

Figure 3.2: Images of micro-bubbles obtained through optical microscope. The shrinking of a micro-bubble (indicated by the red arrow) is observed from images (a) to (d). The total elapsed time was 36 s.

Through the observation of the droplet of O_2 MNB water through optical microscope, bubbles of diameter in the range from 10 to 100 μm were observed. Larger bubbles (diameter approximately 100 μm), trapped in the drop of water, stayed still during almost entirely the recording time (approximately 2 h). In a case of a large volume of water with a flat surface, these bubbles would probably rise up to the surface and explode.

On the other hand, smaller bubbles, with diameter of around 50 μm, showed the tendency to shrink until a limit size that was not possible to be observed through the microscope. The images

of a micro-bubble shrinking with time is shown in the sequence from Figure 3.2a to Figure 3.2d, in which the elapsed time between the first and last image is 36 s. Based on this observation, two possibilities were considered regarding the shrinking bubbles: the bubble would have collapsed at the last moment (Figure 3.2d) or stabilized as nano-bubble.

3.4 DO concentration and pH

3.4.1 Materials and Methods

DO (dissolved oxygen) concentration and pH were measured simultaneously in water samples taken during and after the generation of O_2 MNB, as shown in Figure 3.3.

Figure 3.3: Measurement of DO concentration and pH.

The O_2 MNB water was prepared at four different conditions, as described in Table 3.1.

The DO concentration was determined using a DO meter (SG6, Mettler-Toledo GmbH, Switzerland). This instrument has a high performance oxygen sensor, which detects oxygen concentration from 0 to 99 mg·L^{-1}. The accuracy of this DO meter is $\pm 0.5\%$. All the measurements were done in the water samples at a controlled temperature of 20°C. However, when there was some small

Table 3.1: Generation conditions of O_2 MNB water to measure DO concentration and pH.

Micro-bubble Generator	Volume of water (L)	Nozzle
Nikiso	10	none
Aura-tec	10	single stage
Aura-tec	2	single stage
Aura-tec	2	double stage

variations in the actual temperature, the DO concentration was corrected to 20°C using a correction factor for oxygen solubility (Lewis, 2006).

The pH was measured by a pH meter (D-55, Horiba Ltd., Japan). The measurement range of this pH meter is from 0 to 14 with accuracy of ± 0.01. The pH meter was set to compensate automatically the pH values at 20°C.

After the bubble generation, when the O_2 MNB water was produced in the 10 L tank, the water was kept in the tank covered with an acrylic lid. The cooler attached to the tank was set to 20°C. In the case the water was prepared in a 2 L beaker, it sealed with Parafilm (Pechiney Plastic Packaging, USA) and kept in a 20°C constant temperature room. DO concentration and pH were measured daily until they reached the equilibrium.

3.4.2 Results and Discussion

Figure 3.4 show the DO concentration of the O_2 MNB water during the bubble generation. The DO concentration of the water, which initially ranged from 8.1 to 10.3 mg·L^{-1}, rapidly increased to high levels of approximately 35 to 45 mg·L^{-1}, characterizing a gas supersaturated water.

In most conditions, it was observed that in the first measurement after starting the bubble generation (5 or 10 min), the DO concentration was already at the maximum DO concentration, which was kept during the whole bubble generation period. The exception was the O_2 MNB water produced by the Aura-tec micro-bubble generator in a 10 L of water. This generator has a lower flow rate than the Nikuni micro-bubble generator (1.8 to 2.1 L·min^{-1} against 40 L·min^{-1}, respectively). Consequently, when the former generator worked at a high volume such as 10 L, the time taken to DO concentration reaches the maximum value was longer. Only after 20 min it reached the maximum DO concentration.

The value of the maximum DO concentration has also varied with the operating conditions.

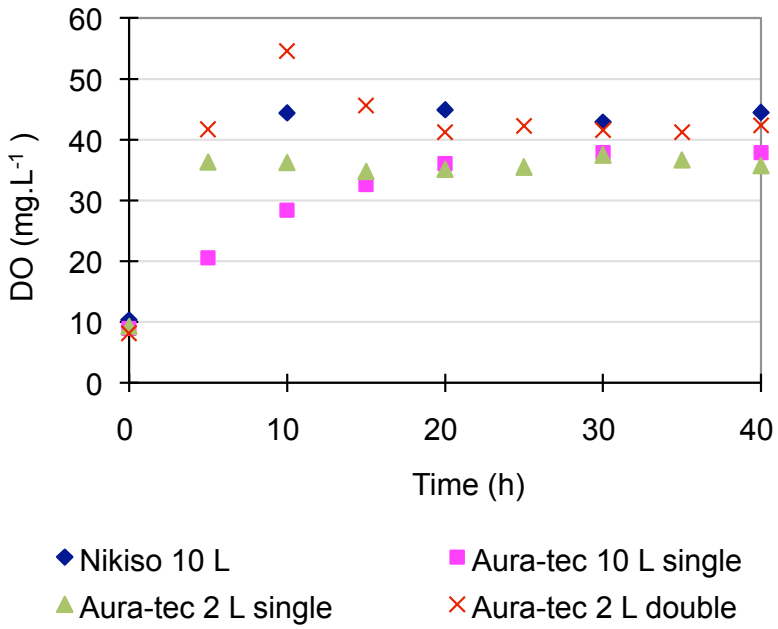

Figure 3.4: DO concentration measured during the bubble generation at different conditions: type of micro-bubble generator (Nikuni and Aura-tec), type of nozzle (single and double) and water volume (2 L and 10 L).

Nikiso micro-bubble generator and Aura-tec micro-bubble generator with the double stage nozzle seems to dissolve oxygen at a higher level (40 to 45 mg·L^{-1}), while the O_2 MNB water produced with Aura-tec micro-bubble generator with the single stage nozzle presented DO concentrations at a lower level (35 to 38 mg·L^{-1}). The higher oxygen dissolution capacity of Nikiso micro-bubble generator is due to the higher pressurization applied to the mixture of water and gas (0.4 MPa) comparing to the Aura-tec generator (0.25 to 0.27 MPa), which means a higher dissolution of gas into the water. However, when the Aura-tec micro-bubble generator was operated with the double stage nozzle, similar DO concentration was reached, because of the high gas dissolution capacity of this nozzle.

After stopping the bubble generation, the DO concentration decreased gradually until reached the saturation equilibrium (Figure 3.5). The O_2 MNB water produced by Aura-tec generator with single stage nozzle showed the fastest recovery to the equilibrium state. Considering the equilibrium DO concentration as 10 mg·L^{-1}, the time to reach it was 3 d. The O_2 MNB water produced with the same volume (2 L) of water but with a double stage nozzle could extend the time to the equilibrium condition to 7 d, because the initial DO concentration was higher.

In addition, the initial volume of water was also important to keep the DO concentration higher

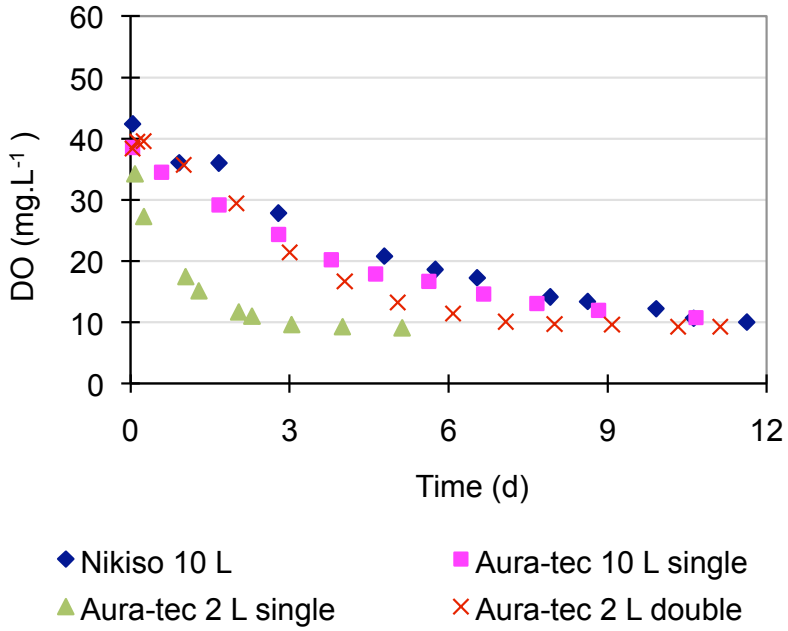

Figure 3.5: DO concentration measured after the bubble generation at different conditions: type of micro-bubble generator (Nikuni and Aura-tec), type of nozzle (single and double) and water volume (2 L and 10 L).

for a longer time. With a larger volume, the ratio of gas exchange surface area to the volume of water is lower. Comparing the O_2 MNB water produced in the Aura-tec generator with single stage nozzle in volumes of 2 L and 10 L, it was verified that the 10 L volume water could hold the DO for a longer time, reaching the equilibrium condition only after 11 d, against 3 d in the case of 2 L of water. In this case, the 2 L beaker had a ratio of gas exchange area to volume of 7.7 m^{-1} and the 10 L tank, the ratio was 2.0 m^{-1} (data for the calculation: diameter of the beaker = 14 cm; diameter of the tank = 16 cm).

In a large volume of water, the DO concentration decreasing rate did not depend much on the initial DO concentration, as observed in the case of the O_2 MNB water produced by Aura-tec and by Nikiso micro-bubble generator, both in 10 L of water. Although the MNB water produced by Nikiso generator had a higher initial DO concentration, the curves of DO concentration with time were similar. The time to reach the saturation equilibrium in the MNB water produced by Nikiso generator was 12 d, which was similar to the 11 d observed in the MNB water produced by Aura-tec generator. Therefore, the time necessary to the DO concentration reach the equilibrium state was also dependent on the initial DO concentration but mainly to the ratio of the gas-water exchange area to the water volume.

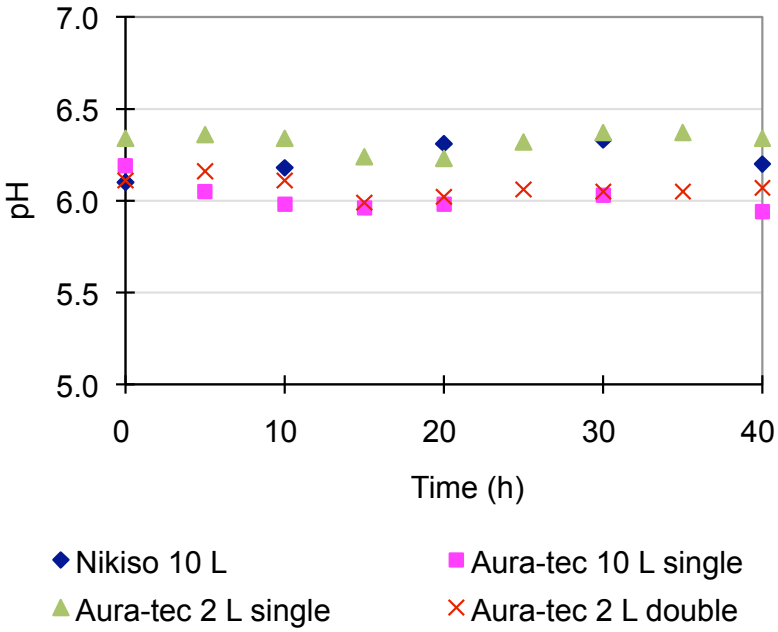

Figure 3.6: pH measured during the bubble generation in different micro-bubble generators (Nikuni and Aura-tec), nozzles (single and double) and water volume (2 L and 10 L).

There are few data in literature which shows the DO concentration of O_2 MNB water, mainly concerning the oxygen concentration change with time. Most of the studies in the literature report the DO concentration of water with air MNB. Values up to 9.8 mg·L^{-1} at 28.5°C (Fujikawa et al., 2003) and up to 12 mg·L^{-1} (Yamada et al., 2007) at 20°C were reported in air MNB water. Sadatomi et al. (2005) observed an increase in DO concentration from 7 mg·L^{-1} to approximately 8.3 mg·L^{-1} when 490 μm diameter bubbles were produced and to about 8.9 mg·L^{-1} with 120 μm diameter bubbles production. The temperature was between 11.5 and 15.5°C. The latter study shows the advantage of smaller bubbles in dissolving into the liquid because of their larger specific area and longer residence time.

The use of air to produce MNB is more economical and practical in many applications. However, for the study of the dissolution of gas with the MNB production, the use of pure oxygen is more appropriate.

A more detailed study measuring oxygen concentration was reported by Kikuchi et al. (2009). Oxygen nano-bubbles were produced by electrolysis and oxygen content of the water was measured using different methods: 10-fold dilution and Winkler method and by a DO meter. It was found that the DO meter can measure only the dissolved oxygen in the solution, while 10-fold dilu-

tion and Winkler methods can detect the total amount of oxygen, including the oxygen in the form of nano-bubbles. For example, in an oxygen saturated electrolyte, the DO concentration was about 1 mM (32 mg·L^{-1}), while the overall oxygen content obtained by Winkler method was about 3 mM (96 mg·L^{-1}). The results indicate that approximately 2 mM (64 mg·L^{-1}) was correspondent to the oxygen nano-bubbles.

In comparison with the present study, it can be observed that the DO concentration measured by the DO meter in Kikuchi et al. (2009) is similar to the oxygen MNB water produced with the single-stage nozzle. This value, therefore, does not include the bubbles in the form of nano-bubbles.

Regarding the pH measurements, no variation was observed during the production of bubbles (Figure 3.6). The values of pH were in the range between 5.96 and 6.45. However, no tendency of increasing or decreasing pH was observed.

Figure 3.7 show the pH of the O_2 MNB water with time. The pH of most of the MNB water samples did not increase or decrease with time and fluctuated between 6.10 and 6.65. The MNB water produced by Aura-tec generator with the double stage nozzle was the only sample which showed a tendency of decreasing pH with time. The pH just after stopping the bubble generation was 6.07 and decreased to 5.62 after 10 d. There could have been some contamination with microorganisms, which made pH decrease. However, the difference between the initial and final pH is very small and it could be just some fluctuation of the measurements.

An increase in pH with the bubbling time was reported by Himuro (2007b). The pH varied from about 6.9 to 7.5 in 5 hours of air bubbling at 25°C. After that time, the pH was constant. According to the authors, the difference in pH may be related to the control water. The water used in that case was tap water, which contains carbon dioxide and chlorine naturally dissolved, which contributes to low the pH. With the bubbling, these compounds would be expelled from the water and the pH would increase. In the present study, the water used to produce the bubbles is subjected to a very strict purification procedure, which can eliminate those compounds.

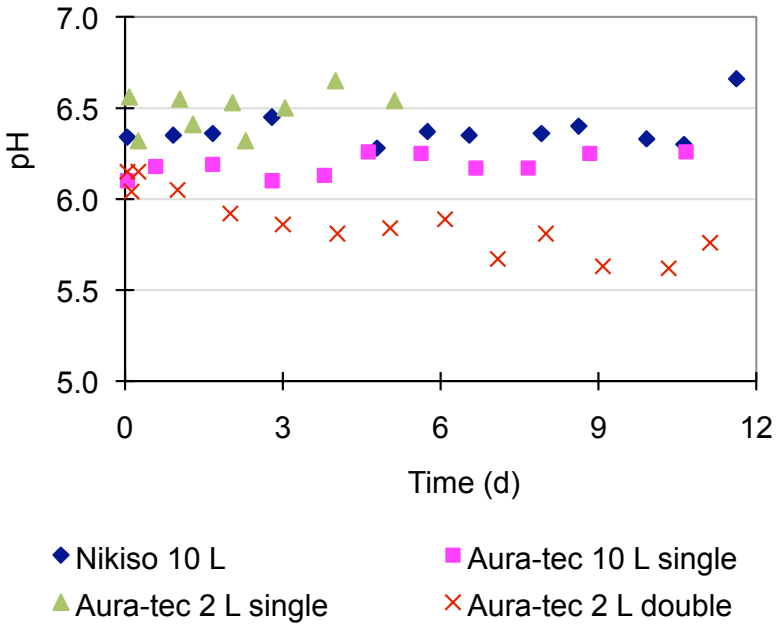

Figure 3.7: pH measured after the bubble generation in different micro-bubble generators (Nikuni and Aura-tec), nozzles (single and double) and water volume (2 L and 10 L).

3.5 Zeta Potential

In a liquid, electrically charged particles attract counterions that are adsorbed on their surface (Figure 3.8). These ions are very closely attached on the particle surface and they compose the called *Stern layer*. Further away from the particle, there are counterions loosely bound, which form a *diffuse layer*. These ions move with the particle but are not adsorbed on the surface. The two layers are referred to as the *double layer*. The boundary of the diffuse layer with the ions that do not move with the particle is called *slipping plane*. The electrostatic potential between the slipping plane and the bulk solution is called ζ*-potential* (zeta potential) (Malvern, 2004).

The magnitude of ζ-potential indicates the stability of the colloidal systems. The DLVO (Deryaguin-Landau-Verwey-Overbeek) theory states that the balance between the attractive Van der Waals forces and the repulsive electrical forces due to the surface charge is decisive for the stability of the colloids. Therefore, high absolute values of ζ-potential means that the repulsive electrical forces have a high potential to be dominant in relation to the Van der Waals forces, resulting in a stable particle dispersion.

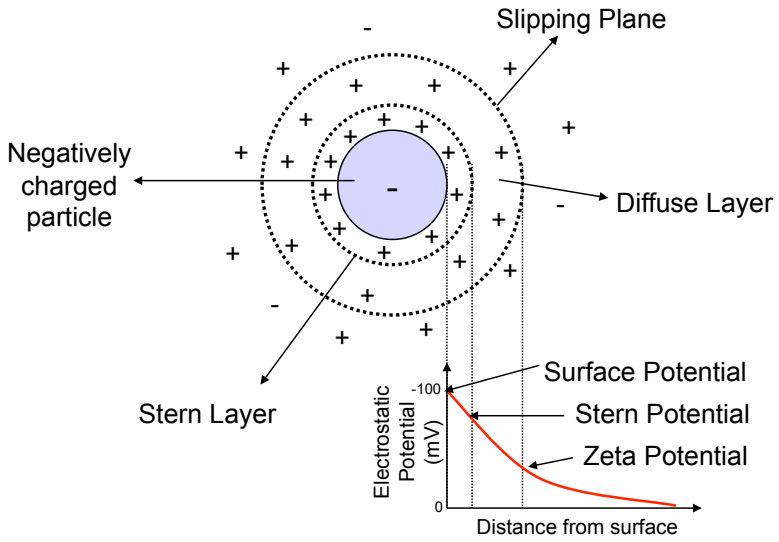

Figure 3.8: Description of a charged particle, the double layer formed by the Stern layer and the diffuse layer and the definition of ζ-potential. Source: Malvern (2004).

The most convenient method to calculate ζ-potential for dispersed colloidal particles is the electrophoretic mobility. The electrophoretic mobility is defined as the ratio of the induced velocity of the particles to the applied electric field strength (Yezek, 2002).

The Henry equation (Henry, 1931) relates the electrophoretic mobility and the ζ-potential:

$$\zeta = \frac{6\,\pi\,\eta}{\epsilon\,f(\kappa\,a)}\,U \tag{3.1}$$

where ζ is the ζ-potential (V), η is the viscosity of the medium (Pa·s), ϵ is the dielectric constant (F·m^{-1}), $f(\kappa\,a)$ is the Henry's function and U is the electrophoretic mobility ((m/s)·(V/m)$^{-1}$), which is calculated as:

$$U = \frac{\nu}{V/L} \tag{3.2}$$

where ν is the particle speed (m·s^{-1}), V is the voltage (V) and L is the distance of the electrode (m).

Henry's function varies from 1.0 for small κa and 1.5 for large κa. The value of κa is related to the double layer thickness. Large κa indicates a thin double layer, which is the case of aqueous colloidal systems.

For measuring ζ-potential in aqueous media, when f(κa) is 1.5, the Equation 3.1 is reduced to

Smoluchowski equation (Smoluchowski, 1914):

$$\zeta = \frac{4\,\pi\,\eta}{\epsilon}\,U \tag{3.3}$$

The difficulty of measuring ζ-potential of bubbles was reported in many studies. The biggest problem is the rising velocity of the bubble, as ordinary macro-bubbles remain in the water just for a fraction of a second. One alternative for the measurement of ζ-potential in bubbles was to follow the rising movement of the bubble, for example, by moving the lens of the microscope at the same speed as the vertical movement of the bubble. Another possibility is to reduce the size of the bubble until the rising velocity of the bubble decreases to a level that its electrophoretic mobility can be measured (Takahashi, 2005; Graciaa et al., 2002).

In addition, it is also difficult to obtain exactly the value of ζ-potential in pure water with air bubbles, because the water is easily contaminated with some surface active agents present in the water, in the measurements apparatus or in the atmosphere (Graciaa et al., 2002). Therefore, it is very important to assure the purity of the water, as well as to avoid contamination in the measuring cell during the procedure.

3.5.1 Materials and Methods

ζ-potential measurements were performed using a Zeta Potential Analyzer (Zeecom, Microtech Co. Ltd., Japan). This system detects the electrophoretic mobility of particles and is equipped with a microscope and a CCD camera to observe the movement of particles in the range of 20 nm to 100 μm. The small particles can be observed by the scattering of a halogen light or laser. The sample was measured in a glass cell of 1 mm $\times$ 10 mm dimension. The sample volume was 8 mL and the distance between the electrodes was 9 cm. The voltage was set to 30 V. Fifty particles were tracked manually to determine their speed and the ζ-potential was calculated using Smoluchowski equation (Equation 3.3).

The ζ-potential was measured in O_2 MNB water during 6 d. The measurements in air MNB and N_2 MNB water samples were done only during the first hours after the bubble production until 1 d later, in order to compare ζ-potential in systems with different gases.

3.5.2 Results and Discussion

The ζ-potential measured in O_2 MNB water with time is presented in Figure 3.9. The results show that the ζ-potential of of O_2 MNB water was negative, with values from -44 to -34 mV. The absolute value higher than 30 mV indicates that the electrical charged particles tend to repel each other, avoiding the aggregation of particles (Spanos et al., 2002). In the case of O_2 MNB water, the high ζ-potential value may support the stability of bubbles by avoiding the bubble coalescence.

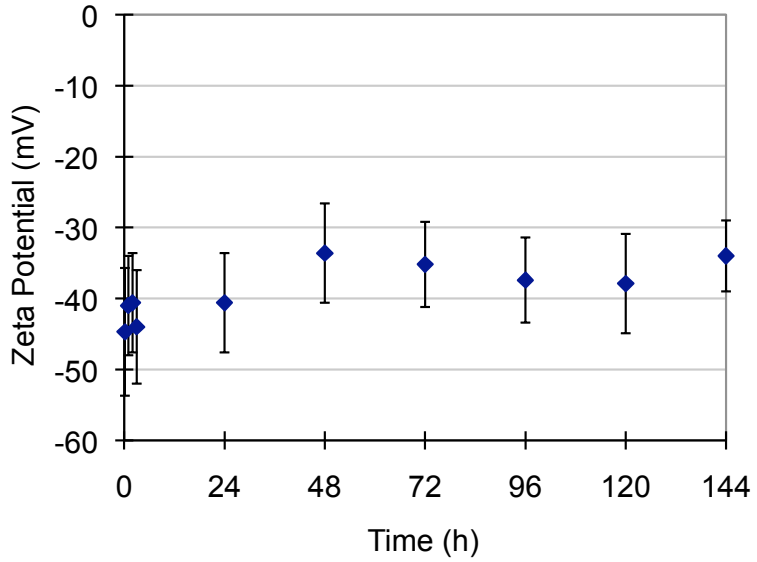

Figure 3.9: Average values of ζ-potential of O_2 MNB water with time ($n = 50$). The vertical bars show the standard deviation of the measurements.

In the measurements performed in the first 4 h, ζ-potential presented absolute values in the range from 40 to 44 mV. The absolute value seem to decrease with time, reaching to 34 $\pm$ 7 mV on the second day, followed by a slightly increase up to 38 $\pm$ 7 mV on the fifth day of measurement. However, on the following day, the average value dropped to 34 $\pm$ 5 mV. It is probable that the variation of the ζ-potential with time after the second day was just a fluctuation of the measurements. However, there was a difference between the first measurements until the first day and the following measurements. The charge of particles just after the bubble generation was higher in absolute value, and it decreased with time. Still, the ζ-potential was kept at a high absolute value (higher than 30 mV) until the last measurement. This could be related to the high concentration of bubbles electrically charged in the early period after the bubble generation. From the second day, there could have been a slight decrease in the concentration of bubbles, but some

remained stable until the last measurement, after 6 d.

The DO concentration and pH of the O_2 MNB water sample taken at the same time as the measurement of ζ-potential can be observed in Figure 3.10. The measurement of pH is important because ζ-potential value is closely related to pH of the medium. The value of pH fluctuated between 6.2 to 6.4, with no tendency of increasing or decreasing, similarly as observed in Section 3.4.2. The variation in ζ-potential, therefore, was probably not caused by a variation of pH. The DO concentration decreased rapidly already 1 d after the bubble generation, as the initial volume of water was only 1 L. On the second day, the DO concentration already reached about 10 $mg{\cdot}L^{-1}$. Although the DO concentration was near the oxygen saturation equilibrium from this time, the measurement of high negative values of ζ-potential was obtained until the last measurement on the 6th day. This means that the electrical charges could be detected in the water even at low DO concentration.

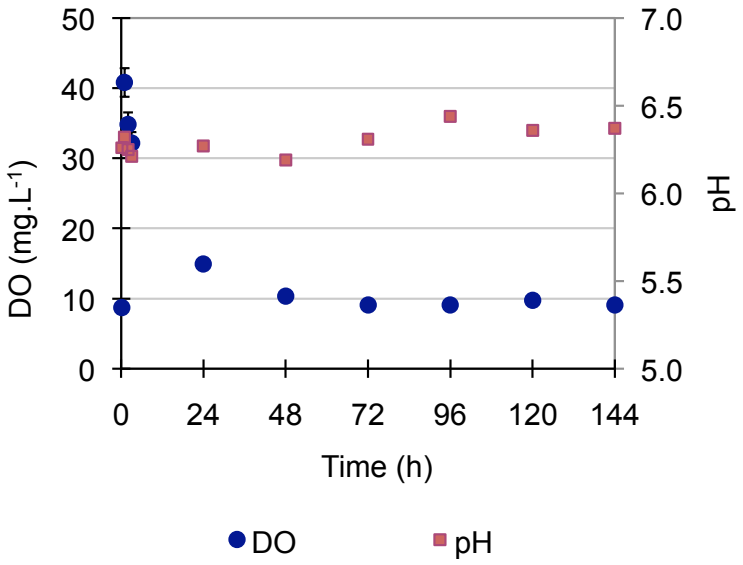

Figure 3.10: DO concentration and pH of the O_2 MNB water measured on the same time as the measurements of ζ-potential. Vertical bars show the accuracy of the instrument (when not shown, error is smaller than the marker).

One important point to observe is that, during the measurements of the particle mobility, although the velocity of the particles did not seem to vary with time, the amount of particles did. Therefore, the charge of the particles remained practically constant, but the concentration of particles or bubbles should be decreasing with time (qualitative data).

The measurements of ζ-potential in air MNB water and N_2 MNB water also indicated neg-

ative values. However, lower absolute values were observed comparing to the O_2 MNB water (Figure 3.11). In the measurement of air MNB, absolute ζ-potential fluctuated from 28 $\pm$ 7 mV in the first hour after the bubble production (pH 6.2) to 33 $\pm$ 12 mV, 1 d later (pH 6.5). The N_2 MNB showed even lower absolute ζ-potential, varying from 26 $\pm$ 7 mV in the first hour (pH 5.7), droping to 17 $\pm$ 6 mV in 2 h (pH 5.8) and to 12 $\pm$ 6 mV after 1 d (pH 6.0).

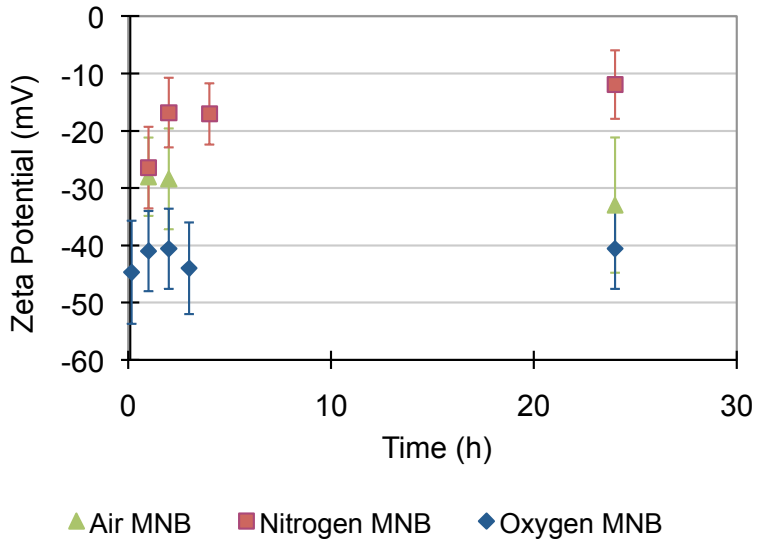

Figure 3.11: Average values of ζ-potential measurements in O_2 MNB water, N_2 MNB water and air MNB water with time ($n = 50$). The vertical bars show the standard deviation.

According to Spanos et al. (2002), the absolute ζ-potential value normally taken as a minimum to observe a potential stability is 30 mV. Therefore, the O_2 MNB could be stabilized in water by the electrically charged surfaces, justified by the high ζ-potential measured. On the other hand, the air MNB are in the limit of the stabilization by repulsion forces and the N_2 MNB would probably not be stable at the measured conditions.

In literature, Graciaa et al. (1995) reported a ζ-potential of -65 mV in air bubbles formed in deionized water, while (Usui and Sasaki, 1978) obtained an average value of -15 mV as the ζ-potential of argon bubbles in distilled water. According to Graciaa et al. (2002), the big disparity in results in literature is due to the differences in the purification methods of the water. In all the reports, however, the value of ζ-potential was negative, in agreement with the results obtained in this study. The negative value is attributed to the predominance of hydroxide ions in the first molecular layers of water at the gas-liquid interface (Kelsall et al., 1996).

Takahashi (2005) reported a similar result as those obtained in the present study. The author found electric charged micro-bubbles with ζ-potential of -35 mV in distilled water at pH 5.8. With this result, the author concluded that both H^+ and OH^- ions play a very important role in the gas-water interface charge. Furthermore, tests with addition of alcohols (non-electrical charged molecules) in the aqueous solution indicated that the gas-water interface electrical charge is related to the hydrogen bond network at the gas-liquid interface, which has a different structure from that of bulk water. The change in the hydrogen bond is also described by Ohgaki et al. (2010), in which is reported a "hard hydrogen bond" at the gas-liquid interface.

3.6 Conclusion

Based on the visual observation of the water during and after the generation of bubbles, it was verified that the micro-bubbles were rapidly dispersed into the water when the bubbling started. They could be easily seen during the bubble production because of the light scattering effect of micro-bubbles. After the bubble generation stopped, micro-bubbles could be still observed for some few minutes, but they disappeared with time.

From the observation of a drop of O_2 MNB water in optical microscope, it was concluded that micro-bubbles of approximately 100 μm diameter stayed stable during the observation time, while 50 μm diameter micro-bubbles tended to shrink in about 30 s.

The DO concentration increased at a very high level in a short time with generation of MNB. The maximum DO concentration varied from 35 to 45 mg·L^{-1}, depending on the micro-bubble generator and on the type of nozzle. After stopping the bubble generation, the DO concentration decreased until it reached the saturation equilibrium. The time to reach the saturation equilibrium depended on the initial DO concentration after stopping the bubble generation and on the ratio of the water surface to the volume of water. On the other hand, the pH did not change either with the generation of bubbles or with the time after the bubble generation stopped.

Finally, the negative ζ-potential in O_2 MNB water indicated the presence of electrically charged particles. The averages values measured at different times were high enough to keep the particles stable. Even after 6 d after the bubble generation, the ζ-potential absolute value was still higher than -30 mV. This result could help the stability of bubbles in water by avoiding their coalescence.

Chapter 4

Particle Size Distribution

4.1 Introduction

There are several methods to measure the particle size in a colloidal system, such as microscopy, sedimentation and light interaction methods. However, if the particles in the system are bubbles, the available methods are more restricted. The reason is that the sample can not receive practically any pre-treatment normally used in solid particles system (e.g. centrifugation, dissection).

Methods using optical imaging analysis can be applied to measure bubbles in the micro scale (Xu et al., 2008; Burns et al., 1997). In nano range, atomic force microscopy was used to measure nano-bubbles attached to a solid surface (Bhushan et al., 2008; Tyrrell and Attard, 2002; Wu et al., 2008; Zhang et al., 2006). In aqueous solution, bubble diameter at nano size were measured by scanning electron microscopy (Ohgaki et al., 2010).

Among the methods using light interaction, there are reports of the use of a light-obscuration based particle counter (Takahashi et al., 2003, 2007) and a method based on light transmission (Tabei et al., 2007; Hasegawa et al., 2008) to measure micro-bubbles. The scattering method of laser diffraction can detect bubbles in a wider range, from nano (Kukizaki and Goto, 2006; Kukizaki and Wada, 2008) to micro sizes (Bredwell and Worden, 1998; Couto et al., 2009; Li and Tsuge, 2006b; Xu et al., 2009). In addition, the dynamic light scattering was used to measure nano-bubbles (Najafi et al., 2007; Kikuchi et al., 2009).

The scattering techniques have the advantage to be non-invasive, which allows to determine the particles size in their natural equilibrium state (Richardson, 2008).

The scattering using visible light, which has wavelength between approximately 400 to 600 nm, is normally used to measure particles larger than 10 nm, although smaller particles can also be detected. The detection principle is the different refractive index of the particle and that of the solvent (Richardson, 2008).

The particle size distribution is presented in a histogram, which shows the relative frequency at each size interval. The relative frequency can be expressed in intensity of the scattered light, in volume or in number of particles. As an example, each type of histogram for a solution containing the same amount of 10 nm and 100 nm diameter particles is shown in Figure 4.1. In number distributions, the peaks show the same proportion, as there is equal amount of particles of each size. The peaks of the volume distribution have a difference in the order of 10^3. Since the volume of the sphere is $(4/3)\pi \cdot r^3$ and the diameter of the big particles is 10 times larger than the small particles, the volume is 1000 times greater. Finally, the intensity of a particle scattering is proportional to the sixth power of its diameter (by the Rayleigh's approximation), that is, a big particle scatters light at a much higher intensity than a small one. Thus, in the intensity dispersion, the peak of the big particles is 10^6 times greater than the small particles one.

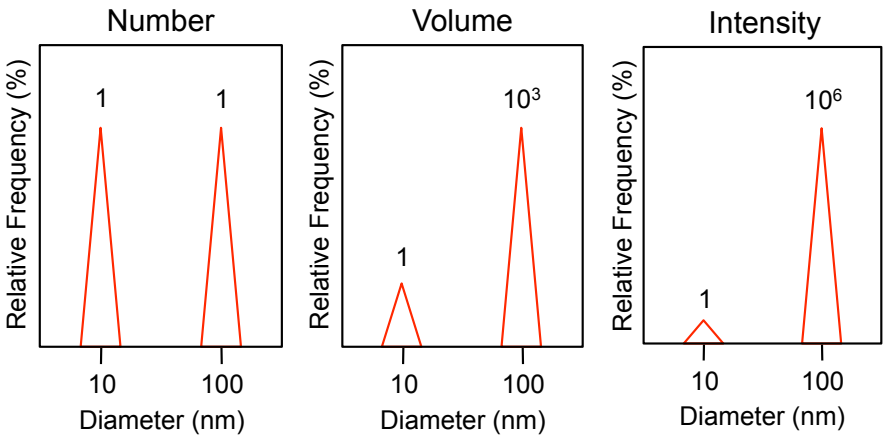

Figure 4.1: Examples of particle size distribution expressed in number, volume and intensity of a solution containing equal amounts of 10 nm and 100 nm diameter particles.

In this study, the particle size distribution of the MNB water was measured by light scattering, using two different principles: laser diffraction and dynamic light scattering. The fundaments and description of each method is described in the following sections.

4.1.1 Laser Diffraction

When a light beam is incident on a particle, it will be scattered in different directions. The laser diffraction method is based on the relation between the angle of the scattered light to the size of the particle.

The Rayleigh theory relates the intensity of the scattered light at an observation angle to the size of the particle. This theory can be applied for isotropic, homogeneous and spherical particles much smaller than the wavelength of the incident light. Using polar coordinates (r, θ, ϕ), the intensity of the scattered light I ($V^2 \cdot m^{-1}$) per intensity of the incident light is given by (Kerker, 1969):

$$\frac{I}{I_0} = \frac{16\pi^4\, a^6}{r^2\, \lambda^4} \left(\frac{n^2-1}{n^2+2}\right)^2 sin^2\psi \tag{4.1}$$

in which a is the radius of the particle (m), r is the distance between the sample and the detector (m), λ is the wavelength of the incident light (m), n is the relative refractive index and ψ is the angle between the plane of polarization of the incident beam and the plane defined by the incident and scattered beams.

However, for particles much larger than the light beam wavelength, Mie theory is more adequate, as it is applied for a more general range of particle size. In Mie theory, the scattering intensity is a function of the angle of the scattered light by particles of arbitrary size (Lyklema, 1991). Mie theory also consider that the particle is isotropic, homogeneous and spherical. Besides, it considers that the particles is in a diluted medium, so there is no interference of the re-scattered lights from other particles (Kerker, 1969).

The solution of intensity of scattered light is resolved in polar coordinates (r, θ, ϕ). With the consideration of the scattered field far from the particle (diluted medium), the radial component can be neglected. The intensities in the ϕ (I_ϕ) and θ (I_θ) polar coordinates are given by (Kerker, 1969):

$$\frac{I_\phi}{I_0} = \frac{\lambda^2}{4\pi^2 r^2}\ |S_1|^2\ sin^2\phi \tag{4.2}$$

$$\frac{I_\theta}{I_0} = \frac{\lambda^2}{4\pi^2 r^2}\ |S_2|^2\ cos^2\phi \tag{4.3}$$

in which S_1 and S_2 are the amplitude functions, defined by:

$$S_1 = \sum_{n=1}^{\infty} \frac{2n+1}{n(n+1)} \{a_n \pi_n(cos\,\theta) + b_n \tau_n(cos\,\theta)\}(-1)^{n+1} \tag{4.4}$$

$$S_2 = \sum_{n=1}^{\infty} \frac{2n+1}{n(n+1)} \{a_n \tau_n(cos\,\theta) + b_n \pi_n(cos\,\theta)\}(-1)^{n+1} \tag{4.5}$$

in which $\pi_n(cos\,\theta)$ and $\tau_n(cos\,\theta)$ are angular functions, expressed by an associated Legendre polynomial and a_n and b_n are coefficients generated by the solution of the wave equations and are functions of α and β, given by:

$$\alpha = \frac{2\pi\, a}{\lambda} = \frac{2\pi\, m_2\, a}{\lambda_0} \tag{4.6}$$

$$\beta = \frac{2\pi\, m_1\, a}{\lambda_0} = m\,\alpha \tag{4.7}$$

where λ_0 is the wavelength in the vacuum (m), λ is the wavelength in the medium, $m = m_1/m_2$ is the complex refractive index of the particle to that of the medium.

In Mie theory, the solution for the scattering of a plane electromagnetic wave by a spherical particle considers both scattering and absorption phenomena. These phenomena cause a reduction in the energy of the incident light, which is described by the extinction concept. The degree to which a particle can scatter and adsorb the electromagnetic radiation is defined by an apparent area called cross section C (m^2). Thus, the extinction cross section (C_{ext}) is defined by the sum of the scattering cross section (C_{sca}) and the absorption cross section (C_{abs}), (Kerker, 1969):

$$C_{ext} = C_{sca} + C_{abs} \tag{4.8}$$

The Mie theory calculation output provides the scattering and the extinction cross sections:

$$C_{sca} = \frac{\lambda^2}{2\pi} \sum_{n=1}^{\infty} (2n+1)\{|\,a_n\,|^2 + |\,b_n\,|^2\} \tag{4.9}$$

$$C_{ext} = \frac{\lambda^2}{2\pi} \sum_{n=1}^{\infty} (2n+1)\{\mathbb{R}(a_n + b_n)\} \tag{4.10}$$

in which $\mathbb{R}$ refers to the real part of the complex number.

These parameters are often expressed as a dimensionless scattering efficiency factor Q, defined by the ratio of the cross section to the actual geometrical cross section ($\pi\, a^2$ for a sphere). Thus, the efficiency factors for scattering (Q_sca) and extinction (Q_ext) are written as:

$$Q_{ext} = Q_{sca} + Q_{abs} \tag{4.11}$$

$$Q_{sca} = \frac{2}{\alpha^2} \sum_{n=1}^{\infty} (2n+1)\{|\, a_n\,|^2 + |\, b_n\,|^2\} \tag{4.12}$$

$$Q_{ext} = \frac{2}{\alpha^2} \sum_{n=1}^{\infty} (2n+1)\{\mathbb{R}(a_n + b_n)\} \tag{4.13}$$

C_{abs} and Q_{abs} are then calculated by the difference of Equation 4.8 and Equation 4.11, respectively.

4.1.2 Dynamic Light Scattering

The Dynamic Light Scattering (DLS) method detects particles due to their the Brownian motion. The speed of the particles is related to their size: small particles move quickly and large particles move slowly. The detection of the particle movement is done by the application of a laser beam in the sample, which will scatter the light in different directions. The movement of the particles generates different scattered light patterns with time, which is detected by the sensor of the instrument. The fluctuations in the scattering intensity with time is analyzed by a digital correlator, which measures the correlation between the patterns. Large particles, which move slower, will generate patterns that fluctuate slowly. On the other hand, small particles, which move fast, will have a pattern that fluctuate quickly. Thus, the speed of particles can be calculated (Malvern, 2004).

The relationship between the particle size, and its speed due to Brownian motion is given by the Stoke-Einstein equation (Richardson, 2008), shown in Equation 4.14. The particle size is expressed by the radius a (m) of a rigid spherical particle and the speed of the particle, as the diffusion coefficient of the particles D ($m^2 \cdot s^{-1}$).

$$a = \frac{k\,T}{6\pi\,\eta\,D} \tag{4.14}$$

in which k is the Boltzmann constant ($J{\cdot}K^{-1}$), T is the temperature (K) and η is the viscosity of the solvent (Pa·s).

4.2 Materials and Methods

4.2.1 Laser Diffraction

The particle size distribution was obtained through laser diffraction method using the Nano Particle Size Analyzer (SALD7000H, Shimadzu, Japan). This analyzer detects particles in the range between 15 nm and 500 μm, using a 405 nm blue-violet laser as light source. The scattered light is detected by a wing sensor, located in the forward direction of the laser beam direction, and by lateral and back scattered light sensors. The measuring cell can be connected to the Aura-tec micro-bubble generator, which allows the measurement of the particle size distribution in line.

Thus, the particle size distribution during the generation of O_2 and air MNB were measured by this method. In the experiment with oxygen, the particle measurements were also done until 1 h after stopping the bubble production. The software WingSALD-7000 (Shimadzu), used to analyze the light scattering data, gives the particle size distribution in volume or in number of the particles. In this study, the particle size distribution was presented in number of particles.

4.2.2 Dynamic Light Scattering

The detection of particles by dynamic light scattering method was performed only after the generation of bubbles. Two equipments were used, with the same specifications (Zetasizer Nano ZS particle size analyzer, Sysmex Co., Japan), except for the laser wavelength of the light source: the red badge option (model ZEN3600) uses He-Ne laser as a light source, with 633 nm wavelength (red laser); while the green badge option (model ZEN3500) uses DPSS laser with 532 nm wavelength (green laser). The laser with smaller wavelength can provide better accuracy in the light intensity distribution pattern of very small particles.

These instruments detects particles in the range from 0.6 nm to 6 μm. The refractive index of the material of the "particles" was set to 1.0, corresponding to the air. The volume of the

sample was approximately 1 mL and the measurements were performed in a glass cell with square aperture, at controlled temperature of 20°C.

The DLS method is very sensitive to the movement of particles. Thus, it is also susceptible to minimum disturbances. In order to avoid the interpretation of noise signals as a particle detection, 5 to 10 replications of each sample was done. The analysis of the results were based on the average particle size distribution. The standard deviation, expressed by the error bars at each size interval of the distribution curves, indicate the repeatability of the measurements. A particle size distribution curve with a very high dispersion of values (high coefficient of variation) and low repeatability was interpreted as noise. In this case, the sample should contain particles in a level below the detection limit.

The red badge Zetasizer Nano ZS particle size analyzer was used in the preliminary experiments aiming to evaluate the quality of the water to be used as a control and to measure the particle size distribution of the O_2 MNB water after 2 hours of MNB production. The O_2 MNB water was produced in the Nikuni micro-bubble generator and stored in the 10 L tank of generator at a constant temperature of 20°C. The samples were taken periodically up to 2d after the bubble generation.

A more detailed examination on MNB water was performed using the green badge Zetasizer Nano ZS particle size analyzer. The bubbling time was fixed to 40 min and the measurements were done periodically until the particle detection started to fail. The flask containing each type of MNB water was stored at a 20°C constant temperature room, sealed with Parafilm (Pechiney Plastic Packaging, USA). O_2 and air MNB water produced in Aura-tec micro-bubble generator were analyzed. In addition, O_2 MNB water was produced at two different DO concentrations by the use of different nozzles in the outlet of the generator (single and two stage nozzles).

The original data of particle size distribution measured by the DLS method is given in intensity of scattered light. From the software used by the instrument (Dispersion Technology Software, version 5.03), the particle size distribution in intensity is converted to the volume distribution. This data, by its turn, can be calculated in number distribution. The number distribution, therefore, is more susceptible to errors than the other data due to the converting procedure. Although the particle size distribution in number is not so reliable, it was used in this study because it has more practical meaning. In addition, the intensity data is also important because they are more sensitive to the change in bubble stability. Therefore, both results were reported in this study.

4.2.3 Data Analysis

The data was analyzed through the geometric mean diameter of the particle size distribution. The geometric mean diameter and its standard deviation were calculated according to the standard ASAE S319.4 (ASABE, 2009), as described in Equation 4.15 and Equation 4.17, respectively:

$$d_g = log^{-1}\left[\frac{\sum_{i=1}^{n}(F_i\, log\, \overline{d_i})}{\sum_{i=1}^{n} F_i}\right] \tag{4.15}$$

$$S_{log} = \left[\frac{\sum_{i=1}^{n} F_i\, (log\, \overline{d_i} - log\, d_g)^2}{\sum_{i=1}^{n} F_i}\right]^{\frac{1}{2}} \tag{4.16}$$

$$S_g = \frac{1}{2}\, d_g[log^{-1} S_{log} - (log^{-1} S_{log})^{-1}] \tag{4.17}$$

where n is the number of intervals; F_i is the relative frequency of the i^{th} interval (%); $\overline{d_i}$ is calculated as $(d_i \times d_{i+1})^{1/2}$ (nm or μm), in which d_i is the lower size in a size interval and d_{i+1} is the upper size in a size interval of the histogram; d_g is the geometric mean diameter (nm or μm); S_{log} is the geometric standard deviation of log-normal distribution in ten-based logarithm and S_g is the geometric standard deviation of particle diameter (nm or μm).

The coefficient of variation (CV), here expressed in percentage, measures the dispersion of the particle size distribution:

$$CV = \frac{S_g}{d_g} \times 100 \tag{4.18}$$

4.3 Results and Discussion

4.3.1 Particle Size Distribution obtained by Laser Diffraction

4.3.1.1 Oxygen MNB Water

During the production of O_2 MNB, particles were detected in the micro range size. The particle size distribution correspondent to the bubbling generation period are shown by the dark and light blue curves in Figure 4.2, which refers respectively to the measurement at 5 and 30 min after the bubbling started. The geometric mean of the particles diameter was 69 μm at 5 min after starting bubbling and slightly decreased to 67 μm, 60 μm and 56 μm after 10, 20 and 30 min of

bubbling, respectively. The dispersion of the particle size distributions were between 26.8% and 30.5%. The complete data of geometric mean, geometric standard deviation and coefficient of variation obtained for O_2 MNB water during the bubble generation are presented in Table A1.1 in the Appendix 1.

A possible reason of the decreasing of the particle size with time could be the increasing DO concentration of water. At a higher DO concentration, the stability of a micro-bubble in the water increases, as the oxygen concentration gradient between the bubble surface and the bulk liquid is smaller. Therefore, small bubbles, which had a very high shrinking rate at low DO concentration, can be more stable and are easily detected by the laser diffraction as DO concentration increases. However, as discussed in Section 3.4, the DO concentration increases very quickly with the generation of O_2 MNB: in the measurement at 5 min after the bubbling started, the DO concentration already reached the maximum value and was practically stable during the whole bubbling period. The explanation for the decrease of particle size during a longer period than the DO increase could be that the bubble size distribution changes gradually, as smaller micro-bubbles increase in number with the continuous bubble generation.

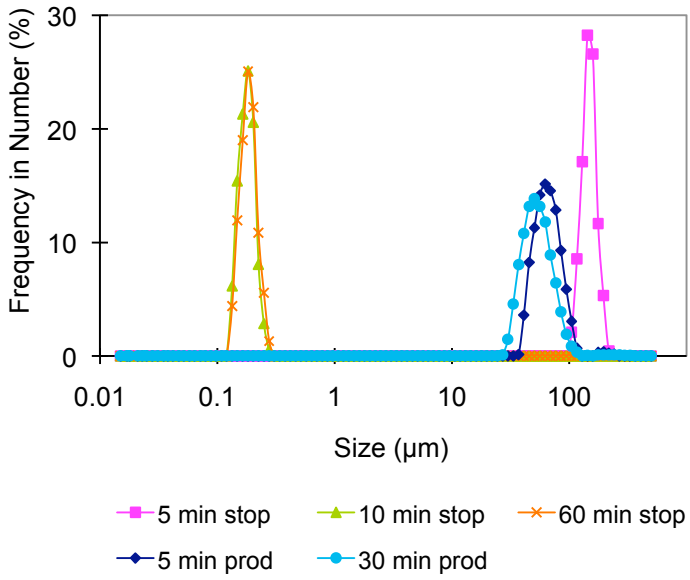

Figure 4.2: Particle size distribution of O_2 MNB water during (labeled "prod") and after (labeled "stop") the bubble generation. Frequency expressed in number of particles.

After the bubble generation stopped, the particles were detected at size in the range from 151 to 164 μm (geometric mean) during the first 8 min. The particle size distribution measured in this

period is represented by the distribution curve obtained at 5 min after the bubble generation stop (pink line), shown in Figure 4.2. In the following measurements, from 9 to 60 min, the micro-particles were no longer observed, but particles in the nano-scale were detected. The geometric mean of the particles diameter was in the range between 184 and 219 nm. Figure 4.2 shows the particle size distribution in this range, represented by the green and orange curves, which are correspondent to the measurement at 10 and 60 min after stopping the bubble generation. The coefficient of variation was between 12.0% and 20.4%, which shows that the dispersion of bubble size was smaller than during the production. The complete data obtained correspondent to the O_2 MNB water after the bubble generation are shwon in the Table A1.2 of the Appendix 1.

Based on the results obtained by laser diffraction method, it is possible to say that during the bubble generation, mostly micro-bubbles were detected. However, this result does not mean that there were no nano-bubbles in the water. As the concentration of micro-bubbles is much higher than nano-bubbles, the laser beam should reach mostly the micro-bubbles. Besides, the results are given in relative frequency, which means that, even if some nano-particles are detected, they are in a much lower proportion compared to the micro-particles and do not appear in the particle size distribution.

In the first minutes after the bubbling ceased, bigger micro-bubbles were detected. Although the results indicated the presence of only micro-bubbles, the visual observation of the water after stopping the bubble generation (Section 3.2) showed that the water was under unstable condition, with many bubbles floating to the water surface and some disappearing in the water, until it became transparent. Therefore, the result obtained through laser diffraction in the first minutes after stopping the bubble generation should represent a transition period, with bubbles in an unstable condition, shrinking or growing in size. However, only the big particles were detected by the laser diffraction method, for the same reason as described in the case of the particle detection during the bubble generation.

After the transition period until the first hour of observation, with the absence of micro-bubbles, particles in nano-size range were detected. However, there is a doubt if these particles are nano-bubbles or other nano-particles present in the water. A more detailed investigation about the existence of nano-bubbles after the generation of MNB was done using the dynamic light scattering method, and the discussion about the stability of nano-bubbles is presented in the Section 4.3.4.

4.3.1.2 Air MNB Water

In the operation of the micro-bubble generatior for the production of air MNB, micro-particles were detected practically stable at a geometric mean diameter of approximately 47 μm along the observation period. Differently from the oxygen micro-bubbles, the air micro-bubbles mean diameter did not seem to decrease in size with time. The reason for that is the time to the air bubbles reach a dynamic equilibrium is shorter than in the case of oxygen. Since air is composed mostly by 78% of nitrogen and 21% of oxygen, and nitrogen has a lower solubility in water than oxygen, the overall dissolution of air is lower than the oxygen. In this way, the difference in the dissolved gas concentration in the control water and after the air bubbling is smaller than in the oxygen bubbling. Therefore, the dynamic equilibrium of the air bubble size is reached in a shorter time than that of the oxygen bubble.

Regarding the size of the air micro-bubbles, the smaller diameter compared to the oxygen bubbles could be explained by the bubble nucleation process. Haedelt et al. (2007), comparing the bubble size of different gases included in chocolate, reported larger bubble diameters when gases with higher solubility were included. The authors justify that gases with higher solubility forms a greater amount of bubble nuclei, which increases the coalescence and originates larger bubbles when the pressure is released. This same mechanism could take place in the case of the generation of bubbles in water. As the dissolution of air in water is lower than that of oxygen, the number density of oxygen nuclei should be lower, leading to less frequent coalescence of bubbles when the pressure drops, resulting in smaller air bubbles.

The complete data obtained correspondent to the air MNB water during the bubble generation are presented in the Table A1.3 in the Appendix 1.

In the literature, there are reports of the use of the laser diffraction method to measure air bubbles in water. The mean diameter of air bubble in water obtained by Couto et al. (2009) was in the range of 32 to 40 μm (frequency based in the volume of the particles), while Li and Tsuge (2006b) obtained air bubble diameters from 52 μm to 67 μm (frequency in number), depending on the configuration of the bubble generator. These values are similar to the diameters obtained in this study. The variation of the bubble size is probably due to the bubble generation method and the quality of the water used to produce the bubbles.

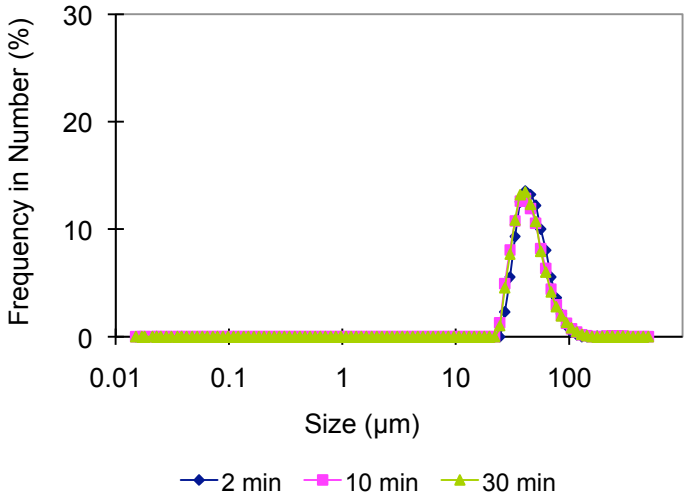

Figure 4.3: Particle size distribution of air MNB water during the bubble generation. Frequency expressed in number of particles.

4.3.2 Particle Size Distribution obtained by DLS (red laser)

A preliminary data was obtained through the DLS method which uses a 633 nm laser (red) as a light source. These first experiments had the objective to know the procedure to measure the MNB water sample in order to have a reliable result.

The complete data of particle size distribution curves, the geometric mean, the geometric standard deviation and the coefficient of variation calculated for each sample are shown in the Appendix 2.

Since the dispersion of bubbles is more unstable than a dispersion of solid particles and the particle sizes are very small, any disturbance should be avoided. Therefore, the first investigation was focused on the quality of the water used to produce the MNB. Particle size distribution of distilled water, ion-exchanged water and ultrapure water produced in a water purification system (described in Section 2.2.1) were tested. The aim was to select a water treatment in which no particle was detected, or at least, that the particle size distribution did not interfere in the detection of particles after the production of bubbles.

The dynamic light scattering method is very sensible to the movement of particles, thus a minimum disturbance in the analysis may result in a signal detected by the instrument. Therefore, even a sample at a very low concentration of particles would result in some detectable signal in the intensity particle size distribution. When the distribution curve is highly dispersed, without

repeatability, the signal is interpreted as noise. It is this pattern of particle size distribution that is aimed for a control sample, with no peaks which would interfere in the detection of particles in the MNB water.

However, the particle size distribution of distilled water showed a peak in the range of 500 nm when the frequency was expressed in intensity (Figure 4.4) and about 200 nm in number of particles. The presence of particles in this range of hundreds of nanometers would probably interfere in the detection of bubbles. Therefore, it was necessary to find a procedure to remove these particles.

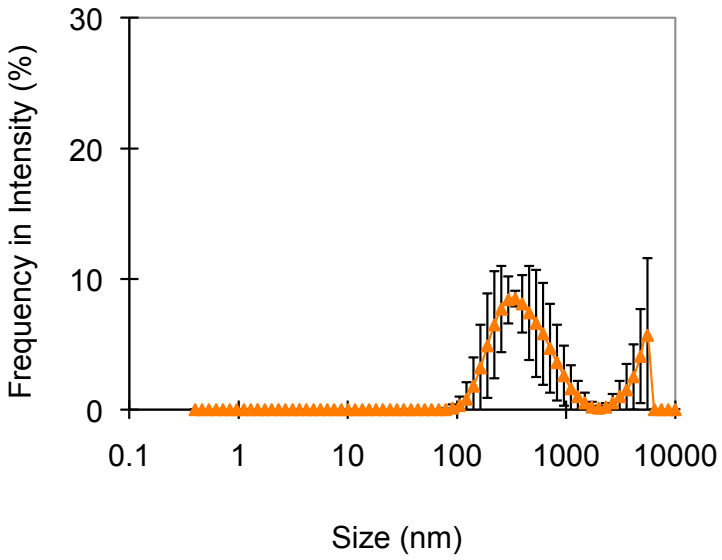

Figure 4.4: Average particle size distribution ($n = 5$), in intensity of scattered light of distilled water ($d_g = 519$ nm, $S_g = 638$ nm, $CV = 122.8\%$).

The first attempt was to remove the particles detected in the distilled water during the sampling in the DLS measurement cell. Disposable syringe hydrophilic filter units of 0.45 μm (mixed celulose ester, Dismic-25AS, Toyo Roshi Kaisha, Ltd., Japan) and 0.20 μm diameter pore (low protein binding LCR (PTFE) membrane, Millex-LG, Millipore Co., USA) were attached on the outlet of the syringe used to sample the water. In the case of the use of 0.45 μm filter, the particle size distribution expressed in number showed two peaks, one around 10 nm and another at 80 nm, but the size distribution in intensity still showed a geometric mean of about 500 nm. The 0.20 μm filter showed better results, as the peaks were detected at smaller sizes (0.6 nm and 60 nm in number), and the size distribution in intensity presented a high dispersion of size, verified by the

high coefficient of variation (521.5%), showing a very low level of particles.

The filters could remove some particles, but the results were still not satisfactory. A filter with a smaller pore diameter could be used to retain the smaller particles. However, the filtering procedure should also be done in the sampling of MNB water as well, in order to retain the same particles of the distilled water. Therefore, the smaller the filter pore size, the more disturbance would occur with the bubbles in the MNB water. Besides, the existence of particles in the distilled water could affect the formation and stability of the bubbles. A more adequate solution would be to use a water with higher purity level to generate the bubbles. Two treatments were tested: ion exchange and a water purification system composed by reverse osmosis, ion exchange and activated carbon unities (ultrapure water).

The particle size distribution in intensity of water treated with the ion exchange process is shown in Figure 4.5. The dispersion of the values is very high indicated a very low level of particles. The curve distribution in number had small peaks at approximately 10 and 80 nm, and a big peak at 0.6 nm. The result is similar to the filtered water during the sampling. Since in the ion exchange process some ions are removed, the bigger particles found in the distilled water with no treatment could be some clusters formed in the presence of those ions.

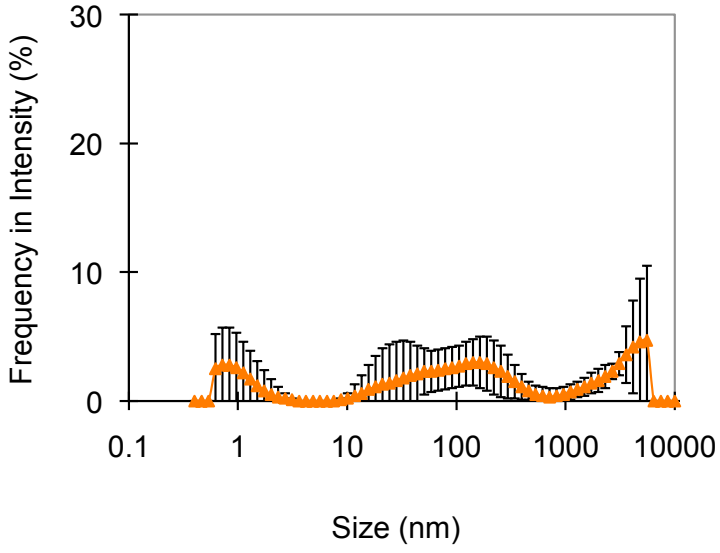

Figure 4.5: Average particle size distribution ($n = 5$), in intensity of water treated with ion exchange process ($d_g = 114$ nm, $S_g = 954$ nm, $CV = 838.4\%$).

Figure 4.6 shows the particle size distribution in intensity of the ultrapure water. Similarly as

the result obtained in the ion exchange treated water, there is a high dispersion of the particle size. In the distribution in number, however, the peaks were at very low sizes: approximately 0.6 and 15 nm. The nano-bubbles are not expected to have such a low diameter because of the molecular size limitation. Thus, the particle size distribution of the ultrapure water should be appropriate to be used to produce the bubbles for the particle size distribution measurements.

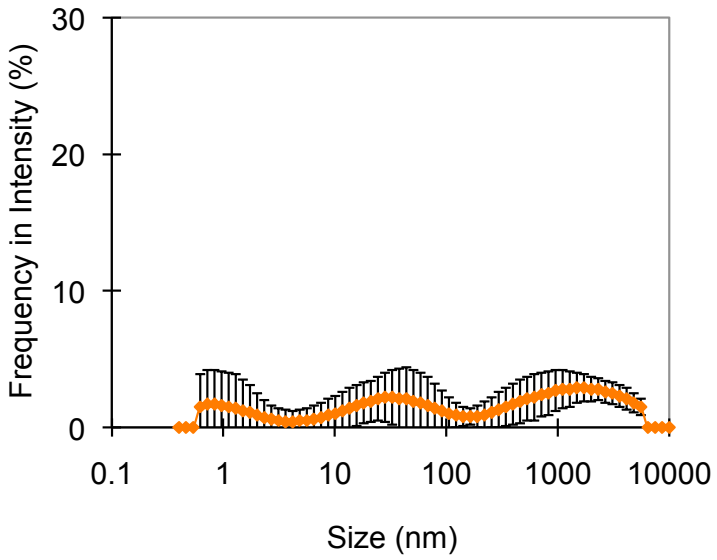

Figure 4.6: Average particle size distribution ($n = 10$), in intensity of scattered light of ultrapure water without degassing ($DO = 8.8$ mg·L^{-1}), ($d_g = 115$ nm, $S_g = 836$ nm, $CV = 726.8\%$).

The next measurements were performed as a preliminary test of the detection of nano-bubbles with time. The measurements were done 20 min, 5 h, 1 and 2 d after the bubble generation stop.

Figure 4.7 shows the particle size distribution in intensity of the O_2 MNB water 20 min after the bubbling stop. A log-normal mono-modal curve was observed. The geometric mean of this distribution was 240 nm and the coefficient of variation was 53.0%. In the next measurements, the geometric mean and the coefficient of variation fluctuated in similar ranges as the first measurement: between 228 to 261 nm and 43.9% (geometric mean) to 52.4% (coefficient of variation). In number, the particle size distribution presented a geometric mean of 139 nm on the first measurement and slight increased to 178 nm after 2 d. The coefficient of variation fluctuated in the range from 43.2% to 51.9%.

These results show that the particle size distribution was practically stable during the observation period of 2 d. Some particles in the range of a few hundred of nanometers (around 100 to 300

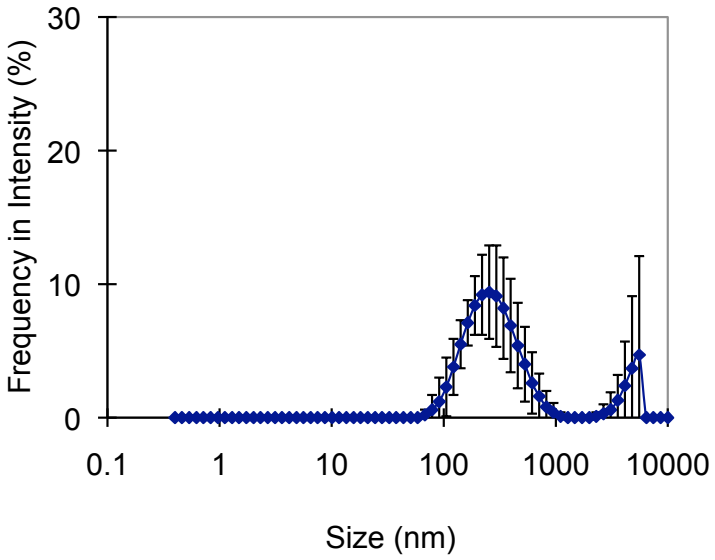

Figure 4.7: Average particle size distribution ($n = 5$), in intensity of scattered light of O_2 MNB water 20 min after stopping the bubble generation ($DO = 37.9$ mg·L^{-1}), ($d_g = 240$ nm, $S_g = 128$ nm, $CV = 53.0\%$).

nm) were detected in all samples after the generation of bubbles, in contrast to the high disperse particle size distribution in intensity and the peaks at sizes lower than 15 nm of the ultrapure water.

In addition, the DO concentration of the O_2 MNB water was 37.9 mg·L^{-1} on the first measurement and was kept at a high level (33.8 mg·L^{-1}) until 2 d later because of the high water volume (10 L) and the acrylic lid placed on the top of the tank. The high DO concentration of the O_2 MNB water could be related to the stability of the bubbles in the water.

In the following section, a more detailed investigation on the residence time and the probable stability of nano-bubbles are presented and discussed.

4.3.3 Particle Size Distribution obtained by DLS (green laser)

The particle size distribution measurements performed through the DLS method with a 532 nm laser (green) as a light source aimed to examine the residence time of the particles in nano-scale in the MNB water. Using different initial DO concentrations and different composition of gases (oxygen and air), the stability of nano-bubbles was investigated.

The complete data of particle size distribution curves, the geometric mean, the geometric standard deviation and the coefficient of variation calculated for each sample are shown from Figure A3.1 to Figure A3.38 in the Appendix 3.

4.3.3.1 Control Water

Although the ultrapure water normally showed very low level of particles, there were cases in which a peak at a relative large size was detected, as shown in the Figure 4.8. In the particle size distribution in intensity, the geometric mean was 612 nm with a coefficient of variation of 130.8%. In number, the values of geometric mean and coefficient of variation was 56 nm and 84.4%, respectively.

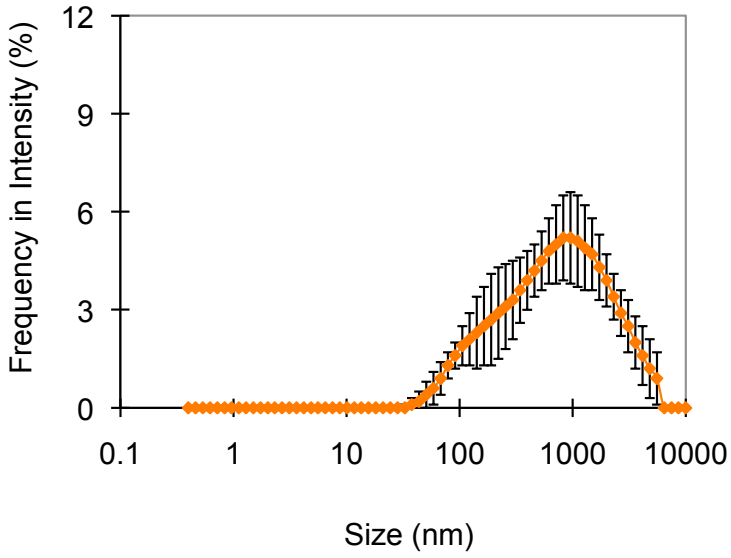

Figure 4.8: Average Particle size distribution ($n = 10$), in intensity of scattered light of ultrapure water before degassing ($DO = 10.1$ mg·L^{-1}), ($d_g = 612$ nm, $S_g = 800$ nm, $CV = 130.8\%$).

The detected particles were supposed to be a very few amount of air bubbles which were incorporated when the water was poured into the flask. The reason for that can be explained by the fact that the water purification system which was used for the preparation of ultrapure water can reject more than 99% of the particles, microorganisms and organic matter. Besides, no surfactants neither salts were added. Therefore, the water was expected to contain no solid particles.

After degassing the ultrapure water under vacuum for 20 min, the particle size distribution in intensity had a very high dispersion (coefficient of variation 794.5%) throughout all the diameter range. The distribution in number presented some small peaks at sizes lower than 30 nm, with a geometric mean of only 1 nm. Based on these results, it was concluded that the degassing procedure was efficient to eliminate some possible bubbles which were initially incorporated in the sample.

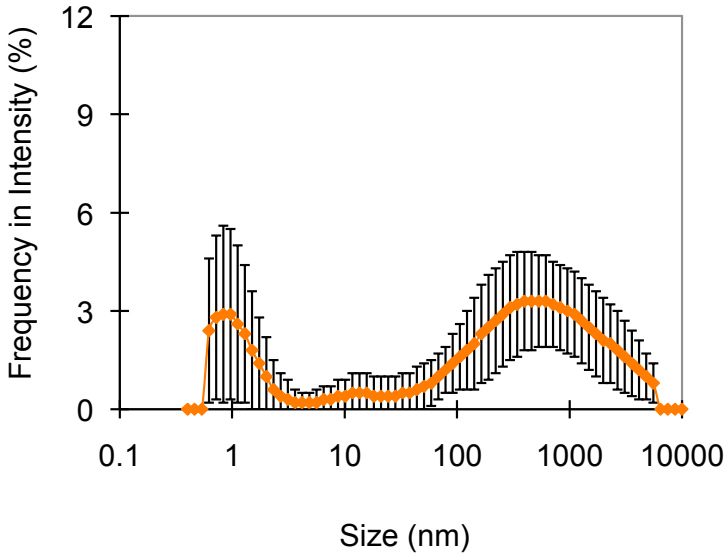

Figure 4.9: Average Particle size distribution ($n = 10$), in intensity of scattered light of ultrapure water after degassing, ($DO = 7.6$ mg·L^{-1}), ($d_g = 106$ nm, $S_g = 839$ nm, $CV = 794.5\%$).

Thus, the ultrapure water prepared by the water purification system and subsequently degassed with vacuum for 20 min was considered suitable as control water for the production of MNB water.

4.3.3.2 Oxygen MNB Water

Differently from the results obtained for the control water, the particle size distribution in intensity of the O_2 MNB water showed a regular shape of a mono-modal log-normal curve and the measurements had good repeatability (Figure 4.10), similarly as observed in the preliminary data (Section 4.3.2). Based on this difference, there is a high possibility that the particles detected represent the diameter distribution of nano-bubbles formed by the introduction of gas.

The geometric mean of the particle size distribution in intensity was 137 nm just after stopping the generation of bubbles. This geometric mean oscillated on the next hours until the following day, reaching values up to 272 nm. The coefficient of variation was in the range of 61.2 % to 85.0%. After 3 d of observation, the particles detected were bigger (380 nm) and the dispersion of particle size was higher (107.4%). Finally, on the sixth day after the bubble generation, the intensity particle size distribution curves were no longer mono-modal, the shape became irregular and there was no repeatability of the data (Figure 4.11). The geometric mean at this time was 432 nm and the coefficient of variation was 181.2%. The high dispersion and lack of repeatability in

intensity distribution curve could be understood as an insufficient concentration of particles to be detected by the instrument.

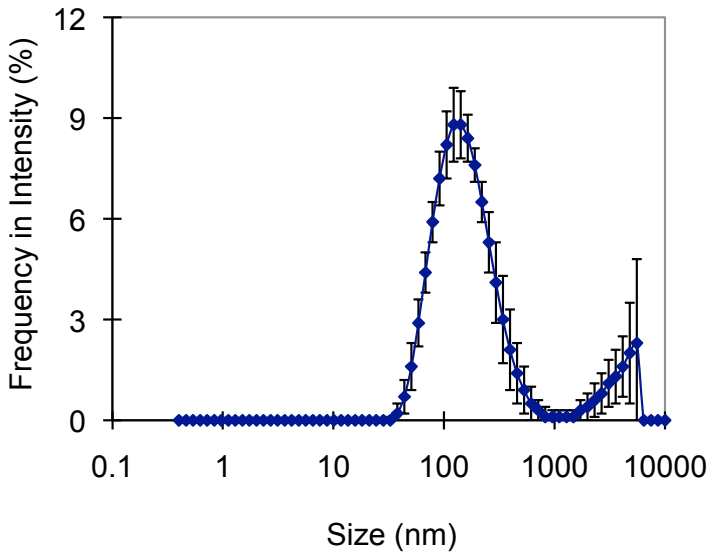

Figure 4.10: Average Particle size distribution ($n = 10$), in intensity of scattered light of O_2 MNB water just after stopping the gas introduction ($DO = 36.9$ mg·L^{-1}), ($d_g = 137$ nm, $S_g = 84$ nm, $CV = 61.2\%$).

On the other hand, the particle size distribution in number showed a different tendency. The initial geometric mean, 54 nm, did not oscillate much with time. The maximum value was observed after 3 d (70 nm), but on the sixth day, this value went down to 55 nm. The coefficient of variation did not show a big change in the dispersion of the particle size, ranging from 37.0% to 61.9%. On the sixth day, this value was 39.5%, in a contrast to the result obtained by intensity.

Although the particle size distribution in number is not so reliable as the data in intensity, the detection of particles until the sixth day of observation based on the number data indicates that particles are still present in the water. The DLS method does not quantify the number of particles, but from the intensity data, the low signal of particle detection could be interpreted as the lowering in the particle concentration. Thus, from both data of intensity and number, it can be concluded that there are particles in nanometrical size in the water after the bubble generation, and the number density of these bubbles decrease with time. On the sixth day of observation, the number density reached a level that these particles could not be detected reliably by the instrument (Ushikubo et al., 2009).

In addition, the change in the particle size distribution curves with time was in accordance with

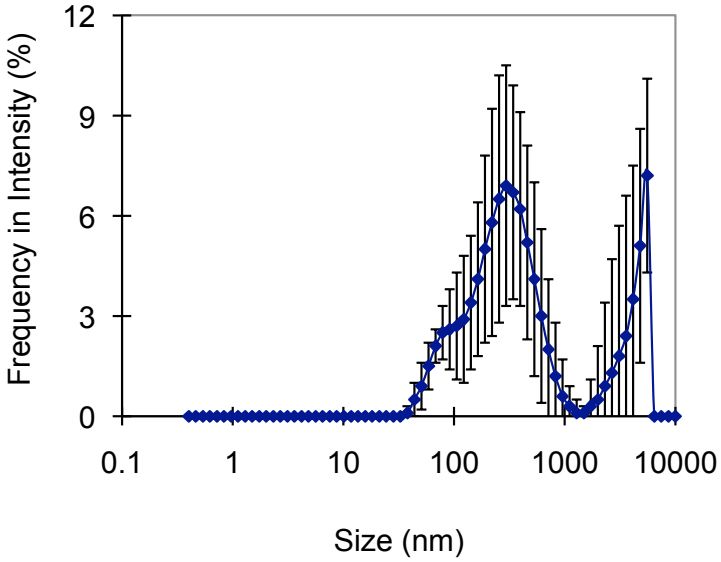

Figure 4.11: Average Particle size distribution ($n = 10$), in intensity of scattered light of O_2 MNB water 6 d later ($DO = 8.9$ mg·L^{-1}), ($d_g = 432$ nm, $S_g = 783$ nm, $CV = 181.2\%$).

the change in the DO concentration, which was at supersaturated level just after the bubble generation (36.9 mg·L^{-1}) and at saturation level after 6 d (8.9 mg·L^{-1}). The supersaturated condition could have kept the nano-bubbles concentration at a detectable level for a longer time. At high DO concentration, the concentration gradient between the bubble interface and the bulk liquid is smaller, which slow down the mass transfer of the oxygen from the bubble to the liquid. With time, the oxygen in the bubble dissolved into the water and, finally, diffused to the atmosphere. Thus, the bubble concentration decreased while the DO concentration reached the saturation level.

By the use of a two-stage nozzle, which has higher capacity of dispersing the gas into the water, O_2 MNB water at higher DO concentration (44.5 mg·L^{-1}) was produced. As a result, particles were observed for a longer time. Mono-modal lognormal curves were obtained in the intensity particle size distribution until the fifteenth day after the MNB water production. During this period, the bubble size remained practically constant. The geometric mean of the particle size distribution in intensity ranged from 125 to 172 nm and the coefficient of variation, from 55.4% to 72.6%. However, in the last measurement, performed on the eighteenth day, non-uniform and highly dispersed curves were observed in the intensity particle size distribution.

Regarding the number particle size distribution, the geometric mean was between 33 to 65 nm and the coefficient of variation was from 37.1% to 80.6%. Similarly in the previous experiment, the particles were detected at a reasonable stable range until the last observation day and the

dispersion of the size distribution did not increase too much. The discussion is the same as the previous case, in which the particles should be still present in the water, but the number density should be decreasing with time.

The DO concentration of the O_2 MNB water decreased from 44.5 mg·L^{-1} on the first day to 9.1 mg·L^{-1} on the eighteenth day, which shows that the saturation condition was reached. Based on the data obtained, it was observed that the higher initial DO concentration could extend the particle stability, which supports the relation between the DO concentration and the presence of nano-bubbles.

Another discussion point is that the particle sizes detected in the O_2 MNB water in the preliminary tests (Section 4.3.2) were larger in number and intensity than those detected in the samples described in this section. The main reason should be the micro-bubble generator used to produce the MNB water. In the former case, Nikuni micro-bubble generator was used, while in the latter case, MNB water was produced by Aura-tec micro-bubble generator. Differently from Nikuni generator, Aura-tec one is equipped by a nozzle in the outlet. The nozzle can have a better control in the bubble size, generating smaller bubbles.

In the reports in the literature, Najafi et al. (2007) measured air nano-bubbles in water using DLS method, obtained an average size of 290 nm. In addition, Kikuchi et al. (2009) reported the presence of oxygen nano-bubbles after water electrolysis by measuring particle size by DLS. The mean particle size was 30 nm on the first day and increased to 180 nm and to 250 nm on the second and third day, respectively. After this time, the bubbles shrank until the fifth day, when no particles were observed. The range of size and the duration of the bubbles were in agreement with the results obtained in this present study, at the lower initial DO concentration condition (36.9 mg·L^{-1}). These reports in literature and the measurements done in this present study show that the use of this method can be reliable for measuring bubbles at nano scale, although an indirect method such as DLS was originally used for measuring solid particles.

4.3.3.3 Air MNB Water

When air was introduced in water as MNB, the repeatability of data was not as good as that obtained for O_2 MNB water. Besides, the shapes of the distribution curves were irregular and the dispersion of the distribution was high ($>$100%) in all measurements. The geometric mean of the particle size distribution in intensity fluctuated from 350 nm on the first 5 min to 140 nm after 25

min of the bubble generation, with a coefficient of variation of 107.3% and 137.5%, repectively. Some particles could still be detected 45 min after the bubble generation, with geometric mean diameter of 205 nm and coefficient of variation of 120.7%. At 70 min, the distribution in intensity was very dispersed, with geometric mean diameter of 84 nm and coefficient of variation of 626.3%.

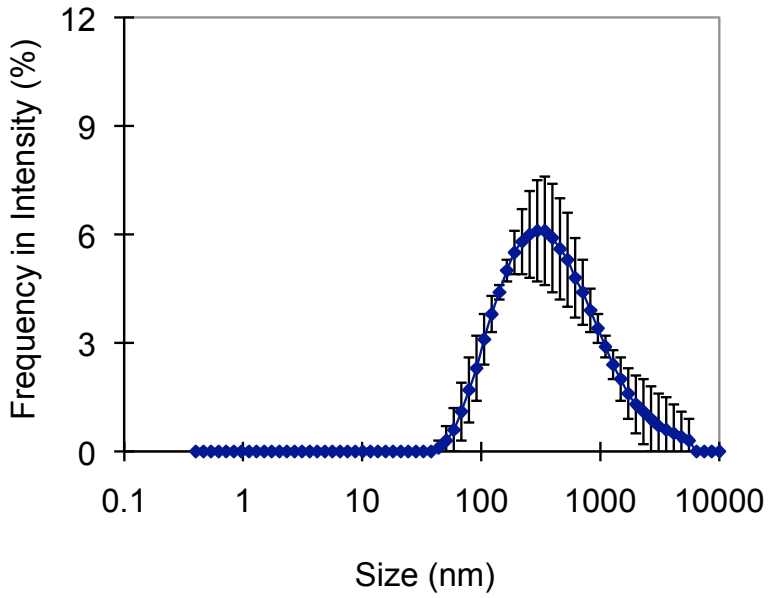

Figure 4.12: Average Particle size distribution ($n = 5$), in intensity of scattered light of air MNB water 5 min after stopping the bubble generation ($DO = 11.7$ mg·L^{-1}), ($d_g = 350$ nm, $S_g = 375$ nm, $CV = 107.3\%$).

Even in the number distribution, the data was not stable and the dispersion of the distribution was high. On the first measurement, the geometric mean diameter of the particle was 76 nm with coefficient of variation of 61.6%. At 25 min, two peaks were detected, at about 60 nm and other at 0.6 nm (coefficient of variation of 490.4%). At 45 min, peaks at approximately 90 nm, 25 nm and 0.7 nm were shown. The coefficient of variation was 392.0%. Finally, at 70 min, a only peak of 0.6 nm was detected. As 0.6 nm is the minimum detection limit and the peak was very sharp, it is suggested that no particles were found in this measurement.

Both data in number and intensity show the short stability of air MNB compared to the O_2 MNB. The low repeatability, the irregular and dispersed distribution curves of the air MNB water indicate that the concentration of bubbles was much lower than that observed in O_2 MNB water.

The DO concentration just after the air bubble generation was 11.7 mg·L^{-1} and kept practically stable until the last observation time (70 min). It is important to observe that this value of DO

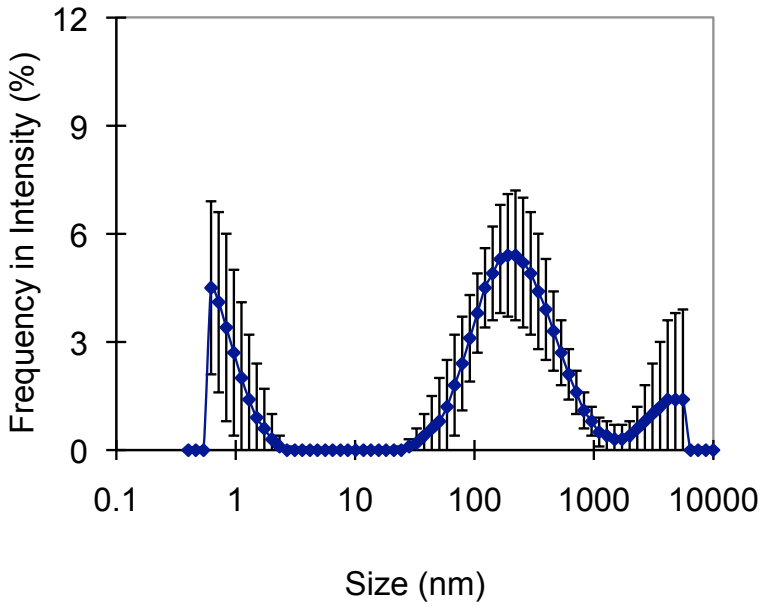

Figure 4.13: Average Particle size distribution (n = 5), in intensity of scattered light of air MNB water 70 min after stopping the bubble generation, ($d_g = 87$ nm, $S_g = 524$ nm, $CV = 626.3\%$).

concentration is much lower than that of the O_2 MNB water because air is composed just partially by oxygen (about 21%). In the air MNB water there should be some nitrogen dissolved in water, although in a lower concentration, as the solubility of nitrogen (1.274×10^{-5} mol gas/mol H_2O) is about a half than that of the oxygen (2.501×10^{-1} mol gas/mol H_2O, at 0.1 MPa, (Lide, 2003)).

Thus, the big difference between the periods in which particles could be observed stable in the O_2 MNB water (3 or 15 d) and in the air MNB water (less than 1 h) should be related to the lower dissolution of the air in water in relation to the dissolution of oxygen. At a lower concentration of dissolved gas in the water, the gas concentration gradient from the bubble interface to the bulk liquid is higher, which leads to the rapid dissolution of the bubble gas into the liquid and the consequent disappearance of the bubble.

4.3.4 Discussion on the Stability of Nano-bubbles

As discussed in Section 1.1.2, mathematical calculations show that a nano-bubble should not exist stable in normal conditions, as the high internal pressure, calculated by Young-Laplace equation (Equation 1.2), would lead to the total dissolution of the gas into the water.

On the other hand, the experimental data obtained in this study showed the detection of particles in the nanometrical scale with good repeatability of the results. Nano-particles were detected

in both laser diffraction and DLS methods after the generation of MNB in water. In addition, it was observed a time-dependent change in the detection of this particles in the DLS method. After some days (3 to 15 d), in the case of O_2 MNB, or less than 1 h, in the case of air MNB, the dispersion of the intensity distribution increased and the results had no repeatability. This shows that the number density of the nano-particles decreased with time until a undetectable level.

The results suggest that the nano-particles detected are nano-bubbles, which tend to decrease in number with time. The stability of the nano-bubbles is related to the dissolution of the gas in the water, which is lower in air than in oxygen. The gas supersaturation condition seems to support the stability of the nano-bubbles.

However, in the case of the O_2 MNB water produced at higher initial DO concentration with the two-stage nozzle, the extension of the particle detection time to 15 d was longer than expected. In Section 3.4, the saturation equilibrium time (defined to 10 $mg{\cdot}L^{-1}$) was reached in only 7 d under the same condition as this experiment (2 L water volume, high initial DO concentration). Thus, particles were still detected in the water after the saturation equilibrium. The possible reason for the longer observation time of particles is that the two-stage nozzle, used to produce water with higher initial DO concentration, can nucleate a greater number of bubbles than the single-stage nozzle because of the larger pressure drop. As a consequence, it takes more time to the number density of bubbles reach the minimum detector level of the particle size analyzer.

From these observations, it can be concluded that the high dissolution of oxygen in the water contributes to decrease the bubbles dissolution rate in the water, but it does not mean that the bubbles do not exist in saturated condition. The existence of particles even after the saturation equilibrium was also shown by the number distribution. Therefore, there should be other forces which can stabilize this particles besides the high gas concentration in the liquid.

The stabilization of the nano-bubbles could be explained by a charged interface, which creates repulsion forces. This was supported by the ζ-potential measurements in the Section 3.5, which showed that the MNB water is electrically charged. The magnitude of ζ-potential measured in O_2 MNB was greater than that of air MNB, which, by its turn, was higher than that of N_2 MNB. The higher ζ-potential of O_2 MNB supports the hypothesis of the stabilization of oxygen nano-bubbles for a longer time than air nano-bubbles, suggested by the particle size distribution. The stability of nitrogen nano-bubbles should be even lower than that of air nano-bubbles.

Bunkin et al. (2007, 2008) reported the existence and stability of “bubstons”, which are nano-

bubbles whose radius are between 10 and 100 nm, stabilized by ions in any saturated liquid. The authors justify the stability of the bubstons by the adsorption of ions on their surface, which makes repulsion forces compensate surface tension forces. The internal and external pressures are in equilibrium. In the later report, the authors concluded that 140 to 180 nm diameter air bubbles are gathered in micro-scale clusters in pure water.

The data of particle size distribution and ζ-potential obtained in this study agree with this description of the "bubstons" regarding the size and stability of the nano-bubbles by ions on their surface. In the case of pure water, the electrical charge should be originated from the polarization of the water molecules in OH^- and H^+ ions.

The relation between the negative ζ-potential and a different structure of water network at the bubble interface from that of the bulk water was reported by Takahashi (2005), as discussed in Section 3.5.

Moreover, the stability of nano-bubbles by strong hydrogen bonds on the interface was suggested by Ohgaki et al. (2010). The presence of hard hydrogen bonds, detected through infrared spectroscopy, would reduce the diffusion of gas to the bulk water. In this same report, the authors detected nitrogen, methane and argon nano-bubbles of 100 nm diameter by scanning electron microscopy. The bubbles could be stable as long as two weeks. The size, as well as the residence time of the bubbles, are similar to the results obtained in this study.

Finally, the experimental data obtained in this study give support to the existence of nano-bubbles. From different points of view, the results are in agreement with the data in the literature.

4.4 Conclusion

In this chapter, the particle size distribution of the MNB water was measured during and after the bubble generation. The results obtained by the laser diffraction method showed that micro-bubbles are present at a high number density during the bubble generation, with geometric mean diameters around 45 to 70 μm, analyzed by number of particles. Few minutes after stopping the bubble generation, the particle size distribution in number showed the presence of particles of about 200 nm diameter.

Preliminary data of particle size distribution using DLS method showed the importance of the quality of water in order to identify the particles formed after the bubble generation. Ultrapure

water produced by a water purification system was chosen as a control water since it showed a particle size distribution which would not interfere in the interpretation of the size distribution of the MNB water.

Further measurements using DLS method showed the presence of nano-particles in the water after the MNB generation. The diameter of the particles determined by the intensity distribution varied in the range between 100 to 300 nm, while the diameter obtained by the number distribution was between 30 to 70 nm.

In the case of the O_2 MNB water, the detection of the particles was practically stable until 3 or 15 d, depending on the initial DO concentration. The air MNB water, however, showed to be less stable, since the particles could be detected for less than 1 h. The time-depending detection of particles and the relation with the dissolved gas concentration suggested that the particles are nano-bubbles which can exist stable in water for some period of time.

Furthermore, the very long residence time of nano-bubbles in the case of the O_2 MNB water produced with the two-stage nozzle showed that the bubbles can still be detected after the saturation equilibrium was reached. This observation led to the conclusion that other forces are acting on the stability of nano-bubbles. The explanation for this stability is given by the ζ-potential measurements, presented in the Section 3.5, which shows that there are electrically charged particles after the bubble generation. The combination of the data of particle size distribution and ζ-potential strongly suggest the existence of nano-bubbles in water stabilized by an electrically charged interface, created by the polarization of molecules of the water in the gas-liquid interface.

Chapter 5

Proton Nuclear Magnetic Resonance

5.1 Introduction

The magnetic moment of a nuclei encompass the magnetism generated by the nuclei electric charges circulation and the intrinsic magnetism of the electrons and nuclei. The magnetic moment μ and the spin angular momentum S are directly proportional (Levitt, 2008):

$$\hat{\mu} = -\gamma \hat{S} \tag{5.1}$$

in which γ (rad·s^{-1}·T^{-1}) is the proportionality constant, which is has a particular value for each nucleus. The " ˆ " symbol indicates the quantum mechanical operators.

Both magnetic moment and spin angular momentum are vectors, which are in the same direction for $\gamma > 0$ and in opposite direction for $\gamma < 0$. When an external magnetic field B_0 (T, tesla) is applied, there is a change in the orientation of the direction of the spin angular momentum vector, which move around the magnetic field. The magnetic moment moves on a cone, keeping a constant angle between the spin magnetic moment and the field. The change in the orientation of the rotation axis is called precession.

The frequency of precession, referred to as Larmor frequency ν_L (Hz) is proportional to the magnetic field in the site of the particle:

$$\nu_L = \frac{\gamma B_0}{2\pi} \tag{5.2}$$

The nuclear magnetic resonance (NMR) studies the properties of molecules with a magnetic

nuclei by applying a magnetic field and observing the frequency of the resonant electromagnetic field (equal to Larmor frequency), (Atkins and de Paula, 2006).

The pulse techniques in NMR consist in the application of a stimulus in nuclear spins and monitor the radiation emitted as they return to the equilibrium. When a radio-frequency pulse is applied in a nuclei system, the magnetization occurs and, after the pulse, the nuclear spin magnetization tends to return to the initial equilibrium M_0. In the z-component, the magnetization M_z reverts to the equilibrium with a constant defined by the longitudinal relaxation time or spin-lattice relaxation time T_1 (s), expressed by:

$$M_z(t) = M_0\,(1 - e^{-t/T_1}) \tag{5.3}$$

The T_1 is a measure of how fast M_z grows back to M_0. However, it can not be confused as the time it takes to grow back to M_0. In theory, the time to recover 100% of the initial magnetization is infinite. However, it is normally considered that the time necessary to M_z recovers 99% of the M_0 value is $5T_1$, which is used in pulse sequences (Traficante, 1996).

After the pulse, the magnetization in the plane xy tends to zero. The decay is governed by a time constant, the transverse relaxation time or spin-spin relaxation time T_2 (s). The y (M_y) and x-component (M_x) of the magnetization are respectively defined by:

$$M_y(t) = -M_0\,cos(2\pi\,\nu_L\,t)\,(e^{-t/T_2}) \tag{5.4}$$

$$M_x(t) = M_0\,sin(2\pi\,\nu_L\,t)\,(e^{-t/T_2}) \tag{5.5}$$

Nuclear Magnetic Resonance (NMR) spectroscopy can detect weak molecular interactions such as hydrogen bonding, molecular mobility and steric effects (Balci, 2005). It is very common the application of this technique to study the state of water, as the water signal can be easily measured and distinguished from the signal of other components in a complex system. The relaxation properties can be related to the molecular properties of water, although this interpretation should be done very carefully because of the complexity of interactions (Berendsen, 1992).

The NMR signal of water can be characterized by three properties: resonance frequency, longitudinal relaxation behavior expressed by T_1 and transverse relaxation behavior through T_2. Ac-

cording to (Berendsen, 1992), former property is the least informative because the water molecules generate a single resonance and can not be distinguished as separated molecules. Thus, in this work, T_1 and T_2 will be measured in the samples of water before and after the bubble generation aiming to get information about the state of water.

5.2 Materials and Methods

Spin-lattice relaxation time (T_1) and spin-spin relaxation time (T_2) were measured in a pulsed spectrometer (JNM-MU25A, JEOL, Japan) at 25 MHz frequency and at constant temperature of 20°C. The pulse sequences used for T_1 and T_2 were saturation recovery and Carr-Purcell-Meiboom-Gill (CPMG), respectively. Five replications of each sample were collected in 10 mm diameter tightly closed tubes, up to a 1.5 cm high liquid column.

Three set of experiments were done to find out differences in molecular interactions with the introduction of MNB in water. The reasons are given in the Results Section (Section 5.3.1).

5.2.1 Oxygen MNB Water and Xenon MNB Water

In the first experiment set, distilled water was used as a control. Oxygen and xenon were generated as MNB in the distilled water, producing the "O_2 MNB water" and "Xe MNB water", respectively. In addition, "O_2 without MNB water", that is, water at high DO concentration but with no MNB included, was prepared. The preparation of this water consisted in subject distilled water placed in 30 mL beakers to high partial pressure of oxygen (0.5 MPa) in a high pressure chamber fig:chamber), at constant temperature of 20°C, overnight. The T_1 was measured at different DO concentrations.

5.2.2 Water at low DO Concentration

In the second set of experiments, the removal of oxygen from the water was tested by using two different approaches: using a two-channel vacuum degasser (DG660B-2, GL Sciences, Japan) and by purging a gas other than oxygen with a diffuser (Figure 5.2).

In the former test, the degassing machine was operated at 1 and 2 mL·min^{-1} flow rate. The water processed in the degasser was referred to as "degassed water". This water was collected in a 5 L plastic bag (HSB-5l, Hagy-tech Co. Ltd., Japan) without air inside. The plastic bag

Figure 5.1: High pressure chamber used to increase the dissolution of oxygen in water.

composition was polyethylene, nylon and a composite film, with total oxygen permeability of 54.7 $mL{\cdot}m^{-2}{\cdot}d^{-1}{\cdot}atm^{-1}$, at 23°C and 50% RH. After the degassed water volume reached 5 L, the DO concentration, T_1 and T_2 were measured.

The later test consisted in purging nitrogen and carbon dioxide gases to decrease the DO concentration in the water to a level lower than 1.0 $mg{\cdot}L^{-1}$. The water in which nitrogen was purged was called "N_2 without MNB water". This water was used as a control for the MNB waters produced with nitrogen (N_2 MNB water) and xenon (Xe MNB in N_2 water). The same procedure was performed using carbon dioxide. This gas was purged in water, producing the "CO_2 without MNB water". Using this water as a control for the "CO_2 MNB water", in which carbon dioxide was generated as MNB. T_1 and T_2 were measured for each sample.

5.2.3 Manganese Solution

The third experiment consisted in using manganese solution as control. Solutions of 3, 5, 10, 15, 40 mM of manganese (II) chloride tetrahydrate ($Mn_2Cl{\cdot}4H_2O$, Kanto Chemical Co. Inc., Japan) were prepared (control sample), then O_2 MNB was produced ("O_2 MNB solution"). A more detailed analysis was done at 10 mM manganese solution. At this concentration, oxygen was diffused through a gas diffuser until reach a DO concentration higher than 35 $mg{\cdot}L^{-1}$ ("O_2 without MNB solution"). In addition, different gases without paramagnetic properties were used.

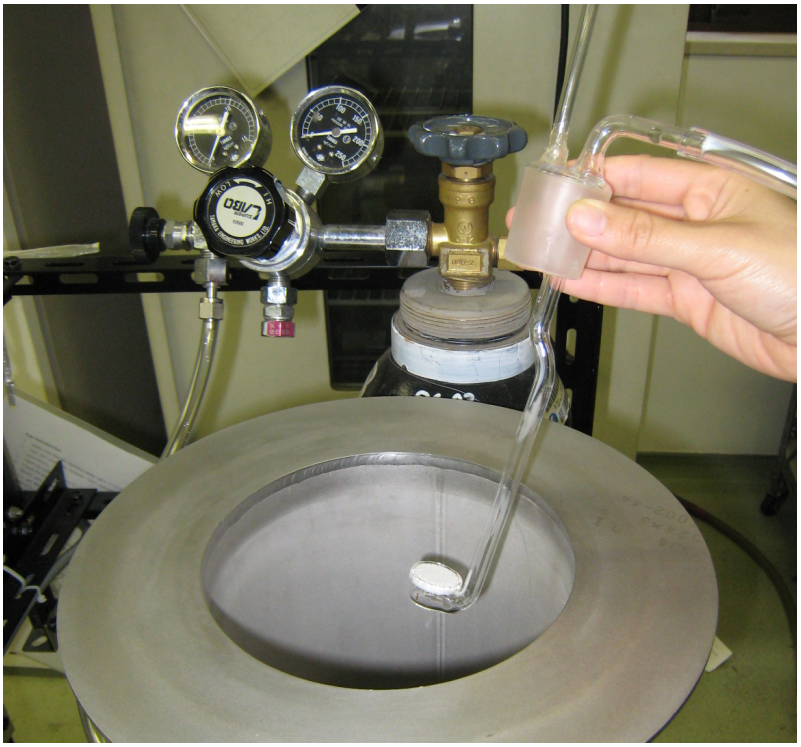

Figure 5.2: Gas diffuser used to purge gas into the water without the generation of MNB

Xenon introduced as MNB in the 10 mM manganese solution was called “Xe MNB solution”. Carbon dioxide was used to prepare two samples: “CO_2 MNB solution”, by the production of CO_2 as MNB in the manganese solution and “CO_2 without MNB solution”, by purging carbon dioxide in the 10 mM manganese solution. In this set of experiments, only T_1 was measured.

5.3 Results and Discussion

5.3.1 Oxygen MNB Water and Xenon MNB Water

The measurements of T_1 and T_2 in the distilled water showed respectively average values of 2.32 $\pm$ 0.05 s and 1.82 $\pm$ 0.08 s. The introduction of oxygen as MNB led to a decrease in both T_1 and T_2, to 1.7 $\pm$ 0.1 s and 1.28 $\pm$ 0.07 s, respectively. Regarding the DO concentration, it increased from 8.8 mg·L^{-1} in distilled water to 45.3 mg·L^{-1} in O_2 MNB water.

On the other hand, the introduction of xenon in water as MNB resulted in an elongation of both T_1, to 2.59 $\pm$ 0.08 s, and of T_2, to 1.94 $\pm$ 0.02 s in relation to the distilled water value. The DO concentration was very low with the introduction of Xe MNB into the water (2.0 mg·L^{-1}),

which shows that the introduction of xenon gas expelled the naturally dissolved oxygen from the distilled water. Figure 5.3 shows the comparison of T_1 for each sample.

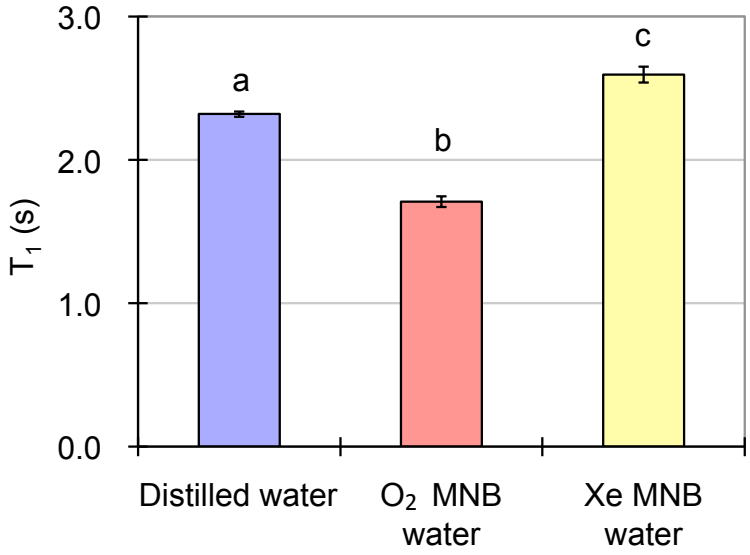

Figure 5.3: Average values of T_1 measured in distilled water (control, DO = 8.8 mg·L^{-1}), O_2 MNB water (DO = 45.3 mg·L^{-1}) and Xe MNB water (DO = 2.0 mg·L^{-1}). The vertical bars show the standard deviation of the measurements. Different letters means that the samples differ significantly ($p < 0.05$).

The opposite results observed in the T_1 and T_2 measurements of Xe and O_2 MNB water could indicate an effect of each type of gas introduced as MNB on the dynamic state of the water. However, since the DO concentration also varied in opposite sides, it was thought that the results were a consequence of the different concentration of oxygen in each sample (Ushikubo et al., 2007).

This hypothesis was confirmed by the T_1 and T_2 measurements of O_2 without MNB water. This water presented shorter T_1 and T_2 than the distilled water, that is, it showed similar tendency as the O_2 MNB water. The results can be better visualized in Figure 5.4, which shows the mean values of T_1 and T_2 of O_2 without MNB water, O_2 MNB water and Xe MNB water measured at different levels of DO concentration. From this figure, a clear inverse proportionality between T_1 and T_2 with DO concentration is observed, independently if the sample contained MNB and which type of gas was used. This indicates that the relaxation time measurements were influenced by the concentration of oxygen dissolved in water and not by some modification in the water dynamic properties caused by the micro- and nano-bubbles.

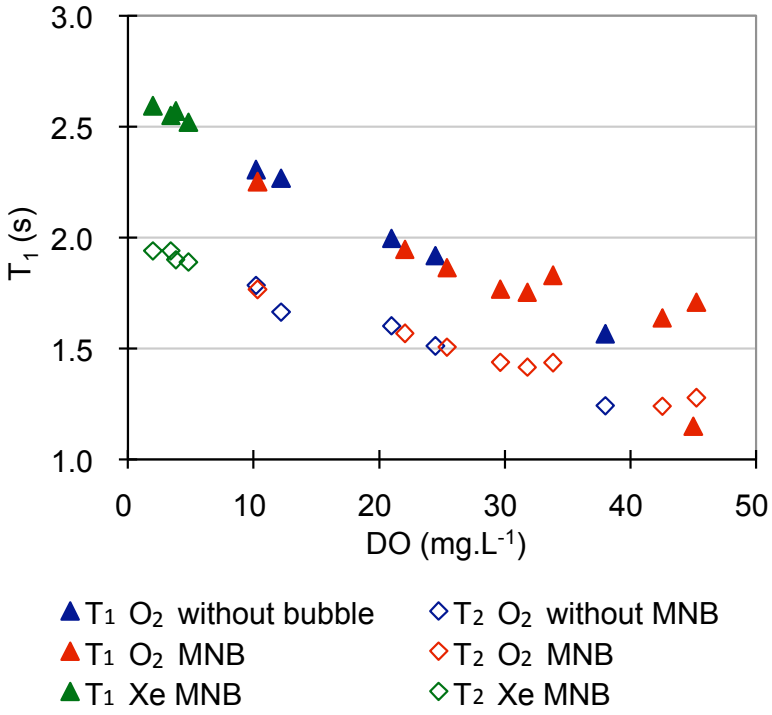

Figure 5.4: Variation of relaxation times T_1 and T_2 with DO concentration of O_2 without MNB water, O_2 MNB water and Xe MNB water

The influence of the DO concentration in the relaxation times is explained by the paramagnetic characteristic of oxygen. In a paramagnetic element, the magnetogyric ratio of the electron is about 657 times greater than that of a proton in observation (Abraham et al., 1988). Therefore, the interaction of the paramagnetic element which are in the same molecule that contains the nucleus in observation or in its surroundings will lead to a very efficient relaxation, that is, to a short T_1.

A useful parameter that show the paramagnetic characteristic of an element is the magnetic susceptibility. It shows how readily the material develops a magnetic moment by the application of an external magnetic field (Levitt, 2008). The molar magnetic susceptibility of (χ_m) some elements are shown in Table 5.1. As can be observed in this table, the magnetic susceptibility of oxygen is $+3449\times10^{-6}$ cm^3·mol^{-1}. The positive value mean that it is a paramagnetic element. On the other hand, the magnetic susceptibility of the water and other gases is a small negative value, which indicates that these other gases are diamagnetic. Therefore, oxygen, as a paramagnetic element, is an interferer in the T_1 measurements.

Still, it is important to consider that this result does not mean that there is no effect of the bubbles on the dynamic properties of water, but that the oxygen is an interferer in NMR analysis.

Table 5.1: Molar magnetic susceptibility (χ_m) of some elements at room temperature (285 to 300 K). Source: Lide (2003).

Name	Formula	χ_m (10^{-6} cm^3·mol^{-1})
Carbon dioxide (gas)	CO_2	-21.0
Manganese(II) chloride tetrahydrate	$Mn_2Cl{\cdot}4H_2O$	+14600
Nitrogen (gas)	N_2	-12.0
Oxygen (gas)	O_2	+3449
Water (liquid, 293 K)	H_2O	-12.96
Xenon (gas)	Xe	-45.5

In order to avoid de interference of oxygen in the measurements, two approaches were taken. One was to remove the oxygen from the water to use it as a control, and then produce MNB water with a gas other than oxygen (nitrogen). The other approach was to add manganese ions in the water before the generation of bubbles. The reason will be explained in the Section 5.3.3.

5.3.2 Water at low DO Concentration

In order to avoid the paramagnetism effect, it was tried to remove the oxygen from the water. The methods used to remove the oxygen was degassing with a two-chanel vacuum degasser machine and diffusing other gases than oxygen, without paramagnetic characteristics.

The degassing machine flow rate was set to 1 and 2 mL·min^{-1}. At a lower flow rate, a higher amount of oxygen could be removed. However, the time necessary to produce the same volume was longer, therefore, increasing the oxygen permeation time through the plastic bag. The time necessary to collect 5 L of degassed water at 1 mL·min^{-1} was 5000 min, that is, about 3 d and 11 h. Considering the oxygen permeability of the plastic bag as 54.7 mL·m^{-2}·d^{-1}·atm^{-1}, and the area of the bag as 0.152 m^2 (dimensions: 19 cm (wide)×14 cm (deep)×19 cm (high); the bottom surface was not considered), the volume of oxygen permeated through the plastic bag is 28.9 mL. On the other hand, the time to produce the same volume of degassed water at 2 mL·min^{-1} was the half of that time and, therefore, 14.4 mL of oxygen would permeate in this period.

However, the oxygen removal by this method was not satisfactory at neither flow rate. After 5 L of degassed water collected, the DO concentration of the water produced at 1 mL·min^{-1} flow rate was 6.2 mg·L^{-1}, while at 2 mL·min^{-1}, the DO concentration was 5.7 mg·L^{-1}. In order to make sure that no paramagnetic effect is affecting the relaxation times, it is necessary to reach a

very low DO concentration, such as lower than 1 mg·L^{-1}. One possible cause of the relative high DO concentration of the degassed water could be the long exposure time to the oxygen permeation, as a long time was taken to collect a large volume of water. However, a small amount (30 mL) of degassed water was collected at 1 mL·min^{-1}, yet the DO concentration was high: 5.1 mg·L^{-1}.

The T_1 and T_2 average values of the degassed water are presented in Table 5.2. There were no significant differences ($p < 0.05$) between the water collected at 1 and 2 mg·L^{-1}. This result was expected, since the DO concentration was similar. Comparing to the distilled water at the saturation equilibrium (Section 5.3.1), T_1 of both degassed water samples were longer than that of the distilled water, while no significant differences were observed in T_2 ($p < 0.05$). The longer T_1 indicates that the paramagnetic effect of oxygen was decreased. However, the T_1 of a oxygen-free water was measured at 20°C as 2.95 s by Simpson and Carr (1958) and around 3 s by Hindman et al. (1973). These T_1 values are much higher as obtained in this study. From the comparison of the data in literature, it is clear that some paramagnetic effect of oxygen is still affecting the degassed water produced in this study. For this reason, the degassed water was not used to produce MNB.

Table 5.2: T_1, T_2 and DO concentration of water with and without gas introduction. Different letters means that the samples differ significantly ($p < 0.05$).

Sample	T_1 (s)	T_2 (s)	DO (mg·L^{-1})
Degassed water 1 ml·min^{-1}	2.59 ± 0.03^{a}	1.84 ± 0.02^{A}	6.2
Degassed water 2 ml·min^{-1}	2.53 ± 0.04^{a}	1.86 ± 0.05^{A}	5.7
N_2 without MNB	2.75 ± 0.07^{b}	2.01 ± 0.08^{B}	0.5
N_2 MNB water	2.79 ± 0.02^{b}	2.03 ± 0.05^{B}	0.4
Xe MNB in N_2 water	2.75 ± 0.04^{b}	2.01 ± 0.04^{B}	0.4
CO_2 without MNB	2.55 ± 0.05^{a}	-	0.6
CO_2 MNB water	2.53 ± 0.03^{a}	-	0.4

On the other hand, the oxygen removal by purging other gases in the water resulted in a very low DO concentration. By the purge of nitrogen in the water, the DO concentration decreased to 0.4 mg·L^{-1}. In the case of carbon dioxide, the DO concentration was 0.6 mg·L^{-1}. At these DO concentrations, the paramagnetic effect of oxygen would be minimum, allowing to verify some molecular interaction changes with the introduction of MNB. However, one disadvantage of this method is that the introduction of other kind of gases itself might change the interactions of

molecules in the system. To overcome this problem, the MNB were generated from the same gases as those used to purge the oxygen (N_2 MNB and CO_2 MNB). One exception was the Xe MNB, which was produced in a water purged with nitrogen. The nitrogen is supposed not to interact with water, due to its low solubility and non-reactive characteristics.

The average values of T_1 and T_2 of the water purged with nitrogen (N_2 without MNB water) and carbon dioxide (CO_2 without MNB water), as well as of the N_2, Xe and CO_2 MNB water are shown in Table 5.2. The samples in which nitrogen was purged showed T_1 longer than 2.7 s and T_2 longer than 2.0 s. Relating these results to the low DO concentration, it can be observed that the paramagnetic effect was practically suppressed. However, the introduction of MNB neither in the case of nitrogen nor in xenon sample did not show significant change in T_1 and T_2 ($p < 0.05$). In the case of the water purged with carbon dioxide, the average T_1 was approximately 2.5 s. This value was significantly different from the nitrogen purged samples, probably because of the presence of ions H^+ and HCO_3^- formed by the dissociation of the carbon dioxide, which changed the molecular interaction. With the generation of CO_2 MNB, however, any significant change was observed in T_1.

It can be concluded from the results that the difference in molecular interactions due to the MNB generation could not be verified through this method. One possibility is that the change in the relaxation time is lower than the precision limit of the instrument. Thus, a different approach was taken in order to check the differences with the generation of MNB.

5.3.3 Manganese Solution

Based on the previous results, T_1 and T_2 seemed to show similar tendencies in the samples. In order to simplify the experiments, and considering that T_1 measurements are more reliable than T_2 (Berendsen, 1992), only T_1 was measured in this section.

The magnetic susceptibility of the manganese(II) chloride tetrahydrate ($Mn_2Cl{\cdot}4H_2O$) is much higher than that of oxygen, as shown in Table 5.1. Thus, the addition of manganese ions in the water before the generation of bubbles was expected to cause an excess of paramagnetism and mask the interference of oxygen in the NMR analysis.

As a result, as shown in Table 5.3, T_1 differed significantly ($p < 0.05$) between the samples before and after the gas introduction as micro- and nano-bubbles and was longer for all the concentrations tested (Ushikubo et al., 2009).

Table 5.3: T_1, DO concentration and pH of Mn^{2+} solution at different concentrations, before (control) and after introduction of O_2 MNB. Different letters means that T_1 of the control and the O_2 MNB solutions differ significantly ($p < 0.05$).

$[Mn^{2+}]$	Control			O_2 MNB solution		
(mM)	T_1 (ms)	DO (mg·L^{-1})	pH	T_1 (ms)	DO (mg·L^{-1})	pH
3	36.7±0.1^a	7.7	5.97	37.60±0.06^b	39.6	6.30
5	20.8±0.1^a	8.0	5.80	21.35±0.06^b	39.1	6.12
10	11.57±0.03^a	8.6	5.59	12.48±0.06^b	38.8	5.71
15	7.77±0.03^a	9.4	5.78	8.18±0.03^b	39.6	5.83
40	2.894±0.004^a	8.5	5.88	3.01±0.02^b	35.8	5.69

A more detailed investigation was performed at a 10 mM manganese solution, which was used to prepare the O_2 without MNB, Xe MNB solution, as well as CO_2 without MNB and CO_2 MNB solution. At 10 mM, the O_2 MNB solution presented a T_1 of 12.5 ± 0.1 ms, while the value in control (manganese ions solution) was 11.57 ± 0.07 ms. As shown in Figure 5.5, the change in T_1 value of MNB solutions did not seem to have influence from DO concentration, since the oxygen without MNB solution did not differ statistically from the control sample ($p < 0.05$) with a T_1 of 11.5 ± 0.2 ms, even containing high DO concentration (37.1 mg·L^{-1}). These results indicate that the paramagnetic effect of oxygen was successfully masked by the excess of manganese.

Similar tendency was observed in the experiments with carbon dioxide. In the sample containing CO_2 by simply purging this in water (CO_2 without MNB solution), T_1 average value was 11.5 ± 0.2 ms, which does not differ significantly from the T_1 of the manganese solution ($p < 0.05$). On the other hand, in the sample with the MNB included (CO_2 MNB solution), the average T_1 increased to 13.1 ± 0.2 ms.

Besides, with the Xe MNB generation in manganese solution, the average T_1 increased to 12.2 ± 0.1 ms, showing that the same tendency of T_1 elongation with the generation of MNB was observed, independently of the gas tested (oxygen, carbon dioxide and xenon).

In a previous study, Oshita et al. (1999) reported the shortening of T_1 when xenon gas was applied to distilled water under high pressure. The authors related the decrease in T_1 to the increase in the viscosity of water after it was subjected to the xenon gas, as these parameters are inversely proportional.

On the other hand, the opposite tendency was observed in Xe MNB solution in this present study, since T_1 increased with xenon gas introduction. The opposite result can be explained by

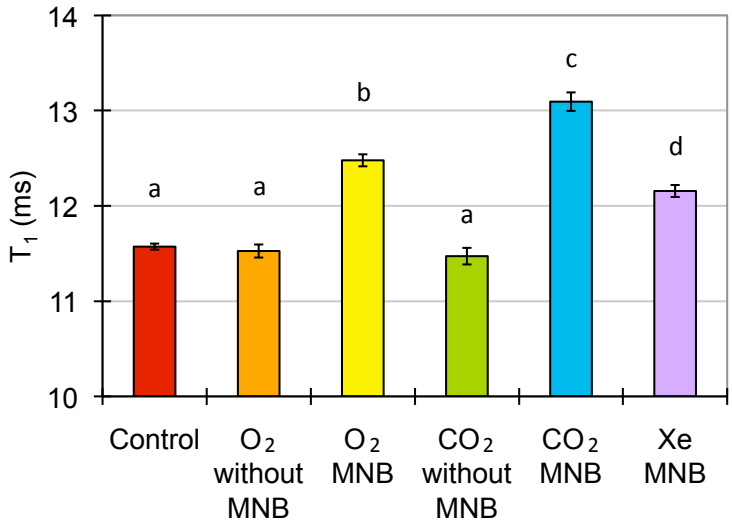

Figure 5.5: Mean T_1 values of 10 mM Mn^{2+} solutions: control (DO = 8.6 mg·L^{-1}) O_2 without MNB solution (DO = 37.1 mg·L^{-1}), O_2 MNB solution (DO = 38.8 mg·L^{-1}), CO_2 without MNB solution (DO = 0.6 mg·L^{-1}), CO_2 MNB solution (DO = 0.5 mg·L^{-1}) and Xe MNB solution (DO = 0.5 mg·L^{-1}). Different letters means that the samples differ significantly between each other ($p < 0.05$).

the difference of structures formed when xenon gas is applied under high pressure and as micro- and nano-bubbles. Oshita et al. (1999) found out that a "structured water" was formed with the application of xenon under high pressure. However, in this study, this structure was not detected by the Xe MNB generation.

The most probable reason for the relaxation time change could be the change in the apparent concentration of manganese ions. The paramagnetic effect occurs when the paramagnetic molecule (in this case, the manganese ions) are in direct contact with the nucleus in observation (the hydrogen protons of the water molecule). With the introduction of MNB, the manganese ions should be adsorbed to the bubbles surface, as the ζ-potential measurements showed that they are negatively electrically charged (Section 3.5). Thus, the apparent concentration of manganese ions decreases in the water. Since the manganese ions are concentrated near the bubbles, the contact area between the water molecules with the manganese ions is decreased. As a consequence, the paramagnetic effect caused by the manganese will also decrease, resulting in a longer T_1.

The importance of these findings is that, by the detection of the change in the apparent concentration of manganese is caused by the presence of an electrically charged interface, which support the existence of nano-bubbles, as observed through the particle size distribution measurements.

Furthermore, there could be other possibilities for the detection of change in T_1. The T_1 elongation observed in MNB solutions could indicate the modification of the water network. A longer relaxation time is related to a less bonded molecular structure. Thus, the generation of MNB in the water could result in a decrease in the hydrogen bonds between the water molecules. According to Himuro (2007a), during the shrinking process of a micro-bubble, hydrogen bonds get weaker and the surface tension decrease. With the generation of bubbles, the polarization of water molecules in OH^- and H^+ ions in the bubble surface may affect the hydrogen bonds between the water molecules. The tendency of elongating T_1 was observed more intense in the case of carbon dioxide. This would be justified by the formation of H^+ and HCO_3^- ions when dissolved in the water, which contributes for the weakening of hydrogen bonds by the formation of ion-dipole forces.

A different explanation could be the magnetic field radiation effect on the gas-liquid interface. Vallée et al. (2005) found that the presence of nano-bubbles seemed to influence water characteristics after the electromagnetic field exposure. Colic and Morse (1999) reported that the gas-water interface should be the main receptor of electromagnetic radiation. Based on this information, the magnetic field applied on the samples during the NMR measurements should modify the characteristics of the MNB solutions by the presence of nano-bubbles. As a result, a change in the response would be observed in relation to the water without bubbles.

From these three possible reasons to explain the change in T_1 in the MNB solution, the former one is the most acceptable, since the change in the relaxation time was observed only in the set of experiments using manganese ions solution, and the explanation is based on the change in the paramagnetic effect. In any case, however, the modification in the T_1 was explained by the presence of nano-bubbles.

5.4 Conclusion

The NMR relaxation times T_1 and T_2 were measured in O_2 MNB water and Xe MNB water. However, it was verified that the DO concentration can affect the results, caused by the paramagnetic properties of the oxygen. In order to overcome this problem, two approaches were taken: (1) remove the oxygen from the water to avoid the paramagnetic effect and (2) add manganese ions, which have a higher magnetic susceptibility than oxygen, aiming to promote an excess of

paramagnetism and mask the oxygen effect.

The first approach could not show differences in the relaxation times between the samples before and after the generation of MNB. On the other hand, the second approach showed a significant increase in the average T_1 with the production of MNB in solutions at different manganese ion concentrations, independently of the gas used to produce MNB.

The most probable reason for the elongation of T_1 with the MNB generation is that the manganese ions should adsorb on the negatively charged bubble surface, lowering the manganese ion apparent concentration. The decrease in the contact area between the paramagnetic elements with the water molecules would lead to a decrease of the paramagnetic effect in the sample, hence increasing T_1.

The difference found in T_1 of manganese solution with the generation of MNB supports the existence of nano-bubbles with a electrically charged surface, as suggested by the previous data obtained through the particle size distribution and the ζ-potential measurements.

Chapter 6

Final Remarks

6.1 Conclusion

During the generation of oxygen micro- and nano-bubbles in the water, the water showed a white milky appearance. The DO concentration rapidly increased to values of approximately 35 to 45 mg·L^{-1}, but no change in pH was observed. Micro-bubbles of geometric mean diameter of 56 to 69 μm, in the case of oxygen, and 47 μm, in the case of air, were detected through laser diffraction method. In observation through optical microscope, bigger bubbles of approximately 100 μm diameter were stable in the water drop, while bubbles smaller than 50 μm diameter shrink.

After stopping the bubble generation, the milky appearance of the water gradually disappeared, becoming transparent. The DO concentration decreased with time to reach the saturation equilibrium (defined as to reach 10 mg·L^{-1}) from 3 to 12 d, depending on the volume of water and on the initial DO concentration. The pH remained practically constant. The micro-bubbles were no longer detected after some minutes after stopping the bubble generation, but particles in the nano scale were detected. The laser diffraction method detected particles of approximately 200 nm diameter in number distribution, while dynamic light scattering method detected particles in the range of about 100 to 300 nm in intensity distribution and between 30 to 70 nm in number distribution. The residence time of the nano-particles was estimated by the measurements of particle size distribution along the time. The particles could be detected for 3 to 15 d in O_2 MNB water and for about 45 min in air MNB water. The time-dependent change of the detection of the nano-particles suggested that the particles are nano-bubbles stabilized for some days or hours. The gas super-saturation condition of the water could slow the diffusion of the bubble gas to the liquid, but

nano-bubbles were also detected at saturation condition.

The ζ-potential measurements in O_2 MNB water suggested the presence of negatively charged bubbles. The electrically charged bubble interface could explain the stabilization of nano-bubbles by repulsion forces. The magnitude of the ζ-potential measured in O_2 MNB water was in the order of -40 mV, while in air MNB water, was -30 mV. This difference in the magnitude should affect the stability of bubbles. This observation is in accordance to the difference in the residence time observed in the case of oxygen and air nano-bubbles.

Moreover, the change in T_1 of Mn^{2+} solution after the introduction of O_2 MNB suggested the adsorption of Mn^{2+} on a gas-liquid interface, supporting the existence of nano-bubbles in water.

In summary, with the use of different approaches (particle size distribution, ζ-potential and NMR relaxation time), the existence of nano-bubbles stabilized in water by an electrically charged interface was strongly suggested.

6.2 Suggestions for Future Studies

The scattering light techniques used to obtain the particle size distribution showed consistent data with good repeatability. However, as an indirect method, the accuracy of the data is not assured. It would be interesting to verify the size and residence time of nano-bubbles using a direct method, such as electron microscopy combined with freeze fracture method.

In order to understand more about the stability of bubbles, it is suggested to measure the surface tension of the MNB water. A low surface tension could justify a lower internal pressure of nano-bubbles. Furthermore, the generation of micro- and nano-bubbles in solutions containing salts could give information about the relation between the nano-bubble stability and charge in the interface.

In addition, in this study, the generation and storage temperatures of the MNB water were kept constant at 20°C. The variation of the temperature should change the concentration of bubble size and number density. An investigation using different temperatures is encouraged.

Finally, there are still many investigations to be done concerning the elucidation of the mechanism of the acceleration in the physiological activity of living organisms caused by the micro- and nano-bubbles.

References

Abraham, R. J., Fisher, J., and Loftus, P. (1988). *Introduction to NMR Spectroscopy*. John Wiley and Sons, Chichester, England.

Ago, K., Nagasawa, K., Takita, J., Itano, R., Morii, N., Matsuda, K., and Takahashi, K. (2005). Development of an aerobic cultivation system by using a microbubble aeration technology. *Journal of Chemical Engineering of Japan*, 38(9):757–762.

ASABE (2009). *ASABE Standards 2009. Standard Engineering Practices Data*, chapter ASAE S318.4. Method of Determining and Expressing Fineness of Feed Materials by Sieving. ASABE, St. Joseph, USA, 56th edition.

Atkins, P. and de Paula, J. (2006). *Atkins' Physical Chemistry*. Oxford University Press, Oxford, 8th edition.

Auratec and Yahiro, T. (2001). Micro-bubble generating nozzle and application device therefor. Technical report, World Intellectual Property Organization, Patent no. WO/2001/036105.

Balci, M. (2005). *Basic ^{1}H- and ^{13}C-NMR Spectroscopy*, chapter 10: Absorption and Ressonance, pages 274–251. Elsevier, Amsterdam, Netherlands.

Berendsen, H. J. C. (1992). Rationale for using nmr to study water relations in foods and biologial tissues. *Trends in Food Science & Technology*, 3:202 – 205.

Bhushan, B., Wang, Y., and Maali, A. (2008). Coalescence and movement of nanobubbles studied with tapping mode afm and tip-bubble interaction analysis. *Journal of Physics: Condensed Matter*, 20:1–9.

Bredwell, M. D. and Worden, R. M. (1998). Mass-transfer properties of microbubbles. 1. experimental studies. *Biotechnology Progress*, 14(1):31–38.

Bunkin, N. F., Indukaev, K. V., and Ignat'ev, P. S. (2007). Spontaneous self-organization of microbubbles in a liquid. *Journal of Experimental and Theoretical Physics*, 104(3):486–498.

Bunkin, N. F., Suyazov, N. V., Shkirin, A. V., Ignat'ev, P. S., and Indukaev, K. V. (2008). Study of nanostructure of highly purified water by measuring scattering matrix elements of laser radiation. *Physics of Wave Phenomena*, 16(4):243–260.

Burns, S. E., Yiacoumi, S., and Tsouris, C. (1997). Microbubble generation for environmental and industrial separations. *Separation and Purification Technology*, 11(3):221–232.

Chu, L. B., Xing, X. H., Yu, A. F., Sun, X. L., and Jurcik, B. (2008). Enhanced treatment of practical textile wastewater by microbubble ozonation. *Process Safety and Environment Protection*, 86(5):389–393.

Clift, R., Grace, J. R., and Weber, M. E. (2005). *Bubbles, Drops and Particles*. Dover Publications, Mineola.

Colic, M. and Morse, D. (1999). The elusive mechanism of the magnetic 'memory' of water. *Colloids and Surfaces A: Physicochemical and Engineering Aspects*, 154(1–2):167–174.

Couto, H. J. B., Nunes, D. G., Neumann, R., and França, S. C. A. (2009). Micro-bubble size distribution measurements by laser diffraction technique. *Minerals Engineering*, 22:330 – 335.

Fujikawa, S., Zhang, R., Hayama, S., and Peng, G. (2003). The control of micro-air-bubble generation by a rotational porous plate. *International Journal of Multiphase Flow*, 29(8):1221–1236.

Gotoh, Y., Serizawa, A., Eguchi, T., Tanaka, H., and Izumi, M. (2006). Oil separation from oil polluted soil by micro bubble injection and separation mechanisms. *Japanese Journal of Multiphase Flow*, 20(1):39–49. (in Japanese).

Graciaa, A., Creux, P., and Lachaise, J. (2002). *Encyclopedia of Surface and Colloid Science*, volume 2, chapter Electrokinetics of bubbles, pages 1876 – 1886. Marcel Dekker, New York.

Graciaa, A., Morel, G., Saulner, P., Lachaise, J., and Schechter, R. S. (1995). The zeta-potential of gas bubbles. *Journal of Colloid and Interface Science*, 172:131 – 136.

Haedelt, J., Beckett, S. T., and Niranjan, K. (2007). Bubble-included chocolate: relating structure with sensory response. *Journal of Food Science E: Food Engineering and Physical Properties*, 72(3):138 – 141.

Hasegawa, H., Nagasaka, Y., and Kataoka, H. (2008). Electrical potential of microbubble generated by shear flow in pipe with slits. *Fluid Dynamics Research*, 40:554 – 564.

Hemmingsen, E. A. (2002). *Encyclopedia of Surface and Colloid Science*, volume 4, chapter Spontaneous gas bubble formation in water, pages 4775 – 4784. Marcel Dekker, New York.

Henry, D. C. (1931). The cathaphoresis of suspended solids. part i - the equation of cataphoresis. *Proceedings of the Royal Society of London A*, 133(821):106 – 129.

Himuro, S. (2007a). A new washing method using microbubbles. *Progress in Multiphase Flow Research*, 2:39–45. (in Japanese).

Himuro, S. (2007b). Physicochemical properties of micro-bubbles. *Chemical Engineering of Japan*, 71(3):165–169. (in Japanese).

Hindman, J. C., Svirmickas, A., and Wood, M. (1973). Relaxation process in water. a study of the proton spin-lattice relaxation time. *The Journal of Chemical Physics*, 59(3):1517–1522.

Kelsall, G. K., Tang, S., Yurdakul, S., and Smith, A. L. (1996). Electrophoretic behaviour of bubbles in aqueous electrolytes. *Journal of Chemical Society, Faraday Transactions*, 92:3887 – 3893.

Kerker, M. (1969). *The Scattering of Light and Other Electromagnetic Radiation*. Academic Press, San Diego.

Kikuchi, K., Ioka, A., Oku, T., Tanaka, Y., Saihara, Y., and Ogumi, Z. (2009). Concentration determination of oxygen nanobubbles in electrolyzed water. *Journal of Colloid and Interface Science*, 329(2):306–309.

Kodama, Y., Kakugawa, A., Takahashi, T., and Kawashima, H. (2000). Experimental study on microbubbles and their applicatibility to ships for skin friction reduction. *International Journal of Heat and Fluid Flow*, 21:582–588.

Kukizaki, M. and Goto, M. (2006). Size control of nanobubbles generated from shirasu-porous-glass (spg) membranes. *Journal of Membrane Science*, 281(1–2):386–396.

Kukizaki, M. and Wada, T. (2008). Effect of the membrane wettability on the size and size distribution of microbubbles formed from shirasu-porous-glas (spg) membranes. *Colloids and Surfaces A: Physicochemical and Engineering Aspects*, 317:146–154.

Kurata, K., Taniguchi, H., Fukunaga, T., Matsuda, J., and Higaki, H. (2007). Development of a compact microbubble generator and its usefulness for three-dimensional osteoblastic cell culture. *Journal of Biomechanical Science and Engineering*, 2(4):166–177.

Levitt, M. H. (2008). *Spin Dynamics: basics of nuclear magnetic resonance*. John Wiley and Sons, Chichester, 2nd edition.

Lewis, M. E. (2006). *Handbooks for Water – Resources Investigations*, volume 9, chapter 6.2. Dissolved Oxygen, pages 35 – 37. U. S. Geological Survey TWRI.

Li, P. and Tsuge, H. (2006a). Ozone transfer in a new gas-induced contactor with microbubbles. *Journal of Chemical Engineering of Japan*, 39(11):1213–1220.

Li, P. and Tsuge, H. (2006b). Water treatment by induced air flotation using microbubbles. *Journal of Chemical Engineering of Japan*, 39(8):896–903.

Lide, D. E., editor (2003). *Handbook of Chemistry and Physics*, chapter Magnetic Susceptibility of the Elements and Inorganic Compounds, pages 4–141 – 4–146. CRC Press, Boca Raton, 84th edition.

Ljunggren, S. and Eriksson, J. C. (1997). The lifetime of a colloid-sized gas bubble in water and the cause of hydrophobic attraction. *Colloids and Surfaces A: Physicochemical and Engineering Aspects*, 129–130:151–155.

Lyklema, J. (1991). *Fundamentals of Interface and Colloid Science*, volume I: Fundamentals. Academic Press, London.

Malvern (2003 – 2004). *Zetasizer Nano Series User Manual*. Malvern Instruments Ltd., Worcestershire.

Matsumoto, M. and Tanaka, K. (2008). Nano bubble – size dependence of surface tension and inside pressure. *Fluid Dynamics Research*, 40(7–8):546–553.

Matsuo, K., Maeda, K., Ohnari, H., Tsunami, Y., and Ohnari, H. (2006). Water purification of dam lake using micro bubble technology. *Progress in Multiphase Flow Research*, 1:279–286. (in Japanese).

Millero, F. J. (2001). *The Physical Chemistry of Natural Waters*. Wiley - Interscience, New York.

Nagayama, G., Tsuruta, T., and Cheng, P. (2006). Molecular dynamics simulation on bubble formation in a nanochannel. *International Journal of Heat and Mass Transfer*, 49(23–24):4437–4443.

Najafi, A. S., Drelich, J., Yeung, A., Xu, Z., and Masliyah, J. (2007). A novel method of measuring electrophoretic mobility of gas bubbles. *Journal of Colloid and Interface Science*, 308(2):344–350.

Ohgaki, K., Khan, N. Q., Joden, Y., Tsuji, A., and Nakagawa, T. (2010). Physicochemical approach to nanobubbles solution. *Chemical Engineering Science*, 65(3):1296–1300.

Ohnari, H. (2007). Swing type fine air bubble generation device. *US Patent 7261283*.

Onari, H. (2001). Fisheries experiments of cultivated shells using micro-bubbles techniques. *Journal of Heat Transfer Society of Japan*, 40(160):2–7. (in Japanese).

Oshita, S., Seo, Y., and Kawagoe, Y. (1999). Relaxation time of protons in intracellular water of broccoli. *Agricultural Engineering International: The CIGR E-Journal*, vol. I. URL: http://www.cigrjournal.org/index.php/Ejounral/article/viewFile/1040/1033. Last access: February 9th, 2010.

Park, J. and Kurata, K. (2009). Application of microbubbles to hydroponics solution promotes lettuce growth. *Hort Technology*, 19(1):212–215.

Richardson, R. (2008). *Colloid Science: Principles, methods and applications*, chapter 12: Scattering and Reflection Techniques, pages 228 – 254. Blackwell Publishing, Oxford.

Sadatomi, M., Kawahara, A., Kano, K., and Ohtomo, A. (2005). Performance of a new microbubble generator with a spherical body in a flowing water tube. *Experimental Thermal and Fluid Science*, 29(5):615–623.

Serizawa, A., Inui, T., Yahiro, T., and Kawara, Z. (2003). Laminarization of micro-bubble containing milky bubbly flow in a pipe. In *Proceedings of the 3rd European-Japanese Two-Phased Flow Group Meeting*, September, 2003, Certosa di Pontignano, Italy.

Simpson, J. H. and Carr, H. U. (1958). Diffusion and nuclear spin relaxation in water. *The Physical Review*, 111(5):1201–1202.

Smoluchowski, M. (1914). *Handbuch der Elektrizität und des Magnetismus*, volume 2. Johann Ambrosius Barth, Leipzig.

Spanos, N., Klepetsanis, P. G., and Koutsoukos, P. G. (2002). *Encyclopedia of Surface and Colloid Science*, volume 1, chapter Calculation of zeta-potentials from electrokinetic data, pages 829 – 845. Marcel Dekker, New York.

Tabei, K., Haruyama, S., Yamaguchi, S., Shirai, H., and Takakusagi, F. (2007). Study of micro bubble generation by a swirl jet. *Journal of Environment and Engineering*, 2(1):172–182.

Takahashi, M. (2005). Zeta potential of microbubbles in aqueous solutions: Electrical properties of the gas-water interface. *Journal of Physical Chemistry B*, 190(46):21858–21864.

Takahashi, M., Chiba, K., and Li, P. (2007). Free-radical generation from collapsing microbubbles in the absence of a dynamic stimulus. *The Journal of Physical Chemistry B*, 111(6):1343–1347.

Takahashi, M., Kawamura, T., Yamamoto, Y., Onari, H., Himuro, S., and Shakutsui, H. (2003). Effect of shrinking microbubble on gas hydrate formation. *The Journal of Physical Chemistry B*, 107(10):2171–2173.

Tolman, R. C. (1949). The effect of droplet size on surface tension. *The Journal of Chemical Physics*, 17(3):333 –337.

Traficante, D. D. (1996). *Encyclopedia of Nuclear Magnetic Resonance*, volume 6, chapter Relaxation: An Introduction, pages 3988 – 4003. Wiley, New York.

Tsai, J., Kumar, M., Chen, S., and Lin, J. (2007). Nano-bubble flotation technology with coagulation process for the cost-effective treatment of chemical mechanical polishing wastewater. *Separation and Purification Technology*, 58(1):61–67.

Tsuge, H. (2007a). *The latest technology on microbubbles and nanobubbles*, chapter 1: Maikurobaburu no tokusei (Special characteristics of microbubbles), pages 1–14. CMC, Tokyo. (in Japanese).

Tsuge, H. (2007b). *The latest technology on microbubbles and nanobubbles*, chapter 2: Maikurobaburu no hasseihou (Micro-bubble Generation Methods), pages 15–30. CMC, Tokyo. (in Japanese).

Tyrrell, J. W. and Attard, P. (2002). Atomic force microscope imges of nanobubbles on a hydrophobic surface and corresponding force-separation data. *Langmuir*, 18:160–167.

Ushikubo, F. Y., Furukawa, T., Oshita, S., Furihata, K., Makino, Y., Kawagoe, Y., and Shiina, T. (2007). Dynamic properties of water containing micro and nanobubbles. In *Proceedings of the International Agricultural Engineering Conference (IAEC)*, December, 2007, AIT, Bangkok, Thailand.

Ushikubo, F. Y., Nakagawa, R., Furukawa, T., Makino, Y., Kawagoe, Y., and Shiina, T. (2009). A study of the effect of micro and nano-bubbles in the dynamic properties of water. In *Proceedings of the 5th CIGR Section VI International Syposium on Food Processing, Monitoring Tecnology in Bioprocesses and Food Quality Management*, August - September, 2009, Potsdam, Germany.

Ushikubo, F. Y., Oshita, S., Furukawa, T., Makino, Y., Kawagoe, Y., and Shiina, T. (2008). A study of water containing micro and nano-bubbles and its possible effect on physiological activity. In *Proceedings of International Conference of Agricultural Engineering*, August - September, 2008, Iguassu Falls City, Brazil.

Usui, S. and Sasaki, H. (1978). Zeta potential measurements of bubbles in aqueous surfactant solutions. *Journal of Colloid and Interface Science*, 65(1):36 –45.

Vallée, P., Lafait, J., Legrand, L., Mentré, P., Monod, M. O., and Thomas, Y. (2005). Effects of pulsed low-frequency electromagnetic fields on water characterized by light scattering techniques: role of bubbles. *Langmuir*, 21(6):2293–2299.

Vicent, B. (2005). *Colloid Science: Principles, methods and applications*, chapter 1: Introduction to Colloidal Dispersions, pages 1–13. Blackwell Publishing, Oxford.

Wu, Z., Chen, H., Dong, Y., Mao, H., Sun, J., Chen, S., and Craig, V. S. J. (2008). Cleaning using nanobubbles: defouling by electrochemical generation of bubbles. *Journal of Colloid and Interface Science*, 328(1):10–14.

Xu, Q., Nakajima, M., Ichikawa, S., Nakamura, N., Roy, P., Okadome, H., and Shiina, T. (2009). Effects of surfactant and electrolyte concentrations on bubble formation and stabilization. *Journal of Colloid and Interface Science*, 332:208 – 214.

Xu, Q., Nakajima, M., Ichikawa, S., Nakamura, N., and Shiina, T. (2008). A comparative study of microbubble generation by mechanical agitation and sonication. *Innovative Food Science and Emerging Technologies*, 9(4):489–494.

Yamada, S., Yoshimi, Y., Terada, T., Ohno, K., and Minagawa, H. (2007). Study on oxygen supplying of the micro-bubbles generated by the pressurizing dissolution method. *Japanese Journal of Multiphase Flow*, 21(1):84–90.

Yasuno, M., Sugiura, S., Iwamoto, S., Nakajima, M., Shono, A., and Satoh, K. (2004). Monodispersed microbubble formation using microchannel technique. *American Institute of Chemical Engineers Journal*, 50(12):3227–3233.

Yezek, L. (2002). *Encyclopedia of Surface and Colloid Science*, volume 4, chapter Studying surfactant adsorption onto colloidal particles using the electrophoretic fingerprinting approach, pages 4899 – 4908. Marcel Dekker, New York.

Zhang, X. H., Maeda, N., and Craig, V. S. J. (2006). Physical properties of nanobubbles on hydrophobic surfaces in water and aqueous solutions. *Langmuir*, 22:5025–5035.

Appendix 1

Particle Size Distribution obtained by Laser Diffraction

The geometric mean, the geometric standard deviation and the coefficient of variation of the particle diameter obtained by laser diffraction method are shown in the tables below. Table A1.1 presents the data obtained during the production of O_2 MNB water (from 5 to 30 min), Table A1.2 shows the values measured in O_2 MNB water after stopping the bubble production (from the moment just after stopping the bubble generation to 60 min later) and Table A1.3 refers to the measurements in air MNB water during the bubble generation (from 2 to 40 min). The bubbles were generated in Aura-tec micro-bubble generator. The geometric mean was calculated based on the frequency in number of particles.

The particle size distribution graphs are not shown in this section, as there were few changes in the curves shape with time. The size distribution curve patterns obtained are shown in Figure 4.2 (O_2 MNB water) and in Figure 4.3 (air MNB water) in Chapter 4.

Table A1.1: Geometric mean (d_g), geometric standard deviation (S_g) and coefficient of variation (CV) obtained by laser diffraction method during the O_2 MNB generation. Frequency in number of particles.

Time (min)	d_g (μm)	S_g	CV (%)
5	69	19	27.2
10	67	18	26.8
20	60	17	28.4
30	56	17	30.5

Table A1.2: Geometric mean (d_g), geometric standard deviation (S_g) and coefficient of variation (CV) obtained by laser diffraction method after stopping the O_2 MNB generation. Frequency in number of particles.

Time (min)	d_g (μm)	S_g	CV (%)	Time (min)	d_g (μm)	S_g	CV (%)
0	63	24	38.2	13	0.188	0.029	15.4
1.5	152	23	15.1	14	0.188	0.029	15.4
2.5	164	20	12.1	15	0.190	0.030	15.7
3.5	151	23	15.2	16	0.190	0.033	17.1
5	155	22	14.5	17	0.184	0.026	14.4
6	0.190	0.030	16.0	18	0.192	0.031	16.3
7	152	23	15.1	19	0.198	0.039	19.6
8	152	23	15.1	20	0.189	0.030	15.7
9	0.212	0.025	12.0	30	0.219	0.045	20.4
10	0.188	0.029	15.5	50	0.099	0.022	22.2
11	0.194	0.033	17.0	55	0.190	0.030	15.7
12	0.194	0.034	17.4	60	0.195	0.032	16.3

Table A1.3: Geometric mean (d_g), geometric standard deviation (S_g) and coefficient of variation (CV) obtained by Laser Diffraction method during the air MNB generation. Frequency in number of particles.

Time (min)	d_g (μm)	S_g	CV (%)
2	49	15	29.9
5	45	16	36.2
10	47	16	34.3
20	47	16	34.6
30	47	16	34.3
40	47	16	34.6

Appendix 2

Particle Size Distribution obtained by DLS (red laser)

The average particle size distribution curves of each sample are shown in the following figures. A visual pattern was adopted in order to make easier the identification of the samples and the kind of data. The particle size distribution curves of control water were represented by orange marks and lines while those of the water after the bubble generation are shown in dark blue marks and lines.

The particle size distribution curves of the control water (distilled, ion-exchange and ultra-pure water) and the O_2 MNB water produced in Nikiso micro-bubble generator are shown from Figure A2.1 to Figure A2.18. The graphs are the average mean of the 5 to 10 replications. The vertical bars represent the standard deviation calculated for each size interval. The frequencies are expressed as intensity of scattered light and as number of particles for each time.

In the captions, the values of geometric mean diameter (d_g), geometric standard deviation (S_g) and coefficient of variation (CV) are presented.

Control water

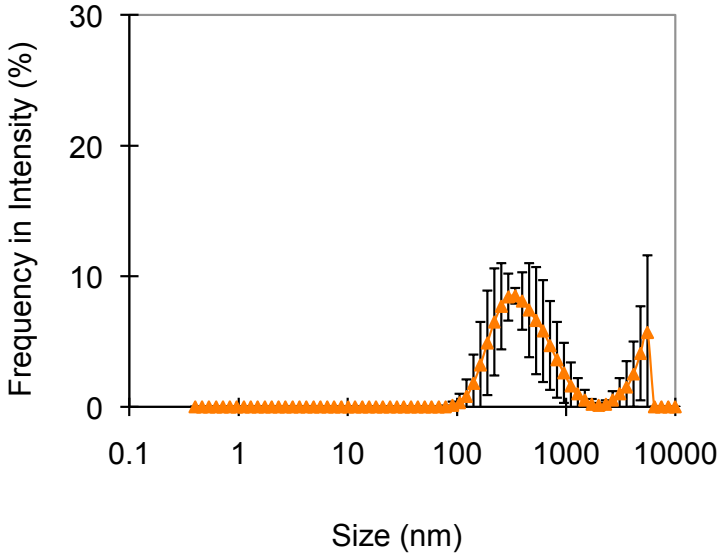

Figure A2.1: Average particle size distribution ($n = 5$), in intensity of scattered light of distilled water, ($d_g = 519$ nm, $S_g = 638$ nm, $CV = 122.8\%$)

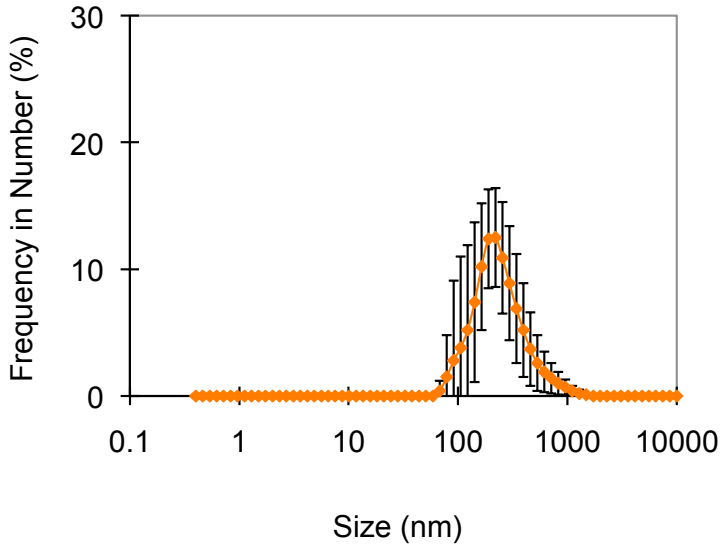

Figure A2.2: Average particle size distribution ($n = 5$), in number of particles of distilled water, ($d_g = 213$ nm, $S_g = 188$ nm, $CV = 55.3\%$).

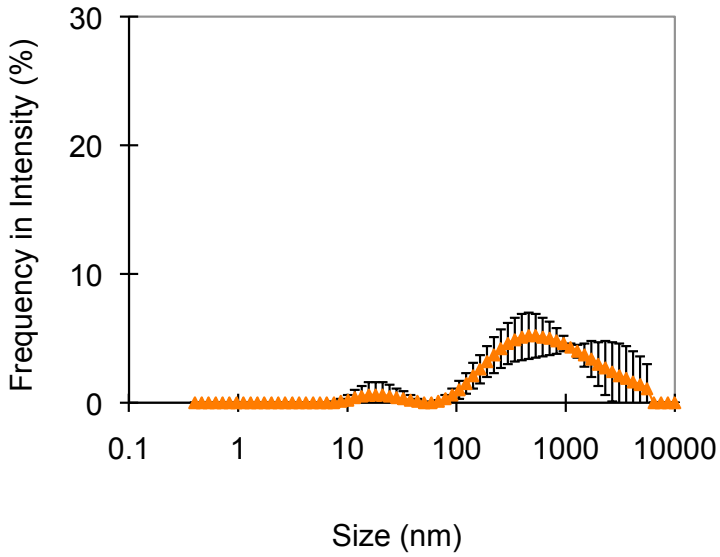

Figure A2.3: Average particle size distribution ($n = 5$), in intensity of scattered light of distilled water treated with a 0.45 μm filter, ($d_g = 526$ nm, $S_g = 801$ nm, $CV = 152.2\%$).

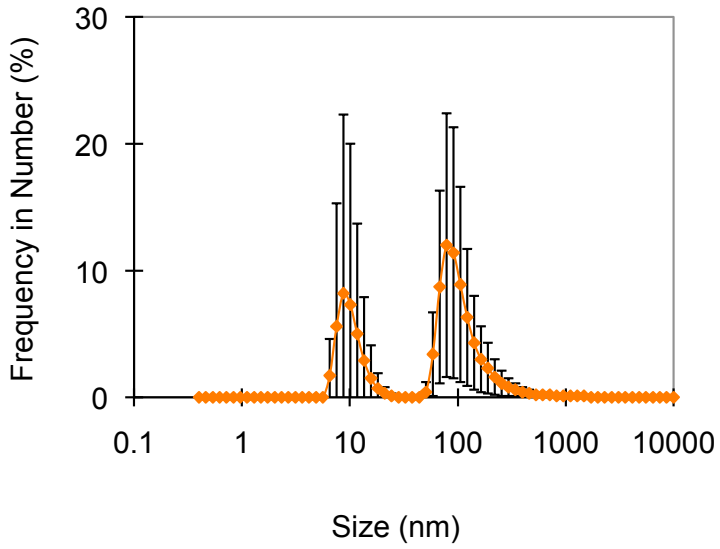

Figure A2.4: Average particle size distribution ($n = 10$), in number of particles of distilled water treated with a 0.45 μm filter, ($d_g = 45$ nm, $S_g = 67$ nm, $CV = 150.1\%$).

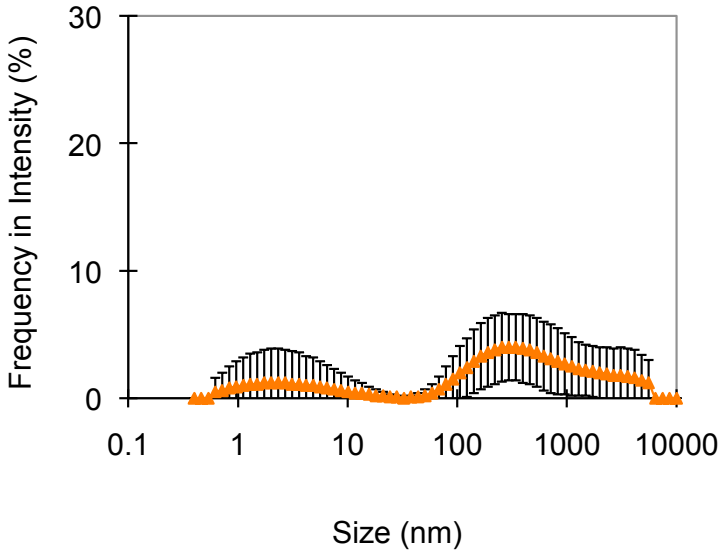

Figure A2.5: Average particle size distribution ($n = 5$), in intensity of scattered light of distilled water treated with a 0.20 μm filter, ($d_g = 169$ nm, $S_g = 883$ nm, $CV = 521.5\%$).

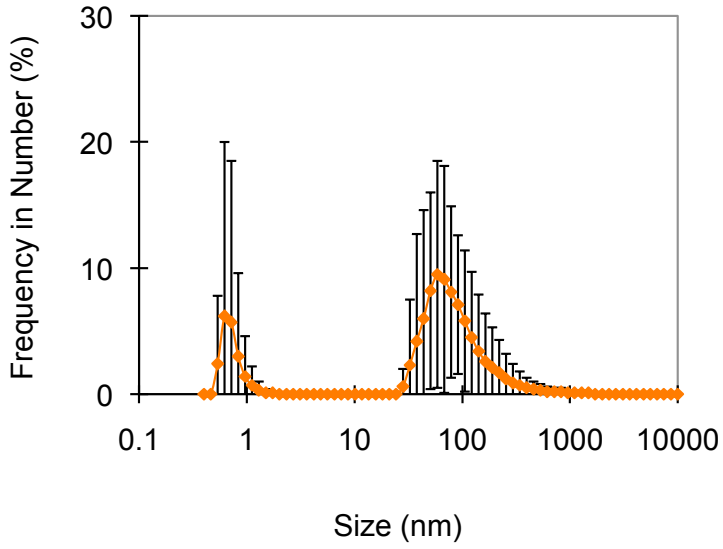

Figure A2.6: Average particle size distribution ($n = 5$), in number of particles of distilled water treated with a 0.20 μm filter, ($d_g = 30$ nm, $S_g = 105$ nm, $CV = 353.6\%$).

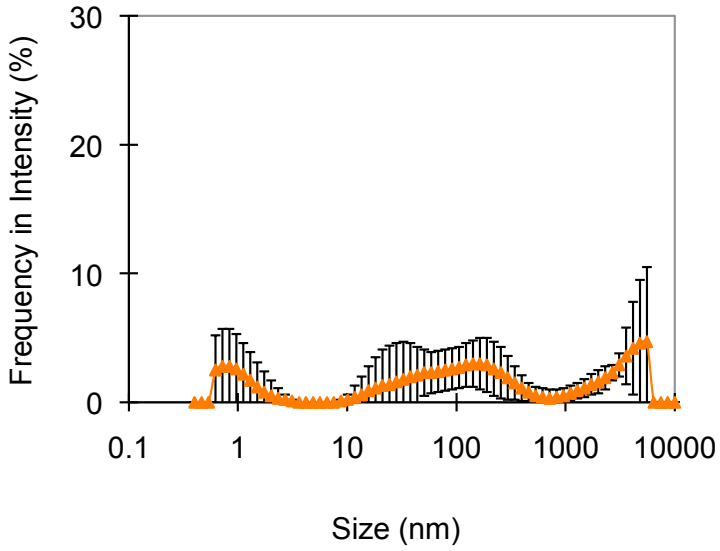

Figure A2.7: Average particle size distribution ($n = 5$), in intensity of water treated with ion exchange process, ($d_g = 114$ nm, $S_g = 954$ nm, $CV = 838.4\%$).

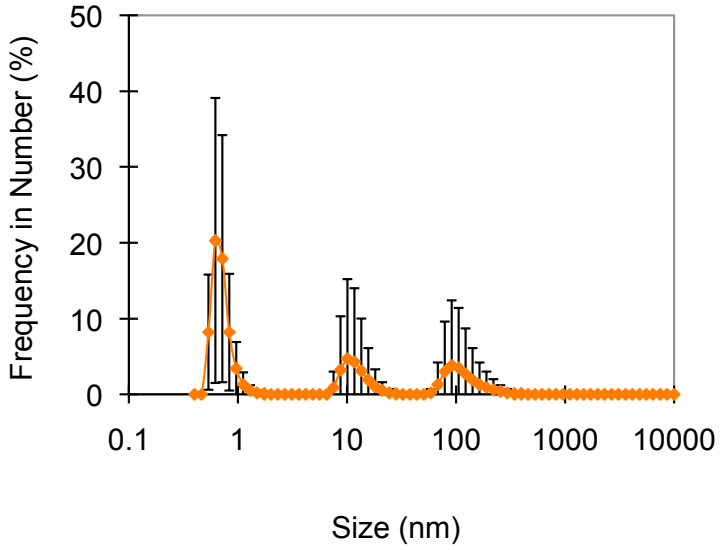

Figure A2.8: Average particle size distribution ($n = 5$), in number of particles of water treated with ion exchange process, ($d_g = 3$ nm, $S_g = 12$ nm, $CV = 393.5\%$).

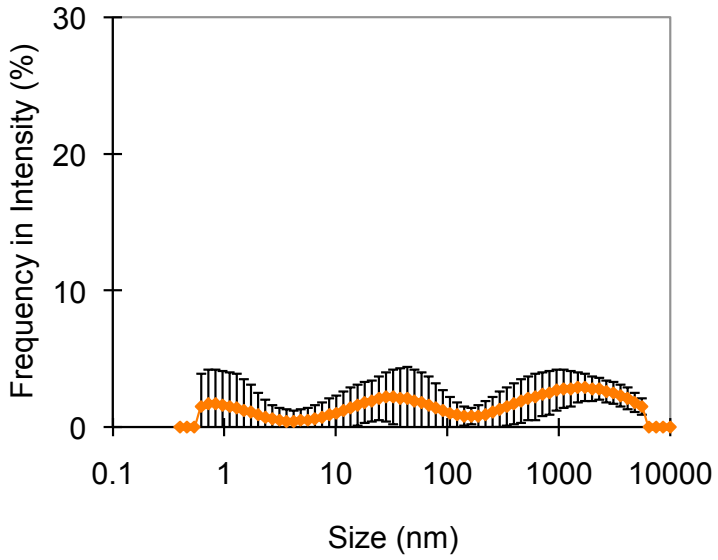

Figure A2.9: Average particle size distribution ($n = 10$), in intensity of scattered light of ultrapure water without degassing ($DO = 8.8$ mg·L^{-1}), ($d_g = 115$ nm, $S_g = 836$ nm, $CV = 726.8\%$).

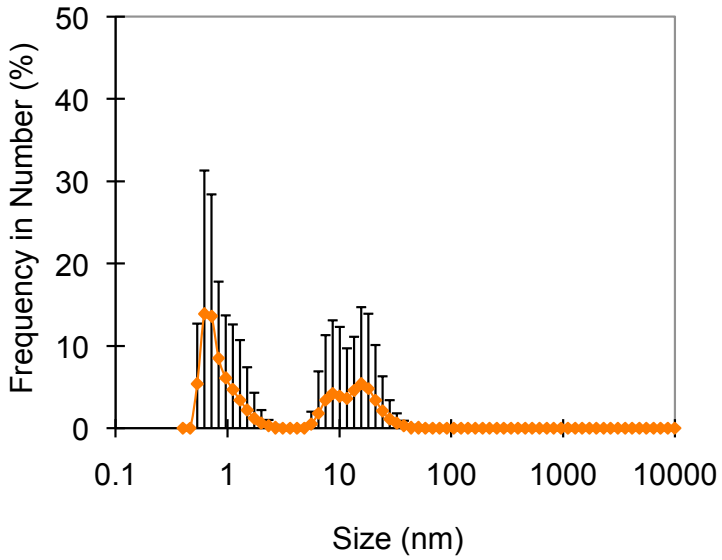

Figure A2.10: Average particle size distribution ($n = 10$), in number of particles of ultrapure water without degassing ($DO = 8.8$ mg·L^{-1}), ($d_g = 2$ nm, $S_g = 5$ nm, $CV = 194.9\%$).

Oxygen MNB Water

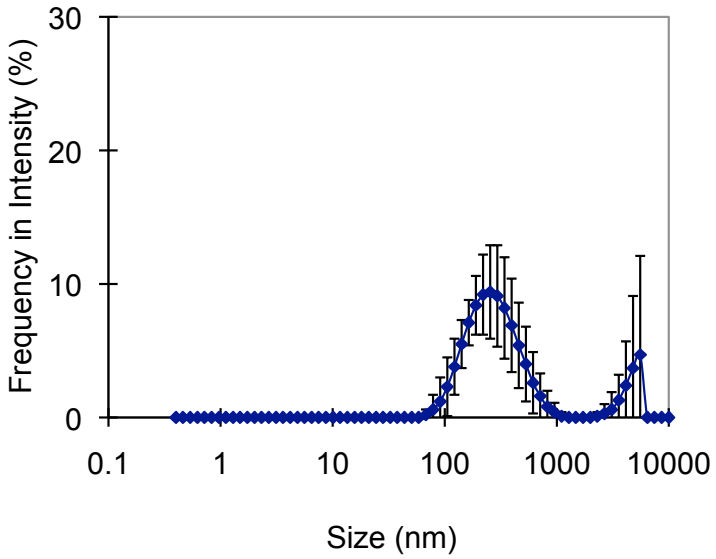

Figure A2.11: Average particle size distribution ($n = 5$), in intensity of scattered light of O_2 MNB water 20 min after stopping the bubble generation ($DO = 37.9$ mg·L^{-1}), ($d_g = 240$ nm, $S_g = 128$ nm, $CV = 53.0\%$).

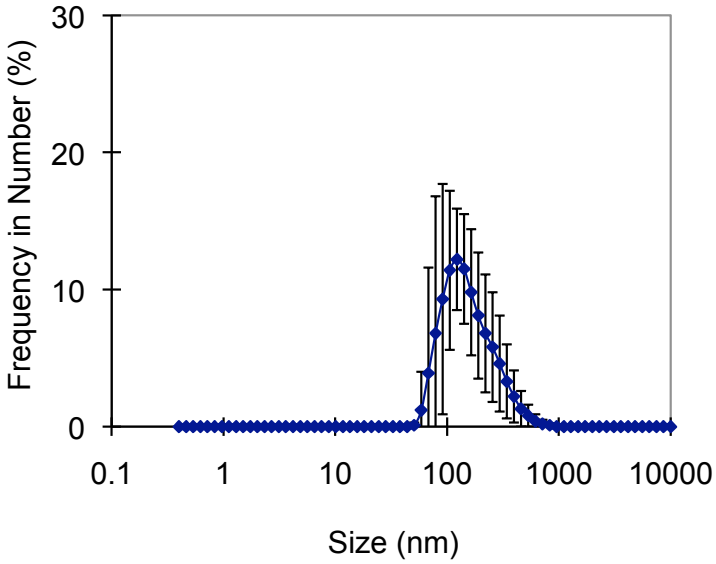

Figure A2.12: Average particle size distribution ($n = 5$), in number of particles of O_2 MNB water 20 min after stopping the bubble generation ($DO = 37.9$ mg·L^{-1}), ($d_g = 139$ nm, $S_g = 72$ nm, $CV = 51.9\%$).

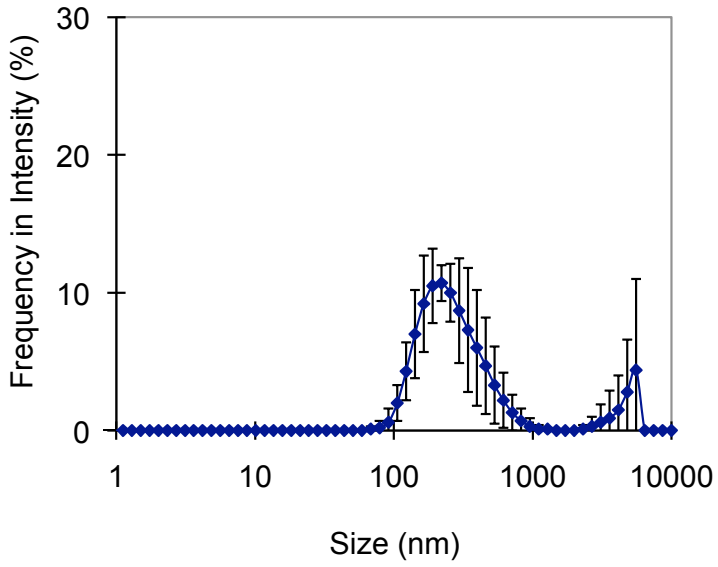

Figure A2.13: Average particle size distribution ($n = 5$), in intensity of scattered light of O_2 MNB water 5 h after stopping the bubble generation ($DO = 35.5$ mg·L^{-1}), ($d_g = 230$ nm, $S_g = 115$ nm, $CV = 49.9\%$).

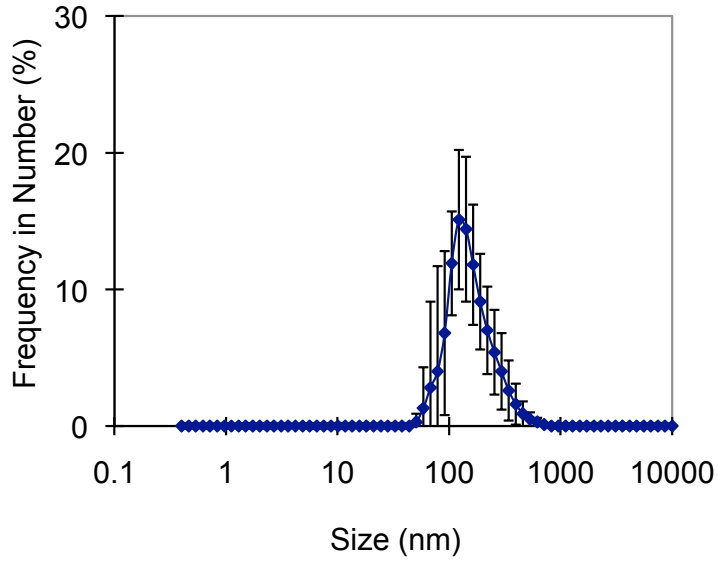

Figure A2.14: Average particle size distribution ($n = 5$), in number of particles of O_2 MNB water 5 h after stopping the bubble generation ($DO = 35.5$ mg·L^{-1}), ($d_g = 139$ nm, $S_g = 64$ nm, $CV = 45.9\%$).

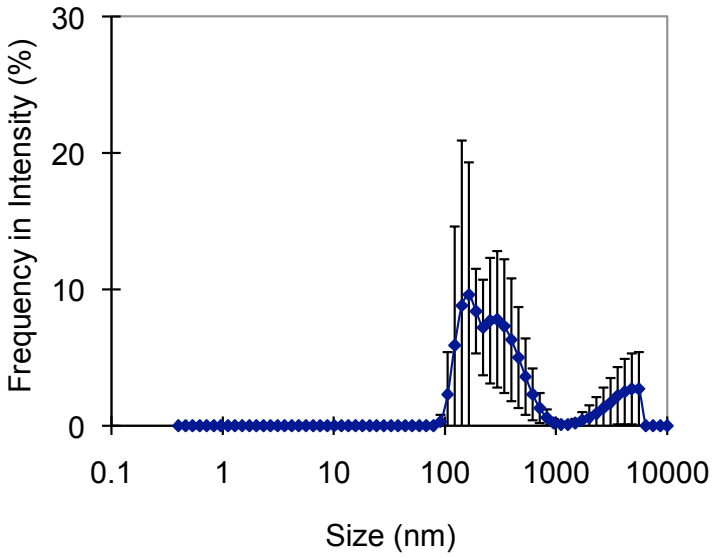

Figure A2.15: Average particle size distribution ($n = 5$), in intensity of scattered light of O_2 MNB water 1 d after stopping the bubble generation ($DO = 36.5$ mg·L^{-1}), ($d_g = 228$ nm, $S_g = 119$ nm, $CV = 52.4\%$).

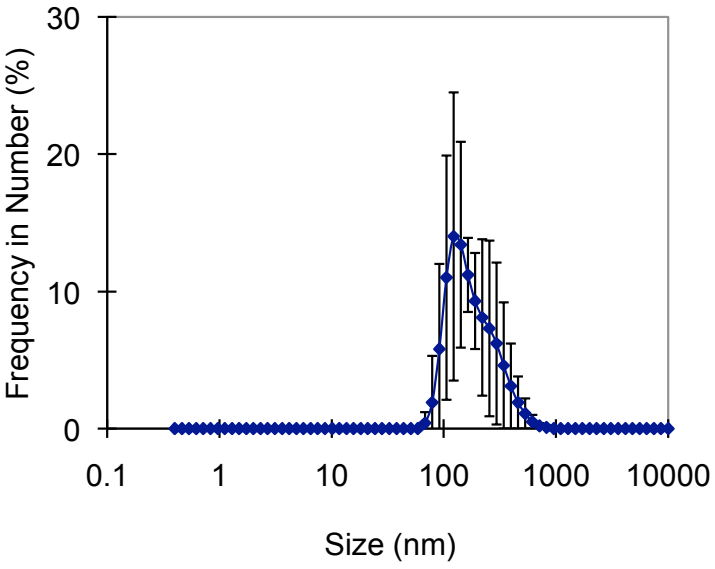

Figure A2.16: Average particle size distribution ($n = 5$), in number of particles of O_2 MNB water 1 d after stopping the bubble generation ($DO = 36.5$ mg·L^{-1}), ($d_g = 160$ nm, $S_g = 76$ nm, $CV = 47.6\%$).

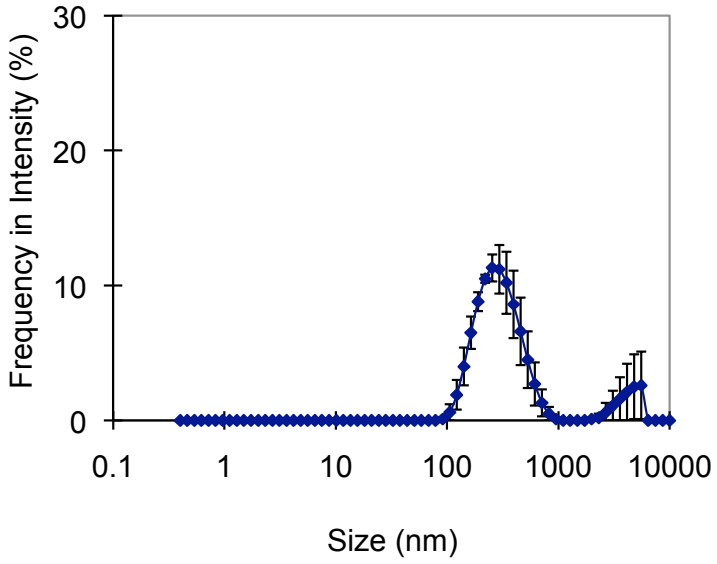

Figure A2.17: Average particle size distribution ($n = 5$), in intensity of scattered light of O_2 MNB water 2 d after stopping the bubble generation ($DO = 33.8$ mg·L^{-1}), ($d_g = 261$ nm, $S_g = 115$ nm, $CV = 43.9\%$).

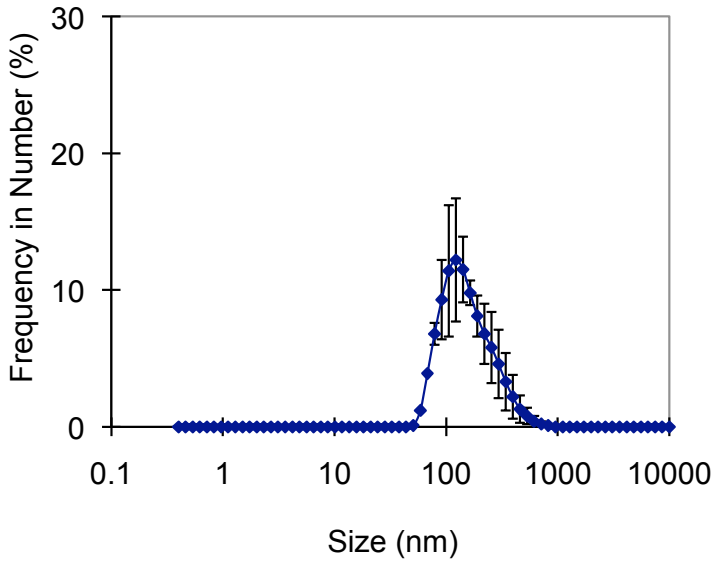

Figure A2.18: Average particle size distribution ($n = 5$), in number of particles of O_2 MNB water 2 d after stopping the bubble generation ($DO = 33.8$ mg·L^{-1}), ($d_g = 178$ nm, $S_g = 77$ nm, $CV = 43.2\%$).

Appendix 3

Particle Size Distribution obtained by DLS (green laser)

The particle size distribution curves of the control water (ultrapure water) and the O_2 MNB water produced in Aura-tec micro-bubble generator are shown from Figure A3.1 to Figure A3.38. The graphs are the average mean of the 5 to 10 replications. The vertical bars represent the standard deviation calculated for each size interval. The frequencies are expressed as intensity of scattered light and as number of particles for each time.

Control Water

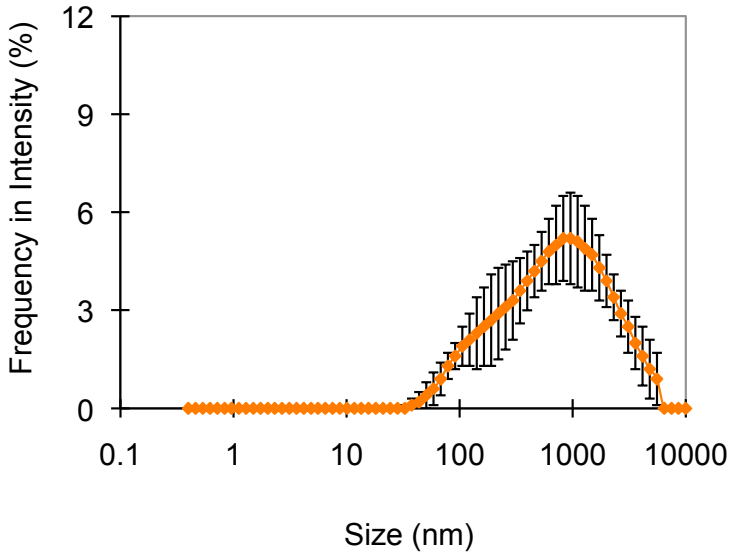

Figure A3.1: Average particle size distribution ($n = 10$), in intensity of scattered light of ultrapure water before degassing ($DO = 10.1$ mg·L^{-1}), ($d_g = 612$ nm, $S_g = 800$ nm, $CV = 130.8\%$).

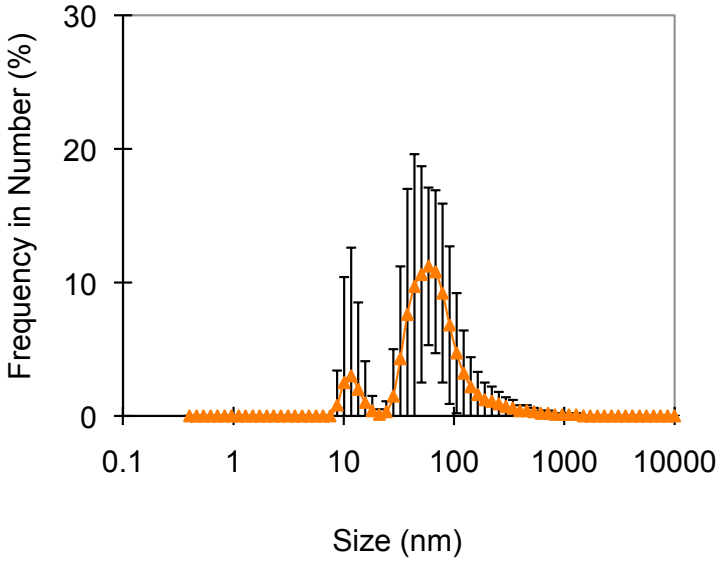

Figure A3.2: Average particle size distribution ($n = 10$), in number of particles of ultrapure water before degassing ($DO = 10.1$ mg·L^{-1}), ($d_g = 54$ nm, $S_g = 46$ nm, $CV = 84.4\%$).

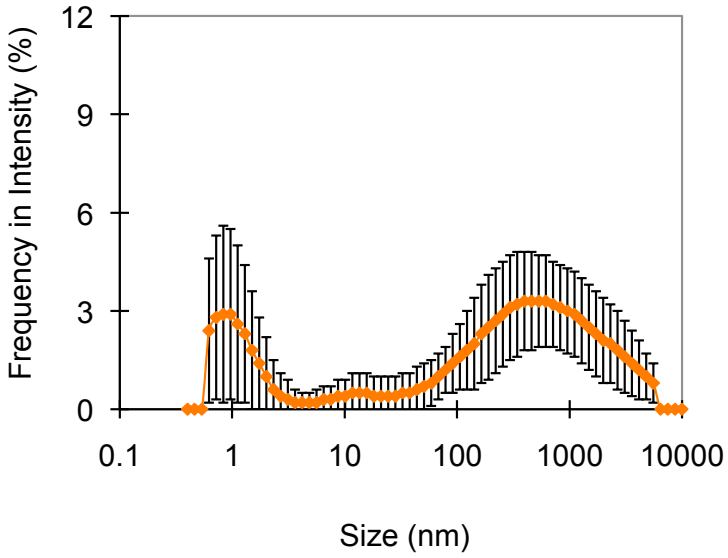

Figure A3.3: Average particle size distribution ($n = 10$), in intensity of scattered light of ultrapure water after degassing, ($DO = 7.6$ mg·L^{-1}), ($d_g = 106$ nm, $S_g = 839$ nm, $CV = 794.5\%$).

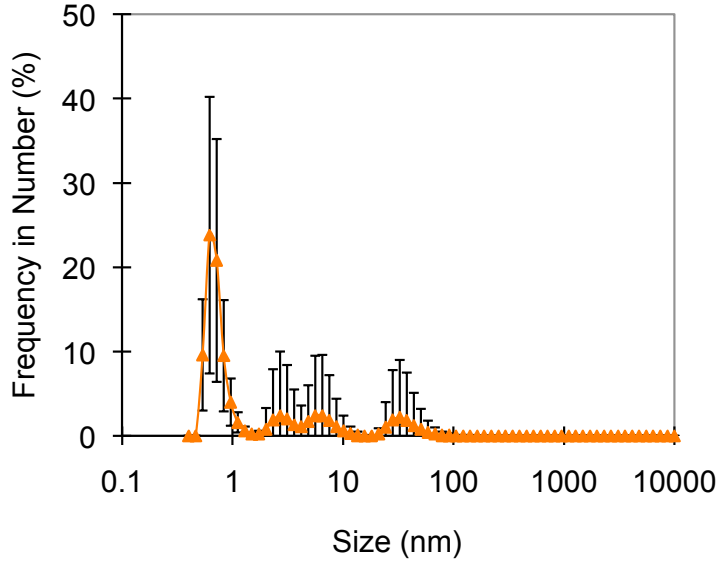

Figure A3.4: Average particle size distribution ($n = 10$), in number of particles of ultrapure water after degassing, ($DO = 7.6$ mg·L^{-1}), ($d_g = 1$ nm, $S_g = 2$ nm, $CV = 172.4\%$).

Oxygen MNB Water

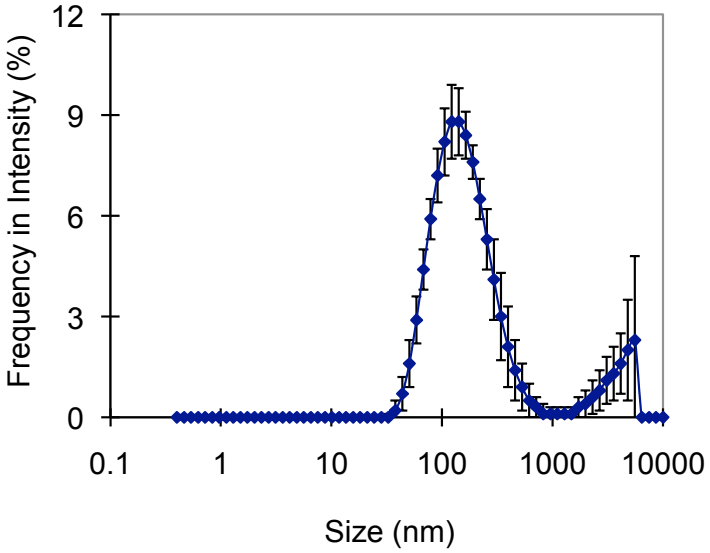

Figure A3.5: Average particle size distribution ($n = 10$), in intensity of scattered light of O_2 MNB water just after stopping the bubble generation ($DO = 36.9$ mg·L^{-1}), ($d_g = 137$ nm, $S_g = 84$ nm, $CV = 61.2\%$).

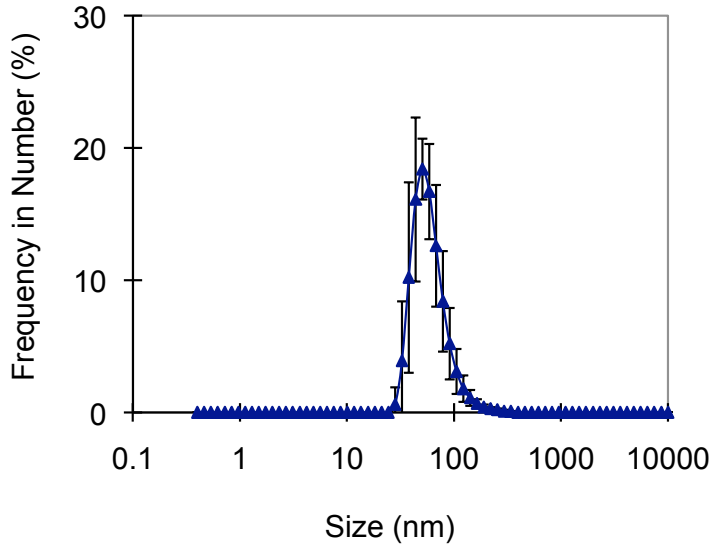

Figure A3.6: Average particle size distribution ($n = 10$), in number of particle of O_2 MNB water just after stopping the bubble generation ($DO = 36.9$ mg·L^{-1}), ($d_g = 54$ nm, $S_g = 20$ nm, $CV = 37.0\%$).

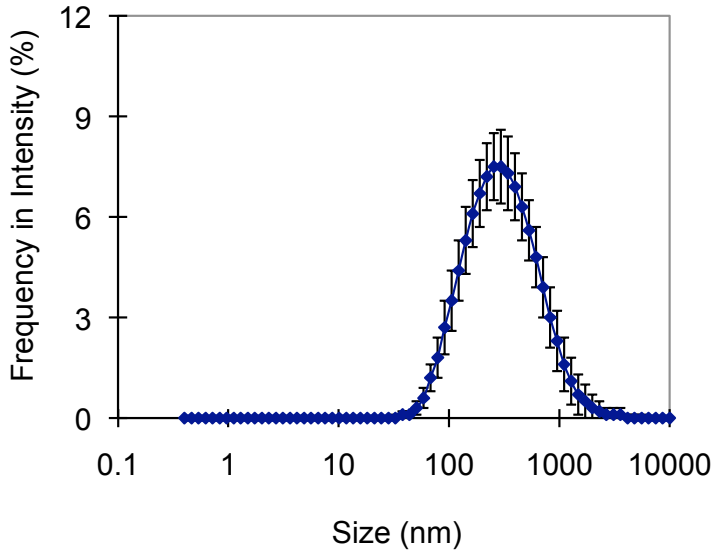

Figure A3.7: Average particle size distribution ($n = 10$), in intensity of scattered light of O_2 MNB water 1 h after stopping the bubble generation, ($d_g = 272$ nm, $S_g = 220$ nm, $CV = 81.1\%$).

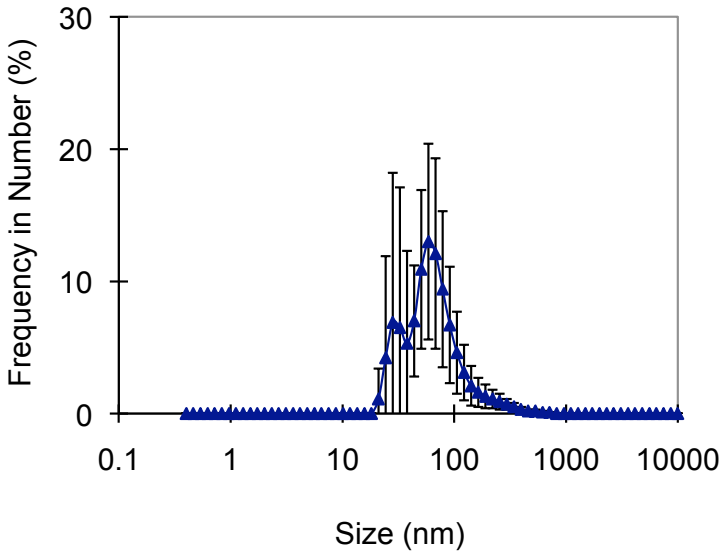

Figure A3.8: Average particle size distribution ($n = 10$), in number of particle of O_2 MNB water 1 h after stopping the bubble generation, ($d_g = 57$ nm, $S_g = 35$ nm, $CV = 61.8\%$).

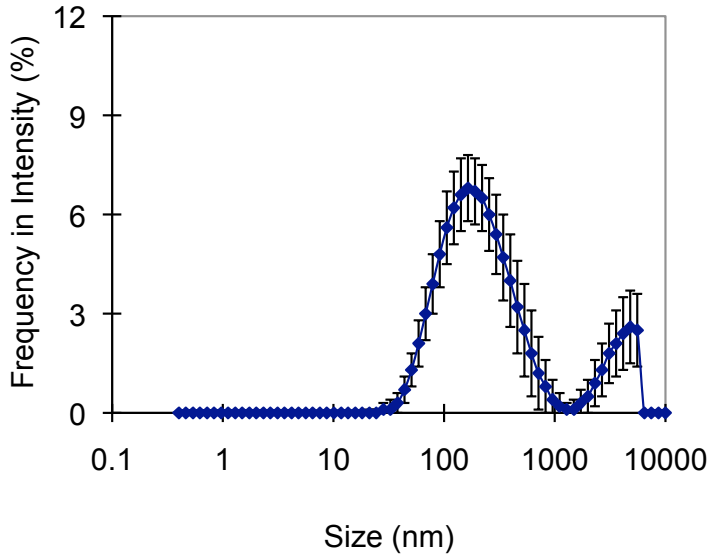

Figure A3.9: Average particle size distribution ($n = 10$), in intensity of scattered light of O_2 MNB water 2 h after stopping the bubble generation, ($d_g = 171$ nm, $S_g = 127$ nm, $CV = 74.1\%$).

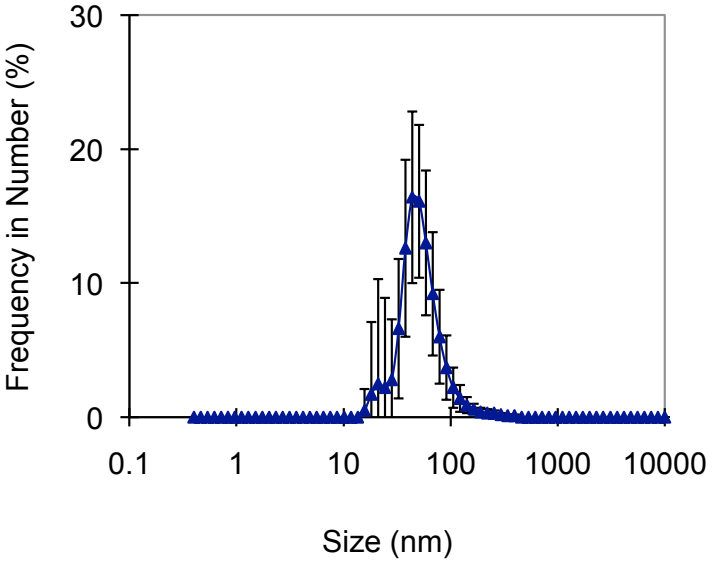

Figure A3.10: Average particle size distribution ($n = 10$), in number of particle of O_2 MNB water 2 h after stopping the bubble generation, ($d_g = 47$ nm, $S_g = 22$ nm, $CV = 46.7\%$).

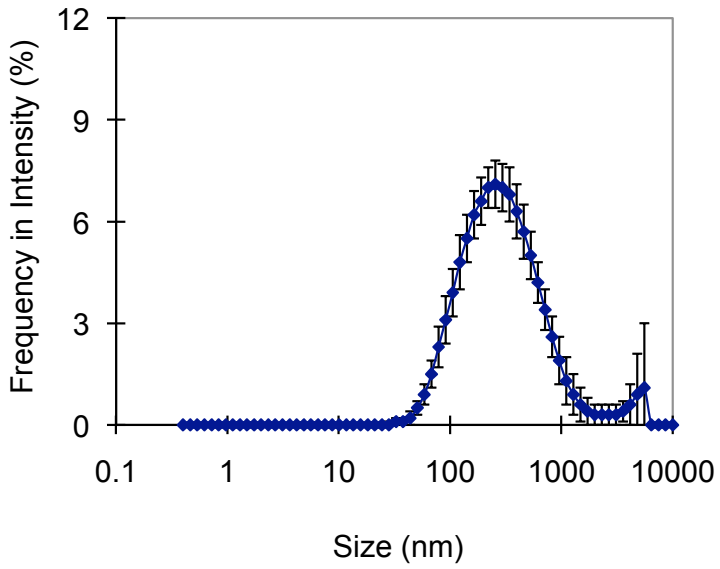

Figure A3.11: Average particle size distribution ($n = 10$), in intensity of scattered light of O_2 MNB water 1 d after stopping the bubble generation, ($d_g = 254$ nm, $S_g = 216$ nm, $CV = 85.0\%$).

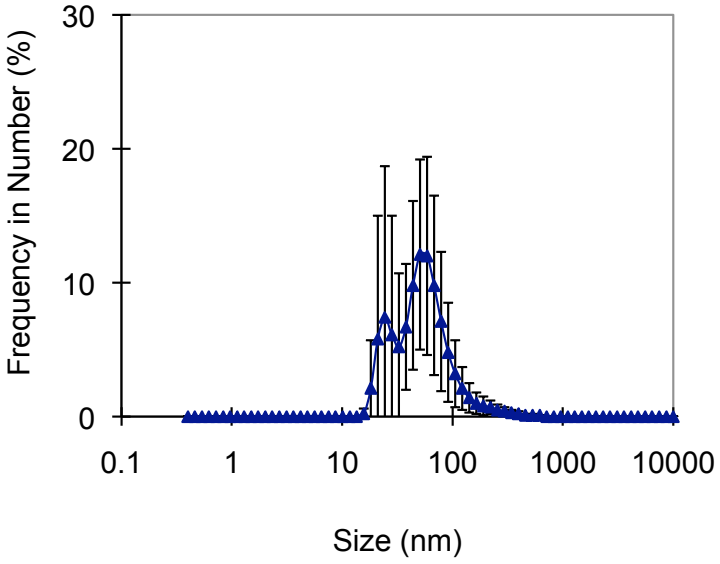

Figure A3.12: Average particle size distribution ($n = 10$), in number of particle of O_2 MNB water 1 d after stopping the bubble generation, ($d_g = 47$ nm, $S_g = 29$ nm, $CV = 61.9\%$).

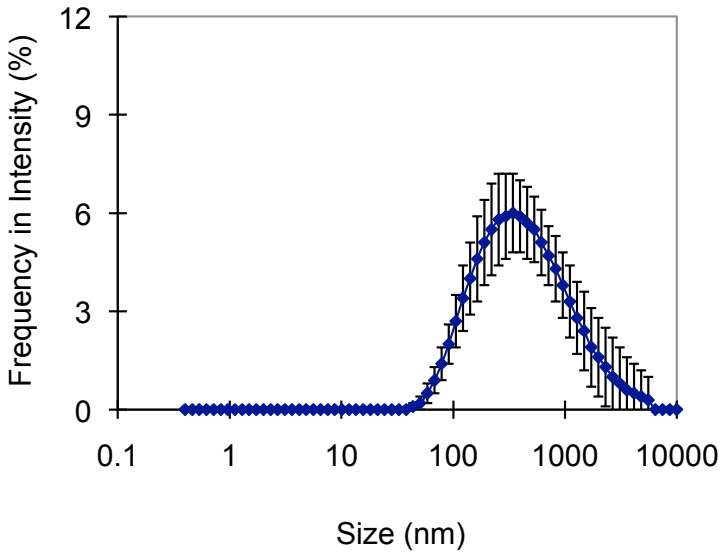

Figure A3.13: Average particle size distribution ($n = 10$), in intensity of scattered light of O_2 MNB water 3 d after stopping the bubble generation, ($d_g = 380$ nm, $S_g = 408$ nm, $CV = 107.4\%$).

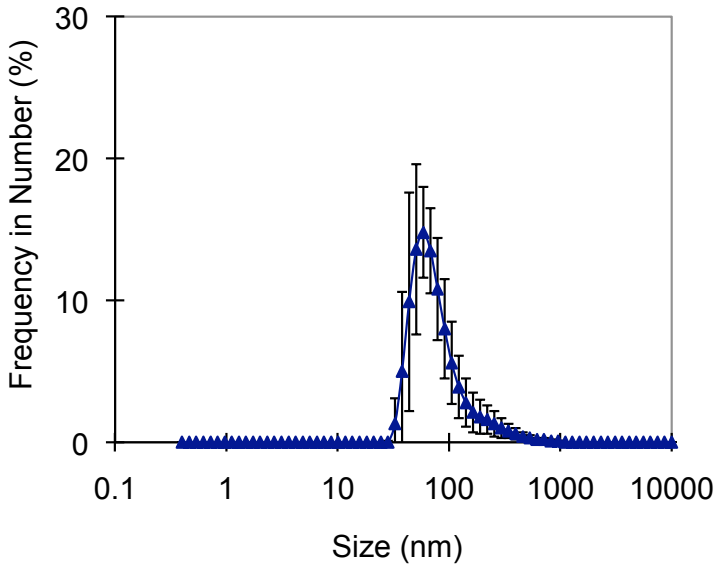

Figure A3.14: Average particle size distribution ($n = 10$), in number of particle of O_2 MNB water 3 d after stopping the bubble generation, ($d_g = 70$ nm, $S_g = 40$ nm, $CV = 57.5\%$).

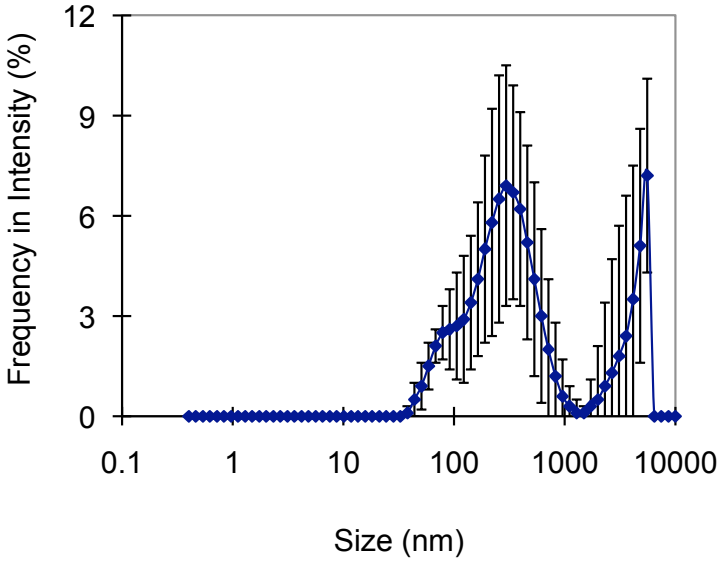

Figure A3.15: Average particle size distribution ($n = 10$), in intensity of scattered light of O_2 MNB water 6 d after stopping the bubble generation ($DO = 8.9$ mg·L^{-1}), ($d_g = 432$ nm, $S_g = 783$ nm, $CV = 181.2\%$).

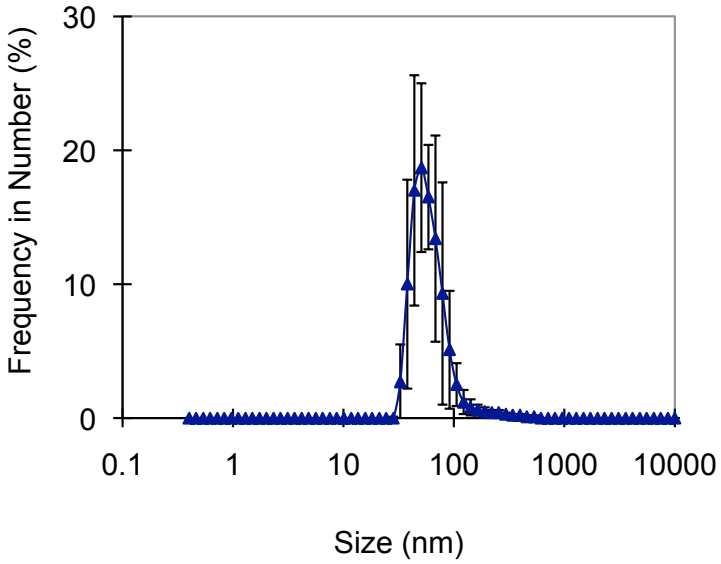

Figure A3.16: Average particle size distribution ($n = 10$), in number of particles of O_2 MNB water 6 d after stopping the bubble generation ($DO = 8.9$ mg·L^{-1}), ($d_g = 55$ nm, $S_g = 22$ nm, $CV = 39.5\%$).

O_2 MNB Water, High Initial DO Concentration

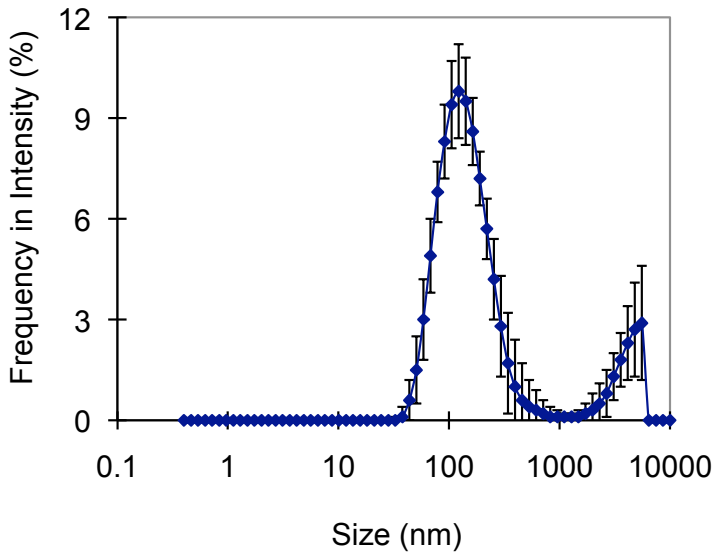

Figure A3.17: Average particle size distribution ($n = 10$), in intensity of scattered light of O_2 MNB water just after stopping the bubble generation ($DO = 44.5$ mg·L^{-1}), ($d_g = 125$ nm, $S_g = 69$ nm, $CV = 55.4\%$).

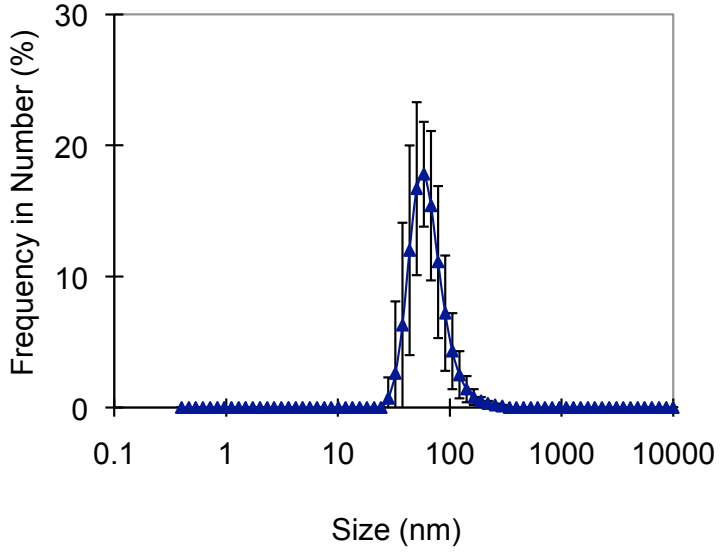

Figure A3.18: Average particle size distribution ($n = 10$), in number of particles of O_2 MNB water just after stopping the bubble generation ($DO = 44.5$ mg·L^{-1}), ($d_g = 58$ nm, $S_g = 22$ nm, $CV = 36.7\%$).

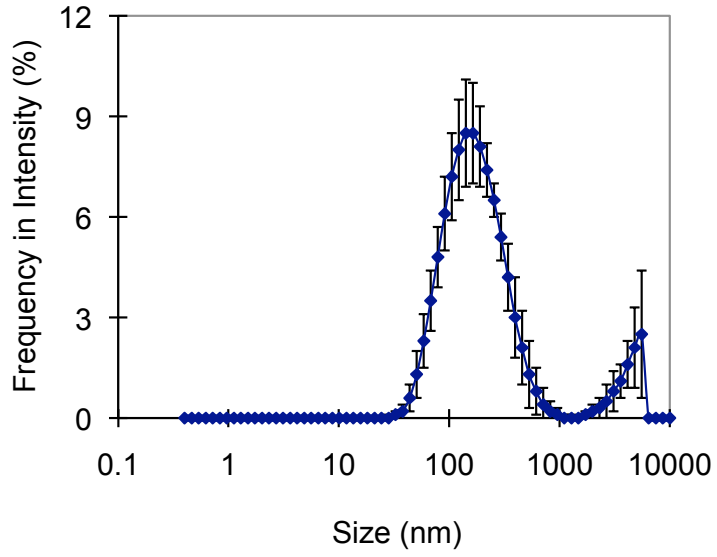

Figure A3.19: Average particle size distribution ($n = 10$), in intensity of scattered light of O_2 MNB water 1 d after stopping the bubble generation ($DO = 35.5$ mg·L^{-1}), ($d_g = 151$ nm, $S_g = 94$ nm, $CV = 62.1\%$).

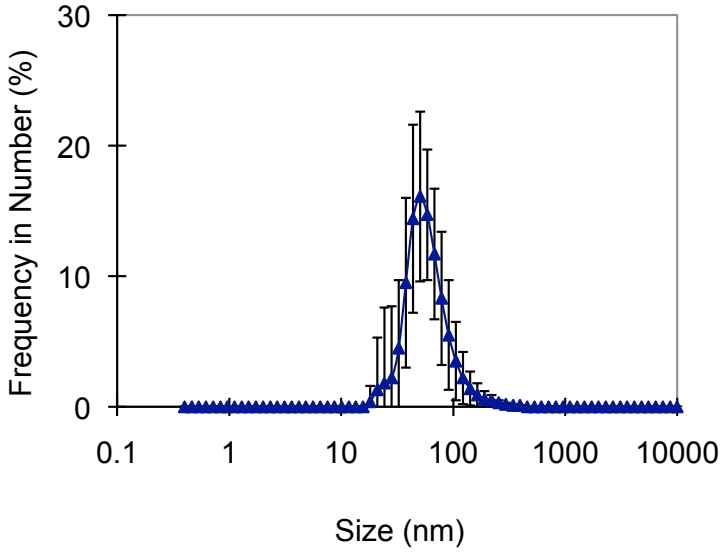

Figure A3.20: Average particle size distribution ($n = 10$), in number of particles of O_2 MNB water 1 d after stopping the bubble generation ($DO = 35.5$ mg·L^{-1}), ($d_g = 53$ nm, $S_g = 24$ nm, $CV = 45.4\%$).

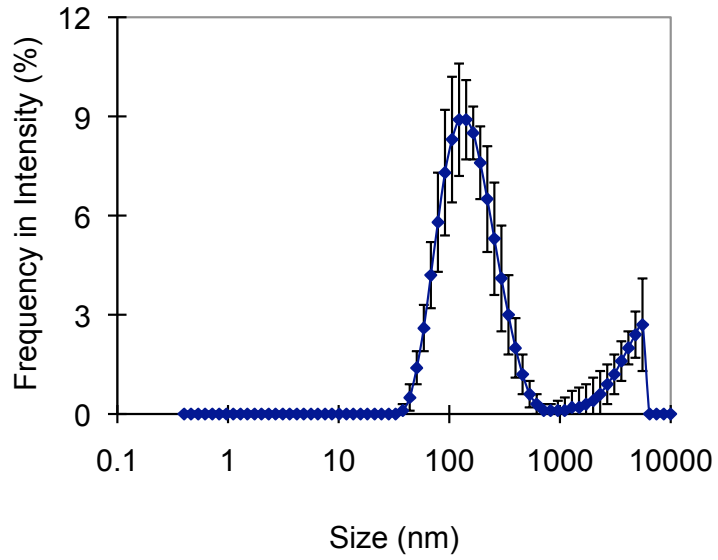

Figure A3.21: Average particle size distribution ($n = 10$), in intensity of scattered light of O_2 MNB water 2 d after stopping the bubble generation ($DO = 23.6$ mg·L^{-1}), ($d_g = 136$ nm, $S_g = 78$ nm, $CV = 57.4\%$).

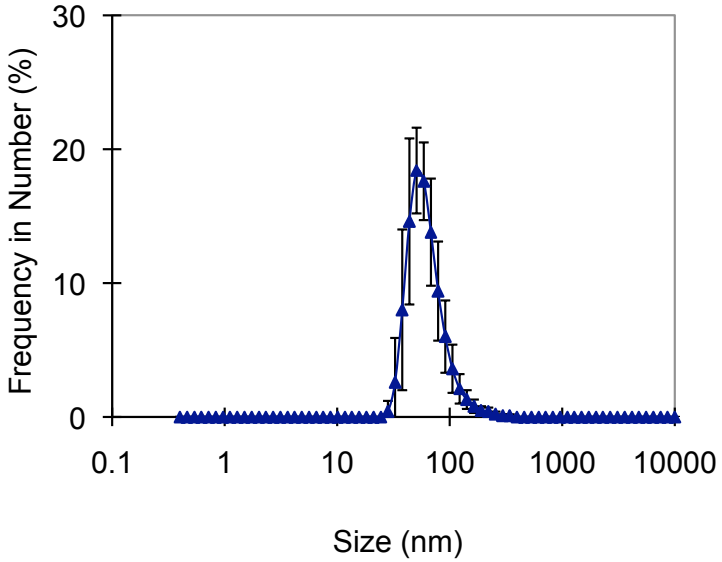

Figure A3.22: Average particle size distribution ($n = 10$), in number of particles of O_2 MNB water 2 d after stopping the bubble generation ($DO = 23.6$ mg·L^{-1}), ($d_g = 56$ nm, $S_g = 21$ nm, $CV = 37.1\%$).

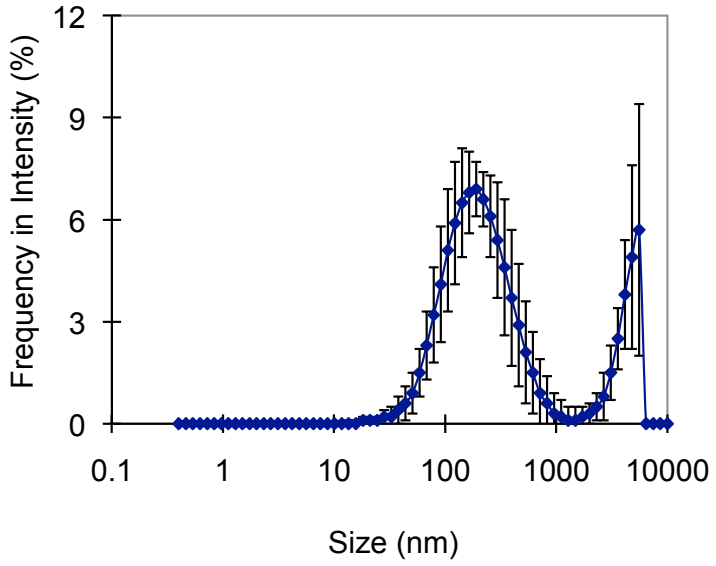

Figure A3.23: Average particle size distribution ($n = 10$), in intensity of scattered light of O_2 MNB water 5 d after stopping the bubble generation ($DO = 10.3$ mg·L^{-1}), ($d_g = 172$ nm, $S_g = 125$ nm, $CV = 72.6\%$). This sample was filtered with a 0.45 μm hydrophilic filter.

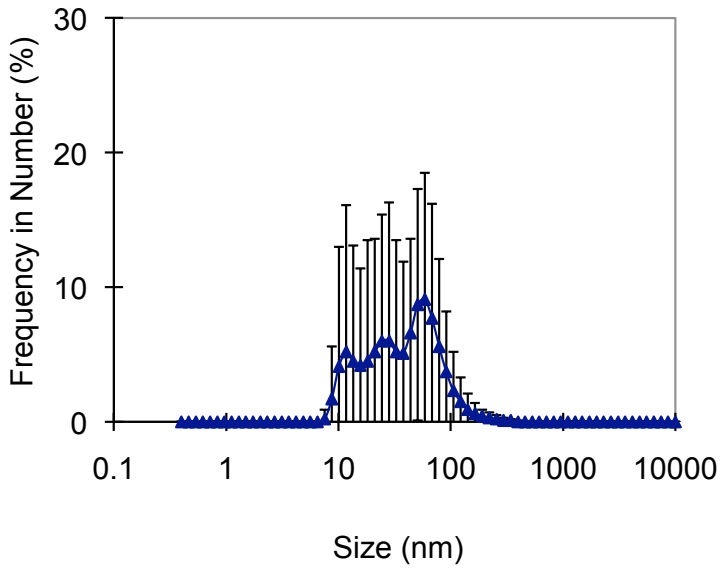

Figure A3.24: Average particle size distribution ($n = 10$), in number of particles of O_2 MNB water 5 d after stopping the bubble generation ($DO = 10.3$ mg·L^{-1}), ($d_g = 33$ nm, $S_g = 27$ nm, $CV = 80.6\%$). This sample was filtered with a 0.45 μm hydrophilic filter.

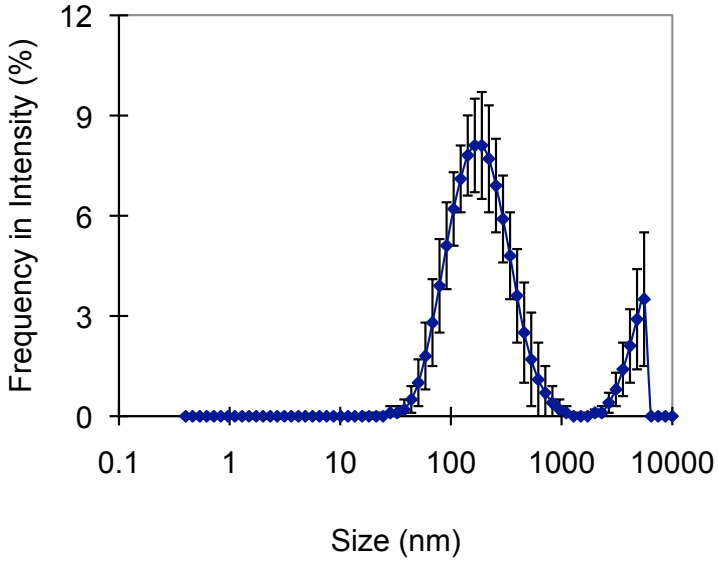

Figure A3.25: Average particle size distribution ($n = 10$), in intensity of scattered light of O_2 MNB water 12 d after stopping the bubble generation, ($d_g = 164$ nm, $S_g = 106$ nm, $CV = 64.7\%$).

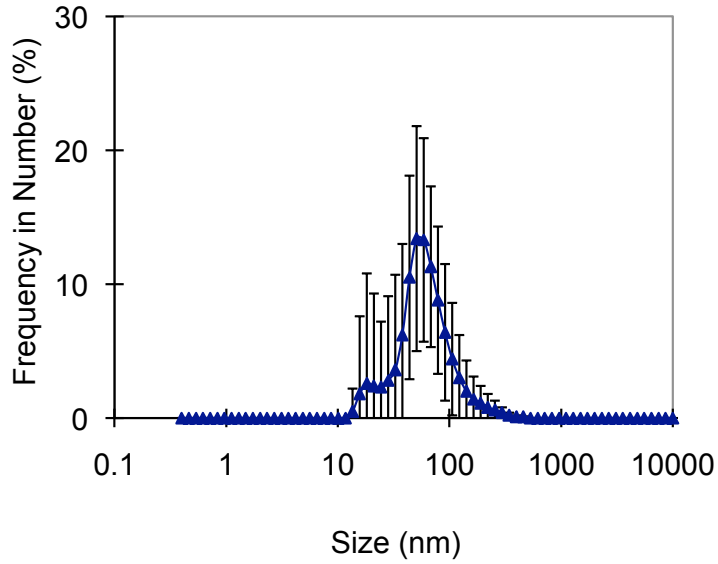

Figure A3.26: Average particle size distribution ($n = 10$), in number of particles of O_2 MNB water 12 d after stopping the bubble generation, ($d_g = 53$ nm, $S_g = 32$ nm, $CV = 59.9\%$).

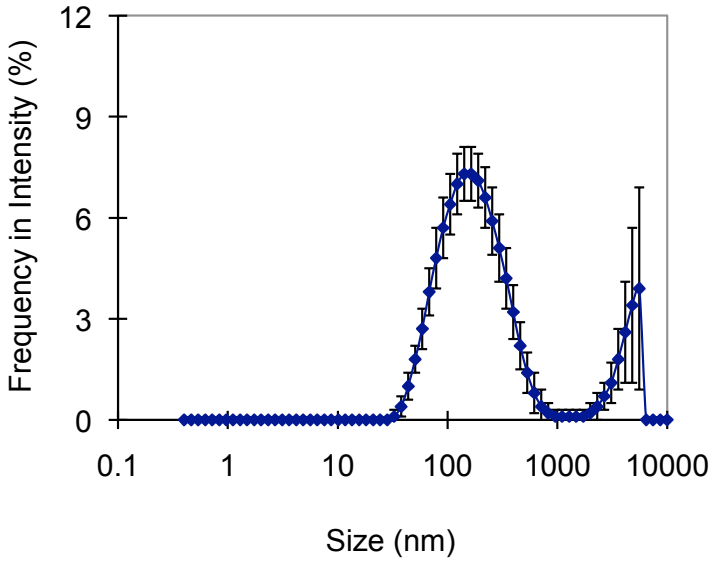

Figure A3.27: Average particle size distribution ($n = 5$), in intensity of scattered light of O_2 MNB water 15 d after stopping the bubble generation, ($d_g = 150$ nm, $S_g = 102$ nm, $CV = 68.5\%$).

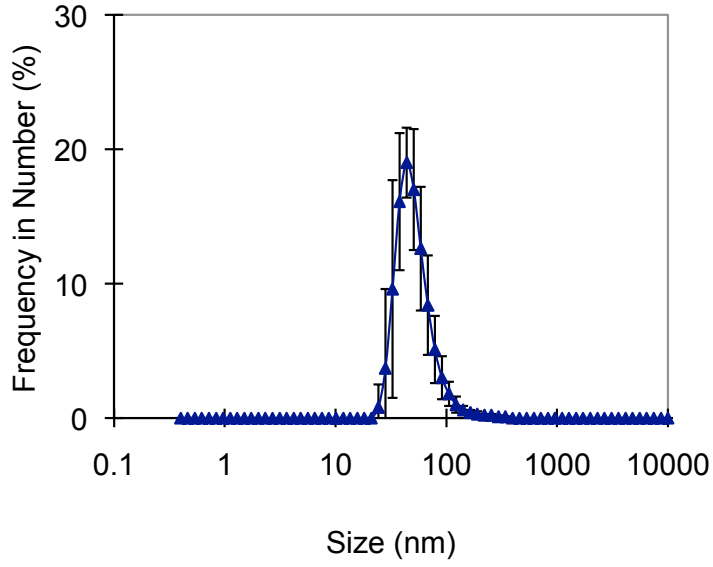

Figure A3.28: Average particle size distribution ($n = 5$), in number of particles of O_2 MNB water 15 d after stopping the bubble generation, ($d_g = 46$ nm, $S_g = 17$ nm, $CV = 37.5\%$).

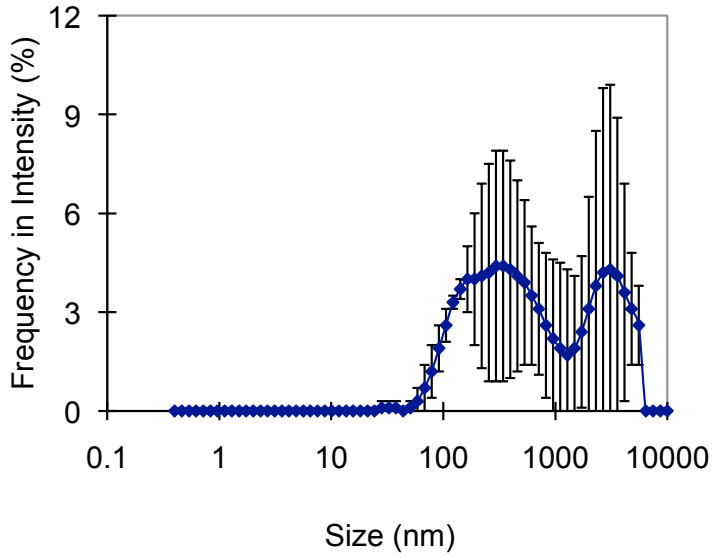

Figure A3.29: Average particle size distribution ($n = 5$), in intensity of scattered light of O_2 MNB water 18 d after stopping the bubble generation ($DO = 8.9$ mg·L^{-1}), ($d_g = 597$ nm, $S_g = 972$ nm, $CV = 162.7\%$).

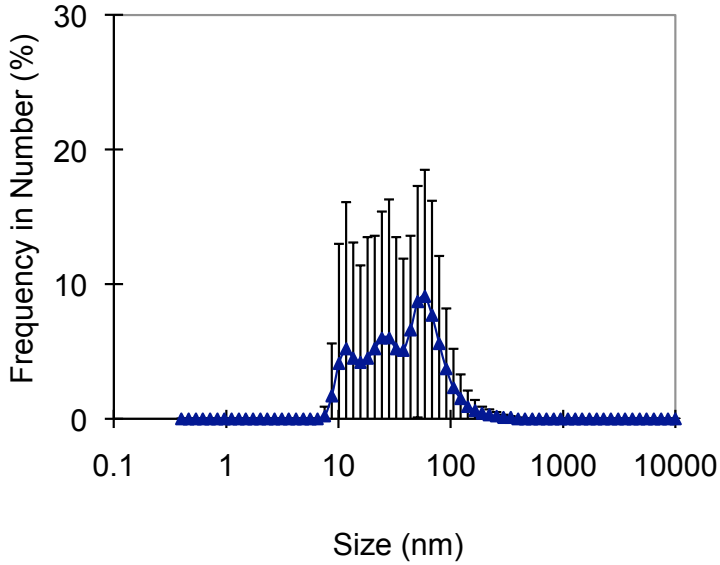

Figure A3.30: Average particle size distribution ($n = 5$), in number of particles of O_2 MNB water 18 d after stopping the bubble generation ($DO = 8.9$ mg·L^{-1}), ($d_g = 65$ nm, $S_g = 45$ nm, $CV = 70.1\%$).

Air MNB Water

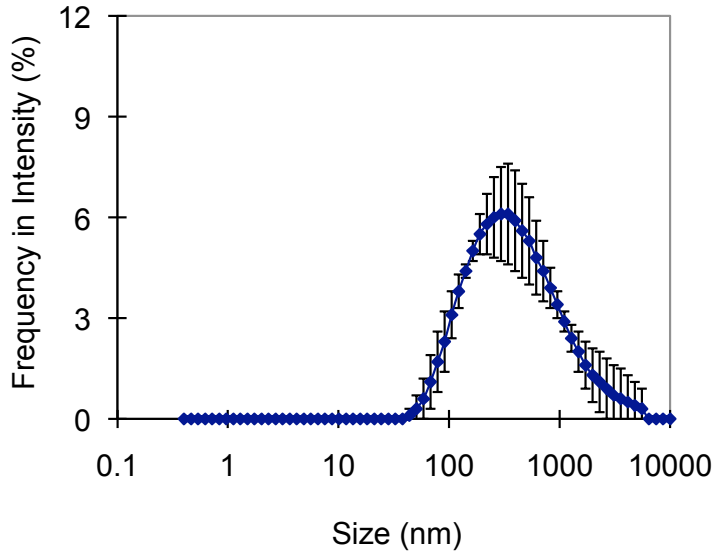

Figure A3.31: Average particle size distribution ($n = 5$), in intensity of scattered light of air MNB water 5 min after stopping the bubble generation ($DO = 11.7$ mg·L^{-1}), ($d_g = 350$ nm, $S_g = 375$ nm, $CV = 107.3\%$).

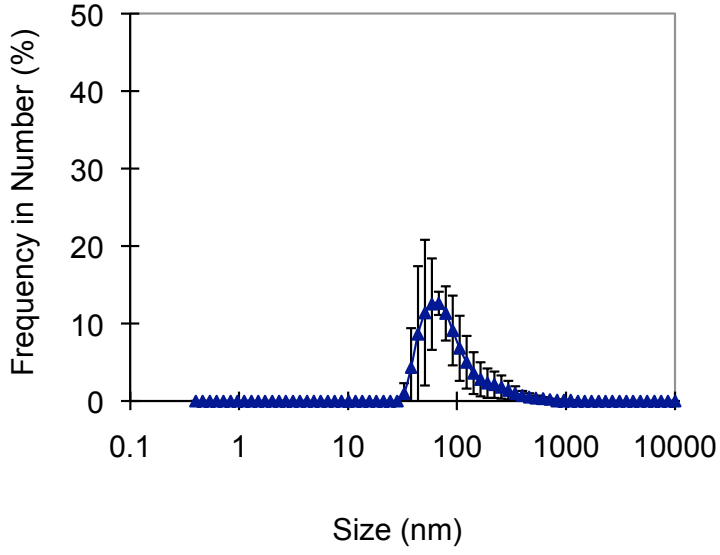

Figure A3.32: Average particle size distribution ($n = 5$), in number of particles of air MNB water 5 min after stopping the bubble generation ($DO = 11.7$ mg·L^{-1}), ($d_g = 76$ nm, $S_g = 47$ nm, $CV = 61.6\%$).

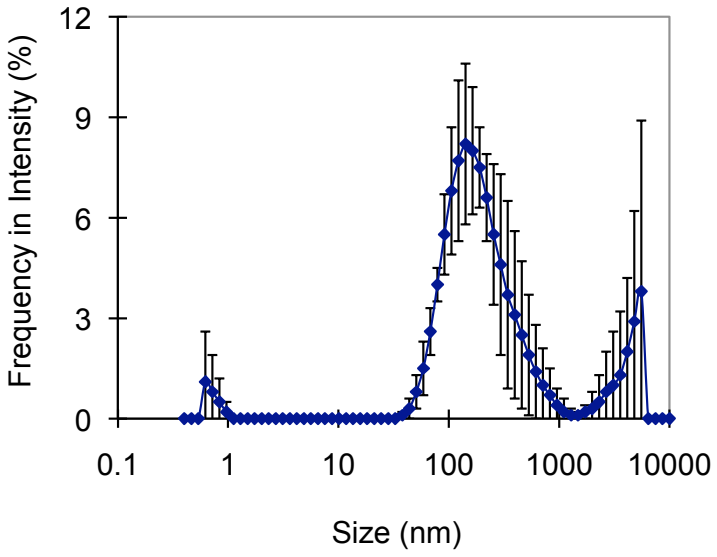

Figure A3.33: Average particle size distribution ($n = 5$), in intensity of scattered light of air MNB water 25 min after stopping the bubble generation, ($d_g = 140$ nm, $S_g = 192$ nm, $CV = 137.5\%$).

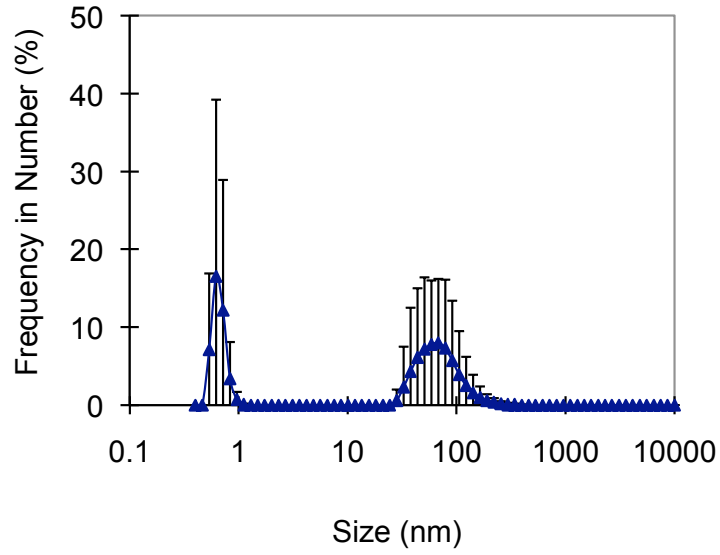

Figure A3.34: Average particle size distribution ($n = 5$), in number of particles of air MNB water 25 min after stopping the bubble generation, ($d_g = 10$ nm, $S_g = 48$ nm, $CV = 490.4\%$).

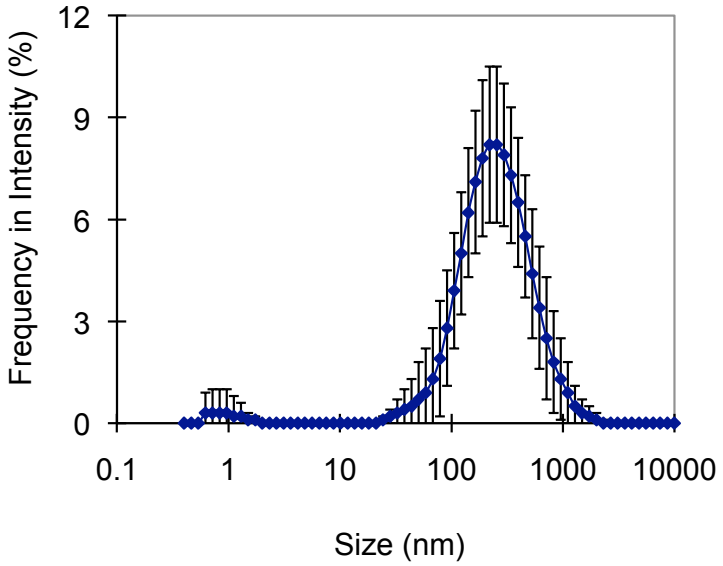

Figure A3.35: Average particle size distribution ($n = 5$), in intensity of scattered light of air MNB water 45 min after stopping the bubble generation ($DO = 11.5$ mg·L^{-1}), ($d_g = 205$ nm, $S_g = 248$ nm, $CV = 120.7\%$).

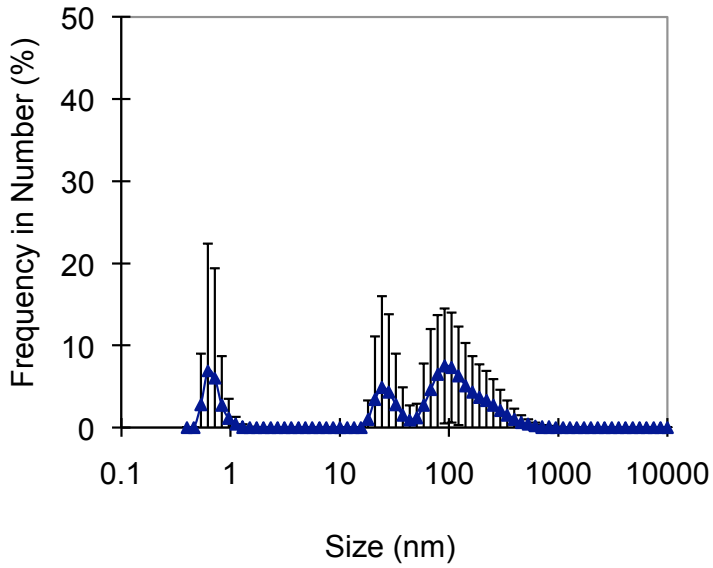

Figure A3.36: Average particle size distribution ($n = 5$), in number of particles of air MNB water 45 min after stopping the bubble generation ($DO = 11.5$ mg·L^{-1}), ($d_g = 31$ nm, $S_g = 122$ nm, $CV = 392.0\%$).

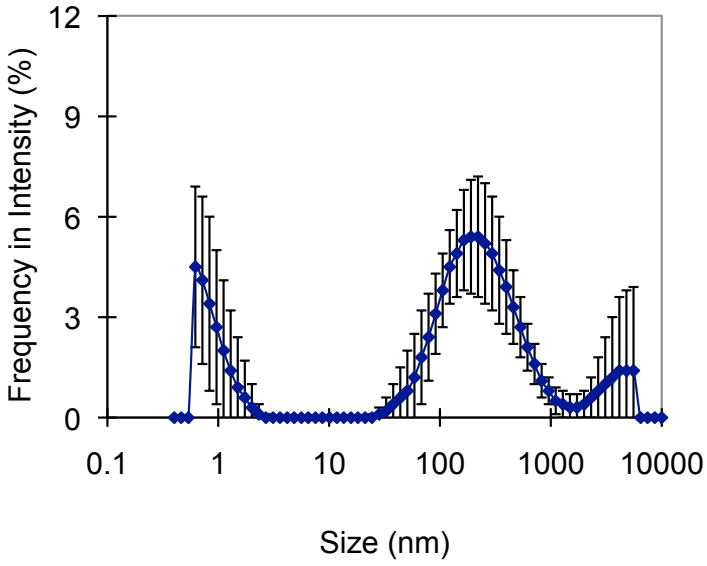

Figure A3.37: Average particle size distribution ($n = 5$), in intensity of scattered light of air MNB water 70 min after stopping the bubble generation, ($d_g = 84$ nm, $S_g = 524$ nm, $CV = 626.3\%$).

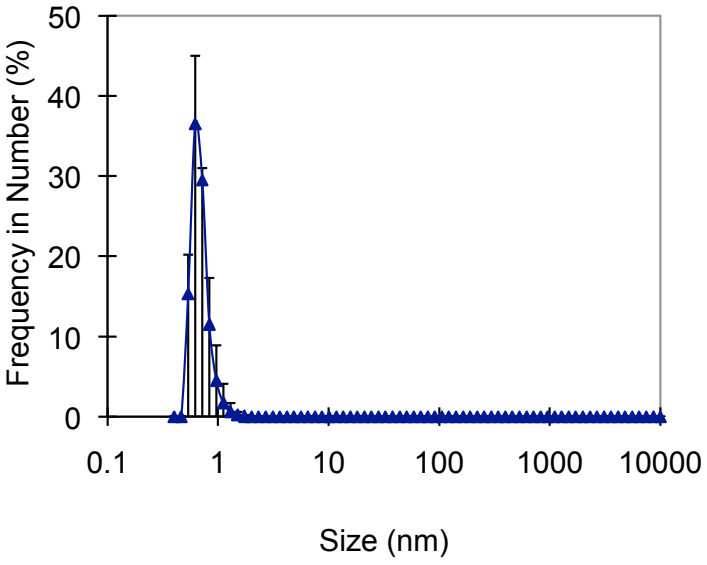

Figure A3.38: Average particle size distribution ($n = 5$), in number of particles of air MNB water 70 min after stopping the bubble generation, ($d_g = 0.6$ nm, $S_g = 0.1$ nm, $CV = 17.9\%$).